Tensor network methods for non-equilibrium dynamics of quantum spin liquids

Ravi Teja Ponnaganti

Université Fédérale
Toulouse Midi-Pyrénées

THÈSE

En vue de l'obtention du
DOCTORAT DE L'UNIVERSITÉ DE TOULOUSE

Délivré par l'Université Toulouse 3 - Paul Sabatier

Présentée et soutenue par

Ravi Teja PONNAGANTI

Le 28 mars 2023

Méthodes de réseaux tensoriels pour la dynamique hors équilibre des liquides de spin quantique

---

Ecole doctorale : **SDM - SCIENCES DE LA MATIERE - Toulouse**

Spécialité : **Physique**

Unité de recherche :
LPT - Laboratoire de Physique Théorique

Thèse dirigée par
Didier POILBLANC et Matthieu MAMBRINI

Jury

M. Roman ORUS, Rapporteur
M. Andreas Martin LäUCHLI, Rapporteur
Mme Mari Carmen BAñULS, Examinatrice
M. Norbert SCHUCH, Examinateur
Mme Nathalie GUIHéRY, Examinatrice
M. Luca TAGLIACOZZO, Examinateur
M. Didier POILBLANC, Directeur de thèse
M. Matthieu MAMBRINI, Co-directeur de thèse

Contents

Introduction

One of the most interesting aspects of modern condensed matter physics, which is the study of interacting electrons from a microscopic and macroscopic level, can be summarized in one phrase – "More is different" [1]. The presence of strong interactions and entanglement in a system governed by quantum mechanics can lead to several exotic states of matter if the system has a large number of particles. Quantum spin liquids are one such set of exotic states that have attracted significant interest, not only due to their interesting properties but also because of the possible technological applications. The rapid progress in cold atom experiment setups, particularly the Rydberg atom simulators, has opened up new avenues to study these spin liquids in one and two dimensions [2]. This calls for advanced theoretical techniques to investigate the non-equilibrium properties of isolated pure quantum states. Exact diagonalization methods are severely restricted by the system sizes. Time-dependent Density Matrix Renormalization Group (tDMRG) and Matrix Product States (MPS) are currently being explored to study the quench dynamics of one-dimensional systems [3–6] though their applicability to systems with critical correlations is questionable [7]. However, no such techniques currently exist for two-dimensional systems. The aim of this thesis is to develop numerical algorithms to study the non-equilibrium properties of spin liquids on a square lattice following a quantum quench using the framework of tensor networks. A variational form of Projected Entangled Pair State (PEPS) ansatz is used to describe the spin liquids. A new symmetric form of the Corner Transfer Matrix Renormalization group (CTMRG), the algorithm necessary to construct the reduced density matrix of the wavefunction in the thermodynamic limit, is described. To study the quench dynamics, two algorithms called the simple update and the variational optimization, along with the necessary modifications to adapt them to study spin liquid wavefunctions, are explained. The tools are then used to study the non-equilibrium dynamics of the resonating valence bond (RVB) state with only nearest-neighbor (NN) valence bond configurations which is a spin-liquid state that is known to exhibit critical dimer-dimer correlations.

This thesis is organized as follows: In Chapter 1, we provide a brief introduction to some basic physics and the motivation related to the work, from the basics of quantum spin systems to the basics of quantum spin liquids and the recent developments in ultracold atomic simulators that demand the need for new numerical and theoretical techniques. Chapter 2 is dedicated to explaining the basics of tensor networks. We start with the diagrammatic notation and follow it with the basics of matrix product states. After explaining the basics of PEPS, we provide a numerical scheme to construct the basis of SU(2) symmetric PEPS with relevant spatial symmetries.

Chapter 3 is dedicated to explaining the tensor network algorithms for time evolution, such as the symmetric simple update and complex-symmetric CTMRG, along with the matrix factorizations that are used in those schemes. Chapter 4 contains the results obtained using the algorithms in chapter 3. An appendix includes some of the ideas that are currently being developed to improve the results.

Acknowledgements

I am honored to express my deepest gratitude to the individuals and groups who have played a pivotal role in the completion of my thesis. First and foremost, I extend my heartfelt thanks to my supervisors, Didier Poilblanc and Matthieu Mambrini, for their invaluable guidance, support, and encouragement throughout my research journey. Their expertise, insight, and unwavering commitment have been instrumental in shaping my intellectual development and enhancing the quality of my work. Without their constant support and supportive leeway, I would not have successfully finished my thesis.

I extend my sincere appreciation to all the members of Laboratoire de Physique Théorique, including Sylvan Capponi, Fabien Alet, Nicolas Laflorencie, Nicolas Destainville, Bertrand Georgeot, Faedi Loulidi, Naïmo Davier, Jeanne Colbois, Bhupen Dhabolkar, Sasank Budaraju, and Sen Niu for their willingness to share their expertise, provide constructive feedback and making these three years memorable. I thank former members of the lab Juraj Hasik, Olivier Gauthé and Pranay Patil for their engaging discussions. I am humbled to have had the opportunity to work with such exceptional scholars.

My heartfelt thanks go to Malika Bentour and Mathilde Rasolomalala, our secretaries, for helping me navigate the challenging paperwork that comes with living in France, and to Sandarine, our computing officer, for her unwavering support in everything related to local computation resources. I would like to thank the CALMIP team for their High-Performance Computing services, which were instrumental in producing the bulk of the results. I thank Jerome Cuny for his help in administrative processes.

I am grateful to Roman Orus and Andreas Läuchli for accepting to be the rapporteurs of this manuscript and to Mari Carmen Bañuls, Norbert Schuch, Nathalie Guihéry, and Luca Tagliacozzo for participating in my jury. A special thanks to all the coordinators and organizers of the 'Entanglement in SCS' conference in Benasque for hosting me every year.

On a personal note, I would like to thank my parents and my sister for their constant love and support. My friends, Rohit Dokara, Swetha Kalla, and Anagha Sasikumar deserve special thanks for their unwavering support throughout.

Finally, I am grateful to my masters' supervisors, Prof. Rajesh Narayanan and Prof. Yasir Iqbal, for introducing me to the fun world of condensed matter theory research. I would not have had the opportunity to pursue my Ph.D. in LPT if not for them.

To Rajesh and Yasir. . .

Chapter 1

Preliminaries

In this chapter, we give a brief introduction to the physics of quantum magnetism and spin liquids. We also discuss the recent developments in cold atom simulators that have motivated the rest of the work.

1.1 Quantum spin systems

1.1.1 Mott insulators and Hubbard model

In order to truly understand the basics of quantum spin systems, one has to start with the fundamental properties of electrons. We shall now start with the model of a collection of electrons moving through a solid-state material. The general Hamiltonian of this model contains a kinetic energy term that takes care of the motion of electrons and a potential energy term that includes the interaction of the electrons with the solid lattice and the interaction of electrons among themselves [8].

$$\mathcal{H} = \frac{-\hbar^2}{2m_e}\nabla^2 + U_{\text{ion}}(\mathbf{r}) + \sum_{i\neq j}\frac{e^2}{|\mathbf{r}_i - \mathbf{r}_j|}. \tag{1.1}$$

To make things simple, the nature of the solid-state material is not considered. The material is assumed to be a perfect crystal with no lattice imperfections. Similarly, the electron-phonon interactions are ignored to make the Hamiltonian much simpler to solve. Once the dynamical effects of the lattice are ignored, the interaction of the electrons with ions (the U_{ion} term) is reduced to a Coulomb interaction term in which the charge of the nucleus is slightly screened by the effect of the electron cloud in the inner shells. In such a lattice, one can use the periodicity of the lattice to apply Bloch's theorem [9] and reduce the wavefunction to,

$$\phi(\mathbf{r}) = e^{i\mathbf{k}\cdot\mathbf{r}}u_{\mathbf{k}}(\mathbf{r}),$$

where the function $u_{\mathbf{k}}(\mathbf{r})$ is a periodic function whose periodicity matches that of the lattice. Notice that $\phi(r)$ only represents the radial part of the wavefunction. The complete wavefunction, including the spin-component, is given by $\psi_\sigma(r) = \chi(\sigma)\phi(r)$. However, these functions are delocalized and if we want to use localized states, we have to take the inverse Fourier transform of these wavefunctions. This results in the Wannier functions [10],

$$w_i(\mathbf{r}) = w(\mathbf{r} - \mathbf{R_i}) = \frac{1}{\sqrt{N}}\sum_k\sum e^{-\mathbf{k}\cdot\mathbf{R_i}}u_{\mathbf{k}}(\mathbf{r}), \tag{1.2}$$

where $\mathbf{R_i}$ is the lattice vector. The creation operator of an electron with spin σ in the Wannier basis is then given by,

$$c^\dagger_{i\sigma} = \int d^3\mathbf{r}\, w_i(\mathbf{r})\psi^\dagger_\sigma(\mathbf{r}). \tag{1.3}$$

Notice that, these are just unitary transformations of the Bloch states and do not involve any approximations. Nonetheless, they are quite helpful in reducing the Hamiltonian equation (1.1) to,

$$\mathcal{H} = \sum_{ij\sigma} t_{ij}c^\dagger_{i\sigma}c_{j\sigma} + U\sum_{\sigma\sigma'}c^\dagger_{i\sigma}c^\dagger_{i\sigma'}c_{i\sigma'}c_{i\sigma}, \tag{1.4}$$

where the kinetic term,

$$t_{ij} = \langle i| \left[-\frac{\hbar^2}{2m_e}\nabla^2 + U_{\text{ion}}\right] |j\rangle$$

is called the "hopping" term, the action of which results in the electron hopping from site i to site j. Using the Pauli exclusion principle and the particle number operator, we can rewrite this as the well-known Hubbard Hamiltonian [11],

$$\mathcal{H} = \sum_{i,j,\sigma} t_{ij} c^\dagger_{i\sigma} c_{j\sigma} + U \sum_i n_{i\uparrow} n_{i\downarrow}, \tag{1.5}$$

where $n_{i\sigma} = c^\dagger_{i\sigma} c_{i\sigma}$. This equation clearly has two limits. When the electronic repulsions are weak and the electrons are largely uncorrelated, we get the metallic phase at $|t_{ij}| \gg U$ where the electrons move freely [12]. In the other limit, $|t_{ij}| \ll U$, the electrons are strongly correlated, and any form of hopping results in a large energy cost thus, the system acts like an insulator, called the Mott insulator. The transition from the metallic phase to the insulator phase under the effect of the interactions is called the Mott transition. However, in this insulator limit, we can treat the hopping term as a perturbation [13].

$$H = H_U + H_t$$

Since the eigenvalues and the eigenstates of H_u merely count the number of states of sites with a pair of electrons n, the eigenvalues of H_u only depend on n. We may write the eigenstates as $|nk\rangle$ with eigenvalues nU. We shall restrict ourselves to a state with only one electron per site. This implies that $n = 1$ is the ground state of H_u. Additionally, since the hopping term moves an electron from one site to another, the action of the term on two neighboring sites will result in a site with two electrons and the other having zero electrons. This makes the first order perturbation term $\langle nl| H_t |nk\rangle$ zero for $n = 1$. In the second-order term, the action hops the spins twice. While this shifts the spins around, the eigenvalue of the resultant state remains unchanged. Hence, the effective second-order perturbation Hamiltonian can be written as,

$$H^{(2)}_{\text{eff}} = P_1 (H_t^2/U) P_1, \tag{1.6}$$

where $P_1 = \prod_i (1 - n_{i\uparrow} n_{i\downarrow})$ is the Gutzwiller projection operator that restricts the Hilbert space of H_{eff} to the subspace of state with one particle per site.

$$\begin{aligned} H^{(2)}_{\text{eff}} &= \Big(\sum_{lk} \sum_{\sigma\nu} t_{lk} t^*_{kl} c^\dagger_{l\sigma} c_{k\sigma} c^\dagger_{k\nu} c_{l\nu}\Big)/U \\ &= \sum_{lk} \sum_{\sigma\nu} \frac{|t_{kl}|^2}{U} c^\dagger_{l\sigma} c_{l\nu} (\delta_{\sigma\nu} - c^\dagger_{k\nu} c_{k\sigma}) \\ &= \sum_{kl} \frac{|t_{kl}|^2}{U} \times \sum_{kl\sigma} (n_{l\sigma} n_{k\sigma} + c^\dagger_{l\sigma} c_{l-\sigma} c^\dagger_{k\sigma} c_{k-\sigma}) \end{aligned} \tag{1.7}$$

The spin operators in terms of fermionic operators can be defined as,

$$S_i^z = \frac{1}{2}\sum_\sigma n_{i\sigma} \tag{1.8}$$

$$S_{i\sigma} = c_{i\sigma}^\dagger c_{i-\sigma} \tag{1.9}$$

$$\mathbf{S}_i = c_i^\dagger \hat{\sigma} c_i \tag{1.10}$$

$$\implies \mathbf{S}_i \cdot \mathbf{S}_j = \frac{1}{2}\sum_\sigma S_{i\sigma}S_{j\sigma} + S_i^z S_j^z, \tag{1.11}$$

where $\hat{\sigma}$ are the Pauli matrices. This reduces the equation (1.7) to,

$$\begin{aligned} H_{\text{eff}}^{(2)} &= \sum_{kl}\left(\frac{|t_{kl}|^2}{U}\right)\left(\sum_\sigma S_{l\sigma}S_{k-\sigma} + 2S_l^z S_k^z - \frac{1}{2}\right) \\ &= \sum_{kl}\frac{|t_{kl}|^2}{U}(\mathbf{S_k}\cdot\mathbf{S_l} - \frac{1}{4}) \end{aligned} \tag{1.12}$$

Hence, for the case where the system has exactly one electron per site (half-filling), the effective spin Hamiltonian that governs the physics of the system is given by,

$$\mathcal{H} = \sum_{\langle i,j\rangle} J_{ij}\mathbf{S_i}\cdot\mathbf{S_j}, \tag{1.13}$$

where, $J_{ij} = \frac{4|t_{ij}|^2}{U} > 0$ is the interaction term. For a spin-$\frac{1}{2}$ system, this Hamiltonian is exactly solvable in one dimension using the Bethe ansatz [14]. No closed-form solution is currently available for larger spins and higher dimensions, and one has to rely on approximation schemes and numerical results to understand the system better. An interesting thing to note is that the main source of the Heisenberg interaction is the electron-electron repulsion arising from Coulomb interactions and Pauli's exclusion principle and not the magnetic moments of the electrons.

1.1.2 SU(2) physics

In this section, we shall discuss the basics of SU(2) group theory and its connection to spin models. In doing so, along with shedding light on the underlying physics, we also introduce some key vocabulary of group theory that shall be used later in the thesis. For details on the notation and further reading, we refer to Ref. [15].

Group representation

A group G is a set of elements $(a, b, c, ...)$ defined along with a multiplicative operation between two group elements, that has the following properties,

- Closure. $\forall a, b \in G$, $c = a \cdot b$, then $c \in G$
- Identity. There should exist an identity element e such that $x \cdot e = x\ \forall x \in G$.
- Associativity. $(x \cdot y) \cdot z = x \cdot (y \cdot z)\ \forall x, y, z \in G$.

- Inverse. Every element x in the group should have a inverse x^{-1} such that the result of the multiplicative operation with that of the inverse is the identity e, i.e., $x \cdot x^{-1} = x^{-1} \cdot x = e,\ \forall x, x^{-1} \in G$.

If the group operation is commutative for all the elements in the group, i.e., $a \cdot b = b \cdot a$, the group is called an abelian group. An example of an abelian group is $\mathbb{Z}_n$, the cyclic group of order n. It consists of elements $a, a^2, a^3, ..., a^n = e$, which consists of a binary operation (a) and its repeated application (a^i), that when performed n-times repeatedly, returns the initial state $(a^n = e)$. An example of a non-abelian group is the permutation group S_n, which consists of operations to permute n objects.

A representation of a group G is a homomorphism of G onto a group $D(G)$, the elements of which are operators in a space L. If a basis is chosen for L, the elements of $D(G)$ can be represented by matrices [16]. Thus, it maps every element of the group to a matrix such that the group operation of two elements is the matrix multiplication, i.e., $a \rightarrow \rho(a)$ such that if $a \cdot b = c$ then $\rho(a)\rho(b) = \rho(c)$. The dimension of a representation is the dimension of the corresponding matrix.

If a representation ρ of a group can be written in the block-diagonal form, then the representation is called a reducible representation, else it is called an irreducible representation or irreps. For a reducible representation, there exists an invertible matrix M such that,

$$M\rho(a)M^{-1} = \begin{pmatrix} \rho_1(a) & & & \\ & \rho_2(a) & & \\ & & \ddots & \\ & & & \rho_P(a) \end{pmatrix}. \tag{1.14}$$

The reducible representation ρ is then said to be written as a *direct sum* $\rho(a) = \rho_1(a) \oplus \rho_2(a) \oplus \cdots \oplus \rho_P(a)$. This implies that there is a subset of states that are never connected. The dimension of a reducible representation is the sum of the dimensions of the corresponding irreducible representations. Note that a group with infinite elements can have a finite-dimensional representation. A *Lie group* is a group with real continuous parameters that make up a smooth manifold. Every Lie group can be labeled by a set of continuous parameters. Let $a(\boldsymbol{\theta}) = a(\theta_1, \theta_2, ..., \theta_n)$. Every Lie group that can be represented by a set of unitary representations consists of a set of matrices X_i called *generators*.

$$a(\boldsymbol{\theta}) = e^{i\boldsymbol{\theta}\cdot\mathbf{X}} = e^{i\sum_k \theta_k X_k}. \tag{1.15}$$

The generators of a Lie group obey the Lie algebra,

$$[X_i, X_j] = iC_{ijk}X_k, \tag{1.16}$$

where C_{ijk} are called the structure constants of the group and satisfy the condition, $C_{ijk} = -C_{ikj}$.

We now look at some useful special groups.

- Unitary group $U(N)$: The set of $N \times N$ unitary matrices, i.e, $U^\dagger U = UU^\dagger = I$.
- Special unitary group $SU(N)$: The set of $N \times N$ unitary matrices whose determinant $\det(U) = 1$.
- Special orthogonal group $SO(N)$: The set of $N \times N$ orthogonal matrices $OO^T = O^T O = I$ whose determinant $\det(O) = 1$.

The special unitary group SU(2) is hence defined as a set of 2×2 unitary matrices with determinants equal to one. The generators of the SU(2) group are given by the Pauli matrices σ_i.

$$\sigma_x = \begin{pmatrix} 0 & 1 \\ 1 & 0 \end{pmatrix}, \ \sigma_y = \begin{pmatrix} 0 & -i \\ i & 0 \end{pmatrix}, \ \sigma_z = \begin{pmatrix} 1 & 0 \\ 0 & -1 \end{pmatrix}. \tag{1.17}$$

The generators of the group are then given by $J_i = \sigma_i/2$, and the commutation relation of the generators is,

$$[J^\alpha, J^\beta] = i\epsilon_{\alpha\beta\gamma} J^\gamma, \tag{1.18}$$

where $(\alpha, \beta, \gamma = x, y, z)$. Using this, one can construct the angular momentum eigenstates by writing the representation group of the angular momentum operator as a direct sum of irreducible representations of SU(2). In order to obtain the representation group of the angular momentum states, we first define a *Casimir operator* which commutes with all the generators of the group

$$\mathbf{J}^2 = J_1^2 + J_2^2 + J_3^2. \tag{1.19}$$

We choose J_3 to be the operator that acts on the natural basis and then define the raising and the lowering operators as,

$$J_\pm = (J_1 \pm J_2). \tag{1.20}$$

then

$$\mathbf{J}^2 = \frac{1}{2}(J_+ J_- + J_- J_+) + J_3^2. \tag{1.21}$$

Since $\mathbf{J}$ and J_3 commute, they should have a common eigenbasis. Let j and m be the corresponding eigenvalues.

$$\begin{aligned} \mathbf{J}^2 |j;m\rangle &= j\,|j;m\rangle \\ J_3 |j;m\rangle &= m\,|j;m\rangle \\ J_\pm |j;m\rangle &= \sqrt{(j \mp m)(j \pm m + 1)}\,|j;m+1\rangle \end{aligned} \tag{1.22}$$

The value of m has an upper bound of j and a lower bound of $-j$. Thus the basis of the SU(2) irreducible representation are, $|j;m\rangle$ where $m = -j, -j+1, ..., j-1, j$, which has a dimension of $(2j+1)$.

Now one might ask why the electron spin operators should obey the SU(2) group rules. The fundamental idea of using SU(2) group to study the spin of a system has a historical precedent. During the early days of the development of quantum mechanics, the concept of electronic spin was introduced to better understand the

magnetic moment of an atom [17]. While it is known that the angular momentum from the orbital contributes to a part of the magnetic moment, the remaining missing part was assumed to be from the physical rotation of an electron about its own axis. Using the angular momentum argument, we begin by defining the angular momentum operator as,

$$\mathbf{S} = \mathbf{x} \times \mathbf{p}. \tag{1.23}$$

The position operator $\mathbf{x}$ and the momentum operator $\mathbf{p}$ obey the commutation relation $[x, p] = i\hbar$. In natural units, we shall take $\hbar = 1$ from now on. The commutation relationship implies that the angular momentum operator of two particles (labelled j and k) obeys the SU(2) commutation relationship.

$$[S_j^\alpha, S_k^\beta] = i\epsilon_{\alpha\beta\gamma} S_k^\gamma \delta_{kj}. \tag{1.24}$$

The "spin" of an electron was later identified to be an intrinsic property of the electron but not a physical rotation (the concept of a point-like electron spinning would result in a faster-than-light rotation speed). However, its relationship with angular momentum holds true regardless of the nature of the origin. As the spin operators obey the SU(2) commutation relations, the Lie algebra of SU(2) can then be used to provide a mathematical description of a spin system.

Addition of angular momentum

The above description works well for an arbitrary spin system. For a system of multiple particles, the wavefunction has to be described on a global level. Consider a system of two spin particles with spins s_1 and s_2. The resultant Hilbert space is given by the tensor product of the individual Hilbert spaces.

$$H = H_1 \otimes H_2. \tag{1.25}$$

The corresponding representations have the dimensions $(2s_1 + 1)$ and $(2s_2 + 1)$. Let $I_{(1)}$ and $I_{(2)}$ be two identity matrices with dimensions $(2s_1 + 1)$ and $(2s_2 + 1)$. The total angular momentum operator is given by,

$$\mathbf{S} = \mathbf{S_1} \otimes I_{(2)} + I_{(1)} \otimes \mathbf{S_2}. \tag{1.26}$$

In order to break the total spin as a direct sum of irreducible representations, one has to diagonalize the total angular momentum operators.

$$\mathbf{S}^2 = \mathbf{S_1}^2 \otimes I_{(2)} + I_{(1)} \otimes \mathbf{S_2}^2 + 2[\frac{1}{2}(S_1^+ \otimes S_2^- + S_1^- \otimes S_2^+) + S_1^z \otimes S_2^z]. \tag{1.27}$$

The diagonalization of this operator has the eigenvalues $|s_1 - s_2|, |s_1 - s_2| + 1, ..., s_1 + s_2$. The relation between the basis of the representation group of the individual spins and the collective spins is given by,

$$|J; M\rangle = \sum_{m_1, m_2} \langle j_1, j_2; m_1, m_2 | J; M\rangle \, |j_1; m_1\rangle \, |j_2; m_2\rangle \, . \tag{1.28}$$

The inner products $\langle j_1, j_2; m_1, m_2 | J; M\rangle$ have been defined to be in such a way that the resultant total spin $|J; M\rangle$ satisfies the SU(2) commutation relationships. These

inner products are called the Clebsch-Gordan coefficients. And the rules governing the resultant breakdown of the total spin operator into a direct sum of irreps are called SU(2) *fusion rules*. In general, the fusion rules of two spins s_1 and s_2 result in a direct sum of $(2s_{\text{min}}+1)$ spins that differ by one unit and s_{min} is the smaller of the two spins.

$$s_1 \otimes s_2 = |s_1 - s_2| \oplus |s_1 - s_2| + 1 \oplus \ldots \oplus (s_1 + s_2). \tag{1.29}$$

Heisenberg ground state

We apply the knowledge of SU(2) physics to study the Heisenberg interactions between two spin-$\frac{1}{2}$ particles. Using the definitions of the raising and the lowering operators $S_i^+ = S_i^x + iS_i^y$ and $S_i^- = S_i^x - iS_i^y$ and their relation with the spin states in S_z basis, we write the Heisenberg Hamiltonian as,

$$S^+ |\downarrow\rangle = |\uparrow\rangle\,,\ S^- |\uparrow\rangle = |\downarrow\rangle\,,\ S^+ |\uparrow\rangle = 0,\ S^- |\downarrow\rangle = 0$$

Using these, we can rewrite the Heisenberg Hamiltonian of equation (1.13) as,

$$\mathcal{H} = \sum_{ij} J_{ij} \left(\frac{1}{2}(S_i^+ S_j^- + S_i^- S_j^+) + S_i^z S_j^z \right). \tag{1.30}$$

For a simple system of two spin-$\frac{1}{2}$ particles, this Hamiltonian has four eigenstates with two distinct eigenvalues. The eigenstates corresponding to the higher energy value of $+0.5J$ have a three-fold degeneracy and form the spin triplet. The eigenstate corresponding to the lower energy value of $-0.5J$ is called a singlet. The orthogonal eigenstates corresponding to these eigenvalues in the S_z basis are:

$$|S_{\text{triplet}}\rangle = \begin{cases} |\downarrow\rangle\,|\downarrow\rangle \\ \frac{1}{\sqrt{2}}(|\uparrow\rangle\,|\downarrow\rangle + |\downarrow\rangle\,|\uparrow\rangle) \\ |\uparrow\rangle\,|\uparrow\rangle \end{cases}$$

$$|S_{\text{singlet}}\rangle = \frac{1}{\sqrt{2}}(|\uparrow\rangle\,|\downarrow\rangle - |\downarrow\rangle\,|\uparrow\rangle)$$

The lowest energy state in which two spins are paired up into a singlet is called a dimer or a valence bond state. The states that can be formed using only valence bond states are called valence bond crystals. Using the fusion rules, this can be written as,

$$\frac{1}{2} \otimes \frac{1}{2} = 0 \oplus 1. \tag{1.31}$$

The spin-0 in the above equation corresponds to the singlet, and the spin-1 corresponds to the spin-triplet. The singlet corresponds to a featureless paramagnet whose expectation values with respect to any of the SU(2) generators is always zero. Since every element of the SU(2) can be obtained from the generators J_k through equation (1.15), the singlet state is invariant under the action of an element in the SU(2) group and is said to be SU(2) symmetric. Similarly, an operator is said to be SU(2) symmetric if it commutes with the SU(2) generators, i.e,

$$[O, J^\alpha] = 0. \tag{1.32}$$

Such operators are invariant under the action of any SU(2) rotation, i.e., $U_{\boldsymbol{\theta}}^\dagger O U_{\boldsymbol{\theta}} = O$. The Heisenberg Hamiltonian is an example of SU(2) symmetric Hamiltonian.

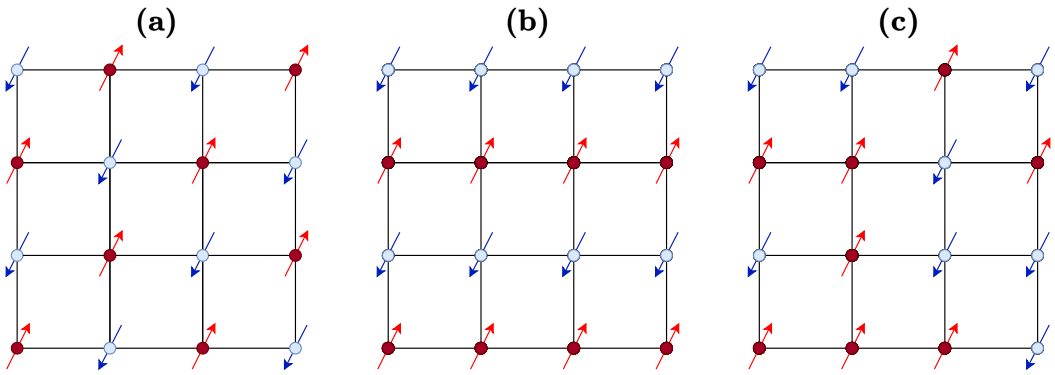

FIGURE 1.1: Ground states of antiferromagnetic models. (a) the Néel state antiferromagnetic phase. (b) Collinear order anti-ferromagnetic phase (c) Paramagnetic disordered phase.

1.2 Magnetic and non-magnetic phases

Once the nature of the quantum mechanical spin is understood, we proceed to look at the effects of many-body interactions in quantum spin systems. In this section, we shall discuss various kinds of magnetic orders or spin liquid phases that can arise through such interactions. In particular, we are interested in the ground states of the local spin Hamiltonians on two-dimensional lattices.

1.2.1 Spontaneous symmetry breaking

Before we move to more complicated phases, we shall first summarize simple magnetic phases involving spontaneous symmetry breaking. The simplest ground state one can think of in this context is the ground state of the Ising model. The ferromagnetic (FM) Ising model has two-fold degenerate ground states in which all the spins point in the same direction. The antiferromagnetic (AFM) model has two Néel configurations as the ground state, in which the spins of the square lattice are organized into a bipartite lattice with spins in each sublattice point in the opposite direction, as shown in figure 1.1-(a). In both these states, at high temperatures, thermal fluctuations help the individual spins over the energy barrier to behave independently. Due to this, there is an absence of long-range order. As we reduce the temperature, this $\mathbb{Z}_2$ symmetry is spontaneously broken, giving rise to one of the two possible ground states [18]. Once the symmetry is broken, the system cannot transition into the other ground state because of the diverging energy barrier. The transitions from the disordered high-temperature state to the ordered ground state that are governed by the thermal fluctuations are well understood by Landau's theory of phase transitions.

However, at lower temperatures, quantum fluctuations dominate. Additionally, in systems governed by Hamiltonians with continuous symmetries, the Mermin-Wagner theorem prevents long-range order from forming in one and two-dimensional materials at finite temperatures [19] and the system is always disordered above 0 K. Hence, in order to get a long-range order, we have cool the system down to zero Kelvin, where quantum fluctuations are much more significant.

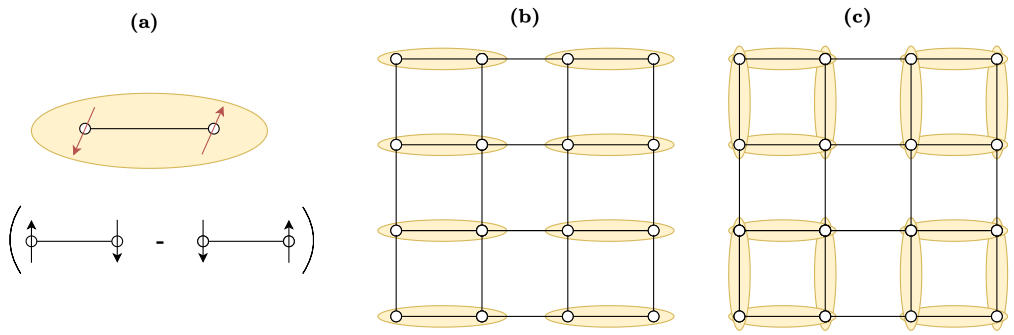

FIGURE 1.2: (a) A visual representation of spin-singlet $\frac{1}{\sqrt{2}}(|\uparrow\rangle|\downarrow\rangle - |\downarrow\rangle|\uparrow\rangle)$ that shall be used in the rest of the thesis. (b) & (c) A columnar state and a plaquette state - two distinct valence bond crystal (VBC) configurations made up of periodically arranged spin-singlets. VBCs do not break the SU(2) symmetry but break the translational symmetry of the lattice.

As we have seen, between two particles under Heisenberg interactions, the minimum energy is achieved when the particles form a singlet. Configurations that contain purely singlet bonds which are arranged periodically, are called *Valence Bond Crystals* (VBCs). These VBCs are SU(2) symmetric and break the lattice symmetry. Since the system has to flip several singlets to attain one valence bond configuration from another, there is a significant energy cost for the system to fluctuate between the valence bond configurations. This energy barrier prevents local excitations in such VBC phases at low temperatures, and hence the VBCs can be considered a "spin-solid" phase.

1.2.2 Frustrated systems

The lattice symmetry that is broken by the VBCs can be restored if we consider a state that is a superposition of several singlet configurations. In such states, the SU(2) symmetry and the spacial symmetries remain intact. Yet these states are quite different from the high-temperature disordered paramagnetic phases. Since they are superpositions of several singlet configurations, they possess high degree of entanglement without showing any long-range order. Quantum states like these, which are highly entangled but exhibit no particular long-range ordering or symmetry breaking, are called *Quantum Spin Liquids (QSLs)* [20].

One of the key ingredients of a spin system to realize such a state is *magnetic frustration*. A magnetic system is said to be *frustrated* if it possesses competing interactions that cannot be simultaneously satisfied [21]. As a result, the ground states of frustrated magnets often exhibit extreme degeneracies that do not result in an ordered state even at absolute zero temperature.

Consider a system of spin-$\frac{1}{2}$ particles on a triangular lattice with nearest-neighbour Heisenberg interactions. The Hamiltonian of each unit cell is given by,

$$H_\Delta = J(\mathbf{S}_1 \cdot \mathbf{S}_2 + \mathbf{S}_2 \cdot \mathbf{S}_3 + \mathbf{S}_3 \cdot \mathbf{S}_1). \tag{1.33}$$

The total spin operator and the total spin-z operator are given by,

$$\begin{aligned} \mathbf{S}_\Delta &= (\mathbf{S}_1 + \mathbf{S}_2 + \mathbf{S}_3) \\ S_z &= (S_1^z + S_2^z + S_3^z). \end{aligned}$$

The resultant spin can be calculated from the fusion rules

$$\frac{1}{2} \otimes \frac{1}{2} \otimes \frac{1}{2} = \frac{1}{2} \otimes (0 \oplus 1) = \frac{1}{2} \oplus \frac{1}{2} \oplus \frac{3}{2}. \tag{1.34}$$

The spins-$\frac{1}{2}$ and spin-$\frac{3}{2}$ have an energy of $-\frac{3J}{4}$ and $-\frac{15J}{4}$ respectively. The eigenstates corresponding to the spin-$\frac{1}{2}$ are,

$$\begin{aligned} |S = \frac{1}{2}; S_z = \frac{1}{2}\rangle_1 &= \frac{1}{\sqrt{2}}[|\uparrow\downarrow\uparrow\rangle - |\downarrow\uparrow\uparrow\rangle] = \frac{1}{\sqrt{2}}(|\uparrow\downarrow\rangle - |\downarrow\uparrow\rangle) \otimes |\uparrow\rangle \\ |S = \frac{1}{2}; S_z = -\frac{1}{2}\rangle_1 &= \frac{1}{\sqrt{2}}[|\downarrow\uparrow\downarrow\rangle - |\uparrow\downarrow\downarrow\rangle] = \frac{1}{\sqrt{2}}(|\uparrow\downarrow\rangle - |\downarrow\uparrow\rangle) \otimes |\downarrow\rangle \\ |S = \frac{1}{2}; S_z = \frac{1}{2}\rangle_2 &= \frac{1}{\sqrt{6}}[|\uparrow\downarrow\uparrow\rangle + |\downarrow\uparrow\uparrow\rangle - 2\,|\uparrow\uparrow\downarrow\rangle] \\ |S = \frac{1}{2}; S_z = -\frac{1}{2}\rangle_2 &= \frac{1}{\sqrt{6}}[|\downarrow\uparrow\downarrow\rangle + |\uparrow\downarrow\downarrow\rangle - 2\,|\downarrow\downarrow\uparrow\rangle]. \end{aligned}$$

The first two sets of states correspond to a singlet on one of the bonds, and the remaining states correspond to a superposition of the singlets on the other two bonds. The lack of diverging energy barrier between the degenerate ground states implies that the system can never choose to settle down to a particular configuration, even at zero temperature. This degeneracy only increases with the number of particles. Unlike the AFM Ising model on a square lattice, where the degenerate states are obtained by a global $\mathbb{Z}_2$ rotation, the degeneracy of frustrated models occurs at a local level. One can obtain a new ground state configuration by altering a few singlets. This implies that quantum fluctuations, which drive the system between two or more equivalent configurations, are much more prevalent and prevent the state from attaining a single unique configuration. They are made up of singlets, so they do not break SU(2) symmetry. They do not break the lattice symmetries as they fluctuate between multiple degenerate states. We also notice that some lattices, such as triangular lattice or Kagomé lattice, naturally lead to frustration because of their geometry, we can also have frustration in simpler lattices by enforcing competing interactions. For a square lattice, this involves adding next-to-nearest neighbor interactions, as shown in figure 1.3-(b).

One of the earliest proposals for QSL came in the form of Resonating Valence Bond (RVB) state from PW Anderson, who proposed it as a possible ground state for the Heisenberg Hamiltonian on a triangular lattice [22]. It is based on the equal weight superposition of all possible singlet configurations. While it has been shown that such an RVB state cannot be the ground state of the Heisenberg Hamiltonian on a triangular lattice [23], short-range parent Hamiltonians have been constructed that have such states as their ground states. Notice that these parent Hamiltonians naturally have SU(2) symmetry embedded in them and can be categorized into *gapped*

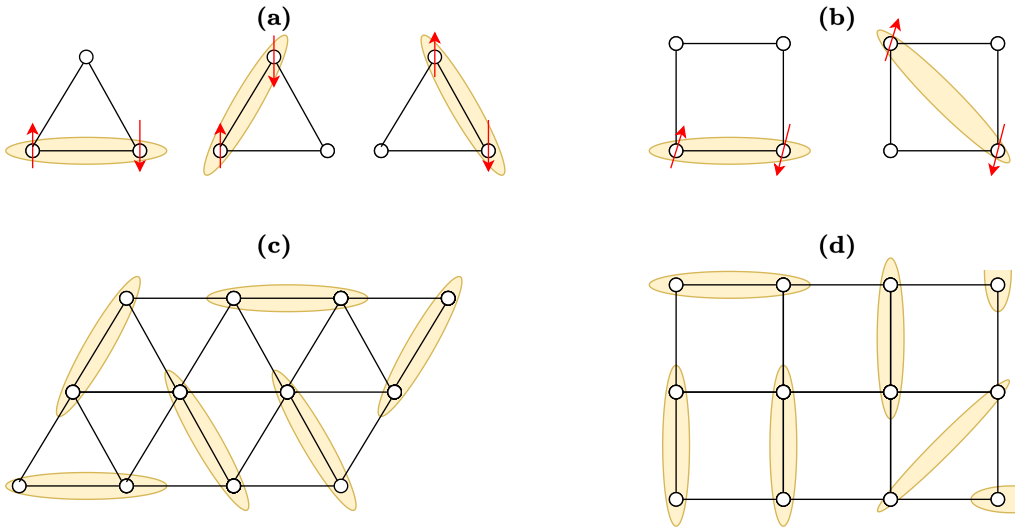

FIGURE 1.3: Magnetic frustration. (a) Eigenstates of spin in a triangular unit cell. Each configuration minimizes the energy along the singlet bond but leaves the other two bonds unsatisfied. (b) Frustration in a square lattice unit cell. The frustration is due to the competition between the singlets along the edge of the square and the singlets along the diagonal. (c) A random valence bond (VB) configuration in a triangular lattice. (d) A random valence bond configuration in a square lattice. Quantum spin liquids can be constructed by a linear superposition of several VB configurations such that no symmetry is broken.

Hamiltonians and *gapless* Hamiltonians based on the excitation energy gap between the ground states and the lowest excited states.

The identification of quantum spin liquids in naturally occurring materials is quite challenging because of their general lack of ground state order. As of now, several possible candidate materials [24–26] that have some confirmed signatures of spin liquids, such as $ZnCu_3(OH)_6Cl_2$(Herbertsmithite), $(Cu_3V_2O_7(OH)_2 2H_2O)$ (Volborthite) and Vesignieite $(BaCu_3V_2O_8(OH)_2)$ exist [25, 27, 28].

Gapped and gapless spin liquids

Consider a Hamiltonian whose ground state can be described by one of the magnetic phases described above. The Hamiltonian and the corresponding ground states are said to be gapless if the excitation spectrum is continuous. Note that gapless phases can only exist in the thermodynamic limit. Finite systems always exhibit a gap in the excitation spectrum which vanishes as we move to the thermodynamic limit. These gapless states are usually present at quantum critical points where quantum fluctuations are scale-invariant, and the system exhibits algebraically-decaying correlations.

$$\langle \mathbf{S}_i \cdot \mathbf{S}_j \rangle \sim |r_i - r_j|^{\eta}. \tag{1.35}$$

A good example of such a gapless state is the ground state of AFM Heisenberg Hamiltonian with nearest and next-to-nearest interactions (the $J_1 - J_2$ Hamiltonian) with $J_2 = 0.5J_1$ [29]. This Hamiltonian has Néel state and collinear AFM states as

its ground states when $J_1 \gg J_2$ and $J_2 \gg J_1$, respectively. Here $\frac{J_2}{J_1}$ can be considered to be the parameter λ. When $\lambda_c = \frac{J_2}{J_1} = 0.5J_1$, it becomes maximally frustrated and the ground of the system becomes a gapless spin-liquid. Note that the actual phase diagram is extremely controversial as different methods have resulted in different conclusions with no particular consensus. The only general agreement is that the system undergoes a transition from Néel state to a spin-liquid for some $0.4 < \frac{J_2}{J_1} < 0.5$ before transitioning into a collinear AFM phase for some $0.5 < \frac{J_2}{J_1} < 0.6$. It is also generally agreed that the spin-liquid state undergoes a transition into a VBC before transitioning into a collinear AFM phase.

On the other hand, a Hamiltonian is said to be gapped if its energy spectrum exhibits a non-zero gap between the ground and the first-excited states in the thermodynamic limit. As a consequence, the ground states have exponentially decaying correlations.

$$\langle \mathbf{S}_i \cdot \mathbf{S}_j \rangle \sim e^{-|r_i - r_j|/\xi}. \tag{1.36}$$

As explained earlier, the parent Hamiltonians of all VBCs are gapped. Gapped spin liquids differ from VBCs in the fact that they do not break lattice symmetries.

For a given Hamiltonian, there is no guaranteed way of analytically finding if the ground state is gapped or gapless. Finding the nature of the ground state of a given Hamiltonian is tedious that has received extreme attention. Things are much clear for 1D spin chains. The energy eigenstates of a system of spin-$\frac{1}{2}$ particles under Heisenberg Hamiltonian are calculated from Bethe ansatz and are found to be gapless. Haldane, in 1983, showed that the nature of the excitation spectrum of a spin chain depends on the spin quantum number S [30, 31]. If the system contains half-odd integer spins, the ground state is unique and gapless, whereas if the system contains integer spins, the ground state is unique and gapped. A more generalization of the properties of a spin chain is given by the Lieb-Schultz-Mattis-Hastings (LSM) theorem [32]. The LSM theorem states that a SU(2) symmetric periodic 1D spin chain with half-integer spin has a vanishing gap between the ground and the first excited state in the thermodynamic limit. This implies that the system is either gapless or has a degenerate set of ground states. This result is later extended to two dimensions by Oshikawa [33] and Hastings [34].

1.2.3 AKLT states

Haldane, in 1983 [31], showed that integer spin chains exhibit a unique gapped ground state under bilinear spin interactions. This implies that the said ground states have to be singlets. Such gapped ground states of integer spin chains preserve the SU(2) symmetry of the parent Hamiltonian are the characteristics of the Haldane phase.

$$H_{\mathrm{BL}} = \sum_{i=0}^{N-1} [\alpha \mathbf{S}_i \cdot \mathbf{S}_j + \beta (\mathbf{S}_i \cdot \mathbf{S}_j)^2]. \tag{1.37}$$

One such ground state belonging to the Haldane phase is the AKLT state proposed by I. Affleck, T. Kennedy, E. Lieb, and H. Tasaki in 1987 [35]. The state is made up

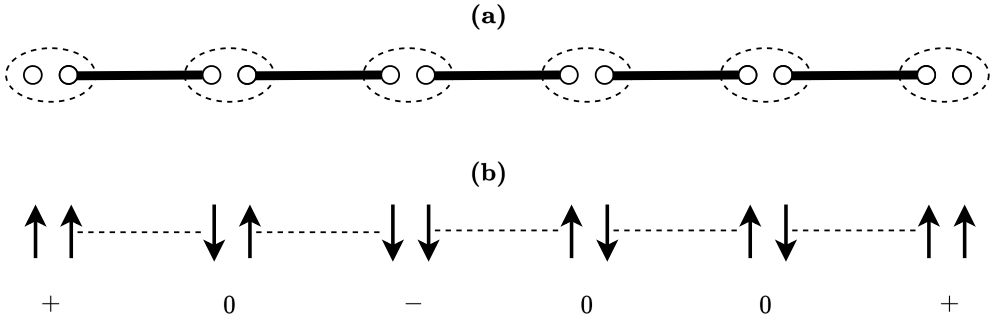

FIGURE 1.4: AKLT state in 1D. (a) The spin-1 AKLT state can be written be broken down as a VBS state of spin-$\frac{1}{2}$ particles. The thick lines indicate singlet states, and the dashed lines represent the projection of 2 spin-$\frac{1}{2}$ particles into the spin-1 space. (b) A specific configuration of spins of the AKLT state. The dashed lines indicate a singlet. Notice that this implies that two $S_z = +1$(indicated by a + and two spin-ups) states will always be separated a $S_z = -1$(indicated by a - and two spin-downs) and vice-versa.

of a spin-1 chain whose Hamiltonian acts on two adjacent spin-1 sites and projects it onto a spin-2 state. We know that a general projection operator of two sites onto a spin-S state is given by,

$$\begin{aligned}\mathcal{P}_{i,i+1}^{(s=2)}(\mathbf{S_i}, \mathbf{S_{i+1}}) &= \prod_{s' \neq s}[(\mathbf{S_i} + \mathbf{S_{i+1}}) - s'(s'+1)] \\ &= [2\mathbf{S_i} \cdot \mathbf{S_i} + 4 - 0(0+1)][2\mathbf{S_i} \cdot \mathbf{S_i} + 4 - 1(1+1)] \\ &= [4(\mathbf{S_i} \cdot \mathbf{S_i})^2 + 12\mathbf{S_i} \cdot \mathbf{S_i} + 8]. \end{aligned} \tag{1.38}$$

Upon normalizing, we get,

$$H_{AKLT}^{1D} = \sum_i \mathcal{P}_{i,i+1}^{(2)}(\mathbf{S_i}, \mathbf{S_{i+1}}) = [\frac{1}{6}(\mathbf{S_i} \cdot \mathbf{S_i})^2 + \frac{1}{2}\mathbf{S_i} \cdot \mathbf{S_i} + \frac{1}{3}]. \tag{1.39}$$

The AKLT Hamiltonian can thus be written in terms of a general bi-linear Heisenberg Hamiltonian given by $\alpha = 1$ and $\beta = \frac{1}{3}$. Based on Haldane's conjecture, the ground state should thus be a gapped valence bond state. The ground state of this Hamiltonian is a valence bond state which is made of singlets between two neighboring sites. One can construct this wavefunction from a set of simple tensor products of spin-$\frac{1}{2}$ singlets and then use a projection operator that projects two spins from spin-1 space to spin-$\frac{1}{2}$ space as shown in. A detailed representation of this state is given in section 2.1.

If we look at each configuration of individual spins that make up this state, we can observe that even though there is no clear long-range order, there is a hidden anti-ferromagnetic order. The enforcement of singlets implies that any two spins with $S_z = +1$(-1) will always be separated by a $S_z = -1$(+1) state and an arbitrary number of $S_z = 0$ states. The final AKLT state is the superposition of all such possible configurations. The randomness of $S_z = 0$ will prevent any long-range order and maintain the spin-liquid nature of the state.

Now consider a trivial product state that is made up of the tensor product of spins in S_z basis $|\psi_{\text{trivial}}\rangle = |\uparrow\rangle \otimes |\uparrow\rangle \otimes ... \otimes |\uparrow\rangle$. The parent Hamiltonian of these states is given by $H_{\text{trivial}} = \sum_i (S_i^z)^2$. We shall now construct a one-parameter interpolation Hamiltonian that connects the AKLT Hamiltonian to the trivial state.

$$H(\lambda) = \lambda H_{\text{AKLT}} + (1-\lambda) H_{\text{trivial}}, \tag{1.40}$$

with $\lambda \in [0, 1]$. In both limits, $s \to 0$ and $s \to 1$, the ground state of the Hamiltonian has a ground state that is gapped and has time-reversal and translational symmetry. However, to go from the AKLT to the trivial state, the Hamiltonian must pass a critical point with a vanishing energy gap. Unlike the Landau-type phase transitions, the lack of symmetry breaking and a conventional order parameter in this transition implies that the transition is topological in nature. This implies that the AKLT state is 'symmetry protected' from the trivial phase, in the sense that it cannot be smoothly connected without undergoing a critical transition [36]. In general, Haldane phases with half-integer spins are protected by either $\mathbb{Z}_2 \times \mathbb{Z}_2$ symmetry or bond-reflection symmetry or time-reversal symmetry and belong to a class of gapped states called Symmetry Protected Topological (SPT) phase [37, 38].

The results of the one-dimensional AKLT model can be generalized to higher dimensions. In any dimension, AKLT states are ground states of particularly simple Hamiltonians that only have nearest neighbor two-site interactions, are rotationally invariant in spin space, and share all spatial symmetries of the underlying lattice [39, 40]. The Hamiltonian can be constructed from a projection operator which projects z spins onto a higher dimensional subspace where z is the coordination number of the lattice. Hence, the AKLT model on a square lattice consists of a Hamiltonian that projects four spin-$\frac{1}{2}$ particles onto a spin-2 subspace. The Hamiltonian is given by

$$H_{\text{AKLT}} = \frac{15}{48}\left(I + \frac{1}{3}\sum_{i,j\in S_4} (\mathbf{S}_i \cdot \mathbf{S}_j) + \frac{1}{5}\sum_{(i,j),(k,l)\in S_4} (\mathbf{S}_i \cdot \mathbf{S}_j)(\mathbf{S}_k \cdot \mathbf{S}_l) \right), \tag{1.41}$$

where S_4 is the permutation operator in a plaquette. The ground state consists of a tensor product of four singlets as shown in figure 1.5. In any lattice, the state always has a gapped bulk and exhibits gapless edge excitations. In lattices that have odd half-integer spins per unit cell, the two-dimensional generalization of the LSM theorem holds. In cases where the theorem does not hold true, the system has a non-degenerate ground state belonging to the SPT phase [39, 41]. The results have been generalized to other SU(N) models in both 1D [42] and 2D [43].

1.2.4 Topological order

Quantum states that break conventional orders, such as VBCs, have an order parameter associated with them. If $|i\rangle$ denotes a set of degenerate ground states for $i = 1, 2, ...d$, one can form a normalized linear combination of such states. $|a\rangle = \sum_i a_i |i\rangle$ and $|b\rangle = \sum_i b_i |i\rangle$. If we can construct a local operator $\hat{O}$ such that it has different expectation values for $|a\rangle$ and $|b\rangle$, $\langle a| \hat{O} |a\rangle \neq \langle b| \hat{O} |b\rangle$, then $\langle \hat{O} \rangle$ is an order parameter for the said broken symmetry. However, in systems such as spin liquids where no local order exists, the systems can have global excitations, which appear in the form of ground

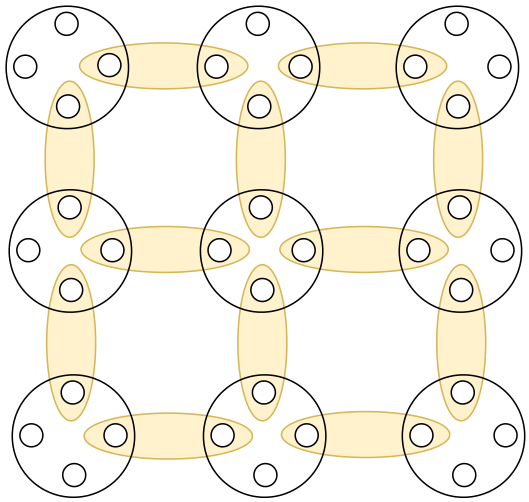

FIGURE 1.5: The 2D AKLT model on a square lattice. Each site on the lattice has a spin-2 particle which can be decomposed into four spin$\frac{1}{2}$ particles that form singlets with the neighbouring sites. in a generalized SU(N) AKLT model, the spin-$\frac{1}{2}$ singlets are replaced by SU(N) singlets.

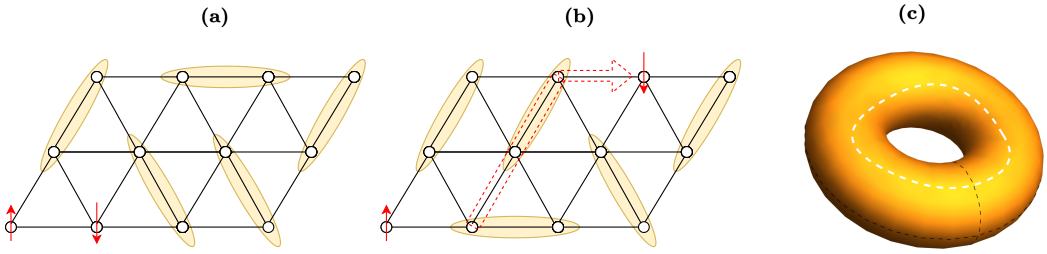

FIGURE 1.6: (a) Spinon excitations that resulted from breaking a singlet bond into two independent spins. (b) A deconfined spinon. The dashed line represents a possible path along which the valence bonds are broken due to the deconfinement of the spinon. If the spinon hops back to the initial point and annihilates with the partner spinon the resultant state is a ground state. (b) A 2d lattice with periodic boundary conditions resulting in a torus geometry. The dotted lines indicate non-contractable loops along which we can apply a string operator, indicative of a spinon path.

state degeneracy. A system is said to have topological order if the number of such global excitations (i.e., the groundstate degeneracy) depends on the topology of the system in the seminal works of X.G.Wen [44, 45].

In order to better understand the nature of topological order, it is essential to understand one of the vital and exciting features of quantum spin liquids which is the existence of non-local fractional excitations called *spinons*. Such excitations typically involve breaking valence bond singlets into a pair of free spins. Each individual spinon can form a singlet with one of the neighboring spins creating a new configuration and shifting the spinon to one of the neighbors as shown in figure 1.6. Hence these spinons can be considered individual quasi-particles that carry the spin of the electron but not its charge. In a VBC state, as we move the spinons apart, it deforms

the configuration along its path, breaks the established order of the VBC, and introduces energetically unfavorable bonds. This implies that we cannot move the spinons far apart without providing diverging excitation energy and hence they cannot exhibit fractionalized excitations. This is not true for spin liquids as they do not have any local order that the spinons can break. A system is said to be fractionalized if there is no energy cost to move the spinons far apart [46].

The relationship of spinons with topological order can be understood from the following example. Consider an RVB spin liquid that can host spinon excitations and has a periodic boundary in at least one dimension, such as a cylinder or torus. Let $|1\rangle$ be a ground state where a pair of spinon excitations are created and moved around the periodic boundary and are then annihilated to return a new state $|2\rangle$. At each intermediate step, the system contains two spinons which can be viewed as the original spinon-free state with a set of string operators that act along the path of the spinons, connecting them. Thus, even though they can be separated, they are always connected. When the spinons are annihilated, the resultant state $|2\rangle$ is equal to a set of closed-loop string operators acting on the initial state $|1\rangle$. If the surface is closed, the string operators can be adiabatically connected and annihilated, implying the states are identical. However, for topologies with a non-zero genus, such as a torus, we can have non-contractable closed loops. In such cases, the two states are distinct and are connected by spinless excitations. Note that the original state $|1\rangle$ can be restored by applying the same string operator on the resultant state $|2\rangle$ implying that the operator is an element of the $\mathbb{Z}_2$ group. These spinless excitations, which are fluxes of a $\mathbb{Z}_2$ gauge field, are called visons. [47]. All the short-ranged valence bond configurations can thus be sorted according to the parity operator $P_x = \pm 1$ of their number of singlets crossed along the path of the vision.

$$P_x = (-1)^{N_x}. \tag{1.42}$$

Where the operator N_x counts the number of singlets in the vison path along the x-direction. P_x is a topological invariant that cannot be changed by any local operator but is used to distinguish two different topological sectors of the ground states. If the lattice is a torus, we have an additional dimension for the creation of non-contractable vison excitations. Hence, we can have an additional parity operator $P_y = \pm 1$, increasing the number of topological sectors to four. In each sector of such an RVB state, we can find different ground states that have identical properties but cannot be probed by an order parameter and hence possess topological order [48]. Note that such construction is not possible on a flat two-dimensional surface with open boundary conditions. Since these arguments are independent of the lattice arrangement and depend only on the topology, this argument can be extended to any degenerate spin liquid with non-trivial topology. The degeneracy is guaranteed by the two-dimensional generalization of the LSM theorem for systems with half-integer spin per unit cell [34]. In that case, a fully gapped state with robust groundstate degeneracy on a torus with no symmetry breaking is always topologically ordered.

1.2.5 Entanglement entropy and area law

The spin liquids and other exotic phases that have been discussed so far are all ground states of local Hamiltonians. We shall discuss a property called the area law that

these ground states generally hold true.

Entanglement entropy is a measure of the information shared between two complementary regions of a many-body system. Mathematically, it is the von Neumann entropy of the reduced density matrix of the substem. If we partition a system of a large number of particles into two subsystems A and B, the corresponding reduced density matrices ρ_A and ρ_B contain all the information of the system within that region. The reduced density matrix ρ_A is given by,

$$\rho_A = \mathrm{Tr}_B(\rho) = \sum_{j\in B} (I_A \otimes \langle j|)\, |\psi\rangle \langle\psi|\, (I_A \otimes |j\rangle)$$

where ρ stands for the overall density matrix of the system $\rho = |\psi\rangle \langle\psi|$. The entanglement entropy is then given by,

$$S(\rho_A) = -\mathrm{Tr}[\rho_A \ln(\rho_A)] = -\mathrm{Tr}[\rho_B \ln(\rho_B)] = S(\rho_B). \tag{1.43}$$

This entanglement entropy can be used to understand the amount of information exchanged between the two subsystems. For a random state within the Hilbert space of the system, the Page conjuncture states that the entanglement entropy usually grows as a volume law [49], i.e., the entanglement entropy is proportional to the number of particles contained within the sub-system A. For low energy states, however, the entanglement entropy follows the so-called *area law* [50, 51], which is generally used to separate the relevant states from the irrelevant ones. A quantum mechanical state is said to obey the area law if it satisfies the following condition. *If a system of particles can be broken down into two complementary subsystems A and B, then the upper bound of the entanglement entropy is proportional to the number of particles on the boundary of the subsystem A, i.e.,* $S_A = O(|\partial A|)$.

It has been explicitly proven in one-dimensional systems that the ground states of all gapped Hamiltonians [52], including the ones that have long-range terms, obey the area law [53]. Gapless critical states in one-dimensional systems seem to have a logarithmic correction term to the area law, whereas some classes of gapless states are shown to have a square-root correction term [54]. While no such rigorous proof exists in two dimensions, there has been no contradicting numerical evidence either, and it is expected to be valid for most local and gapped Hamiltonians. We shall show later that the PEPS ansatz that is used in this work naturally obeys the area law and hence is very useful in capturing the relevant portion of the Hilbert space to simulate strongly correlated systems.

1.3 Quantum simulators

Now that we have discussed the basics of quantum spin systems and the exotic phases that can arise from many-body interactions of quantum spin systems, we shall move on to the hot topic of experimentally simulating such exotic phases of matter. The field of experimentally realizing complex states of matter using cold atoms was pioneered by Eric Cornell and Carl Wieman in 1995 when they reported the first experimental evidence of Bose-Einstein condensate (BEC) using ^{87}Rb atoms [55]. In the same

year, Wolfgang Ketterle's team reported BEC of sodium atoms [56]. Since then, a significant amount of research has gone into implementing experimental protocols to simulate strongly correlated systems using cold atoms. We now describe two such experimental setups that provide motivation to tackle the research problem discussed in this thesis.

1.3.1 Optical lattice

One of the key experimental techniques in such cold-atom simulators is the creation of a cold-atom optical lattice [57–59]. It typically involves detuning a laser light such that it is far from the resonance wavelength of the atoms. As a result, the atoms do not absorb the photons and hence do not experience heating. When two counter propagating lasers combine to form a periodic standing wave, the resultant electric potential acts as a lattice. At low enough temperatures, atoms are confined in the minima of the periodic electric potential as shown in figure 1.7. The behavior of the confined atoms in such a potential is similar to the electrons in a crystalline solid. The depth of the electric potential can be tuned by changing the intensity of the laser, which allows us to control the dynamical motion of the atoms which hop from one minima to the other via quantum tunneling. When the potential is high, the tunneling effect is at its minimum, and the system behaves like an insulator and can be used to simulate Mott insulators. It has to be noted that the nature of the atoms used in the simulators has a significant effect on the outcome of the simulation. We can use different isotopes to change the nature of simulations. For example, Ytterbium has seven isotopes, of which two are fermions and the rest are bosons. Another popular choice for bosonic cold atom simulations is Rubidium-87 and has been in use from the early days of ultra-cold atomic simulations.

While they have been successful in uncovering some new insights about the nature of Hubbard models [60–65], the major drawback of this method is that the trapping potential is usually very weak. Hence in order to trap the atoms, the temperature has to be cooled down to

1.3.2 Rydberg blockade

A Rydberg atom simulator is a type of quantum simulator that uses magnetic traps or optical tweezers to form an array of Rydberg atoms and then uses a laser-powered optical pump to simulate the dynamics of a highly entangled many-body state [66–69]. Rydberg atoms are atoms in an excited state which have one or more electrons in a state with a very high principle quantum number n. The interaction strength between two such Rydberg atoms scales with n and is several orders of magnitude higher than the interaction strength of two ground-state atoms. This makes them a likely candidate to simulate long-range interactions. The key idea in the Rydberg blockade is the concept of dipole-blockade [70–73]. If we shine a laser onto an individual atom with the right frequency ω_0, we can drive an electron from the ground state $|g\rangle$ to an excited state $|r\rangle$. If the frequency does not match the energy gap, the interaction does not take place. The Rabi frequency of the two levels gives us information about the effect of the laser on the isolated atom, $\omega = \langle g| (-\mu \cdot E) |r\rangle$. The principle of

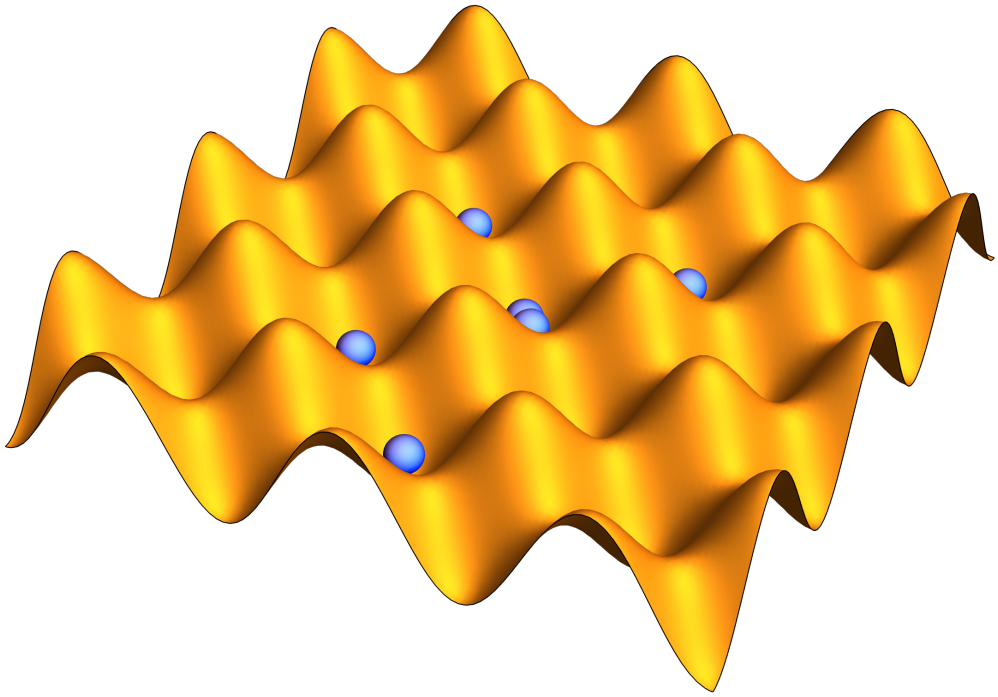

FIGURE 1.7: Optical lattice in an ultracold atomic simulator setup. The lattice is constructed from standing waves formed by six laser sources in 3 dimensions. At extremely low temperatures (in the order of nK), the atomic gases occupy the troughs of the optical lattice. The intensity of the laser controls the amount of tunneling that can take place through the electric potential barrier and can thereby be used to control the amount of hopping between various lattice sites.

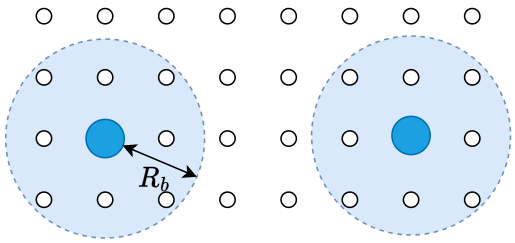

FIGURE 1.8: A typical Rydberg blockade arrangement with the blockade radius R_b marked. All the Rydberg atoms within R_b are blocked from getting excited. The excited atom can be considered as an entangled singlet and the condition that the R_b covers two lattice points can be used to enforce the condition of one dimer per lattice site.

dipole blockade is that the excitation of one Rydberg atom shifts the energy level of the remaining Rydberg atoms by $V(R)$. All the atoms that are within a certain blockade radius, R_b, have their energy levels shifted enough to bring them out of resonance from the laser frequency. Thus, the excitation of one Rydberg atom blocks the excitation of the atoms nearby. The Hamiltonian of the system is then given by,

$$H_{Ryd} = \frac{\omega}{2}\sum_i(\sigma^i_{gr} + \sigma^i_{rg}) - \delta\sum_i \sigma^i_{rr} + \frac{1}{2}\sum_{i,j} V_{ij}\sigma^i_{rr}\sigma^j_{rr}, \tag{1.44}$$

where $\delta = \omega_0 - \omega_{gr}$ is the detuning of the laser, i and j are site indices, $V_{ij} = V(R_{ij})$ and R_{ij} is the distance between sites i and j, and $\sigma^i_{\alpha\beta} = |\alpha_i\rangle\langle\beta_i|$ $(\alpha_i, \beta_i = e, r)$ is the projection operator. If R_b is large enough, the potential V_{ij} is given by the Van der Waals force $V_{ij} \sim (\frac{R_b}{R_{ij}})^6$.

Since each excited Rydberg atom can take only two possible states $|g\rangle$ and $|r\rangle$, assuming the groundstate has filled electron shells, the basis of excitation states is $|gg\rangle$, $|gr\rangle$, $|rg\rangle$, $|rr\rangle$. Since we only provide enough energy for one transition from $|g\rangle \rightarrow |r\rangle$, the excitation state is given by $(|gr\rangle \pm |rg\rangle)$ which is a singlet and can act as a valence bond. If the blockade radius is large enough to cover two lattice points, we can enforce the one dimer per lattice site constraint as shown in the figure 1.8. Because of the possible long-range interactions and the ability to enforce the dimer constraints, Rydberg atoms are widely being used for simulating spin liquids [74–80]. Note that this is only one form of performing quantum simulations using Rydberg atoms. Several different types of implementations exist [81, 82] and are used depending on the type of problem.

1.3.3 Non-equilibrium dynamics in quantum simulators

This pioneering research paved the way for investigating complex phases of matter. The next most important step in the evolution of quantum simulators is the observation of the Mott insulator to the superfluid phase transition [83]. Soon other forms of quantum dynamics, like quantum transport, were studied. The theoretical proposal for simulating the Bose-Hubbard model using optical lattices was first presented

in Ref. [84] and was soon followed by an experimental realization in Ref. [83]. Similarly, an experimental scheme for the minimum forms of topologically ordered materials such as the resonating valence bond (RVB) state and Laughlin states was proposed in 2008 in Ref. [85] which led to an experimental realization of RVB states at a plaquette level [86]. Similarly, several models that are hard to find in nature, such as the Haldane phase, have been successfully prepared using cold atoms [87, 88]. Eventually, other forms of quantum simulators, such as trapped ions for spin-$\frac{1}{2}$ models [89, 90], superconducting qubits [91–93], and Rydberg atom simulators for long-range interactions [94–96], have also been developed.

As new protocols and experimental setups are being proposed, the existing simulators have grown in capacity. Programmable simulators with 219 atoms [2], 256 atoms [97], and 289 atoms [98] have been used to prepare topological spin liquids. Apart from simulating strongly correlated materials, the applicability of these quantum simulators in other fields is also being tested, such as understanding molecular reactions, electron transport, machine learning [99–101], and solving computationally hard problems [98], etc.

Most of the theoretical models that are used to describe real magnetic materials, including the ones described earlier in the thesis, are too ideal to be accurate. Ultracold atoms in optical lattices, however, provide an almost perfect playground for the realization of these systems. Since these states are completely controlled by the artificial potential wells, we can abruptly change the interacting Hamiltonian faster than the time scale of the relaxation dynamics of the system. After such a near-instantaneous change in Hamiltonian, called Hamiltonian quench, the expectation values of the generic local observables O become time-dependent. Among such fascinating works, the one that we find most interesting with respect to the content of this thesis is a recently proposed protocol to optimize the preparation of topological spin liquids on Rydberg atoms by Giudici *et al.* in Ref. [102] to realize the RVB state on Kagome lattice (based on the experimental realization of the work done by G. Semeghini *et al.* in Ref. [2]). The proposed protocol targets the preparation of the fixed point of the topological phase (RVB) state of hard dimers. The effective Hamiltonian of the quench protocol is given by equation (1.44). The ansatz proposed to study the dynamics of this state is given by a two-parameter variational tensor network ansatz,

$$|\phi(z_1, z)2)\rangle = \mathcal{N}\mathcal{P}[\bigotimes_{i=1}^{N}(1 + z_2\sigma_+^i)(1 + z_1\sigma_-^i)]\,|\mathrm{RVB}\rangle\,, \tag{1.45}$$

for $z_1, z_2 \in \mathbb{C}$, where $\mathcal{N}$ is a normalization constant, $\mathcal{P}$ is the projector on the sector of the Hilbert space that satisfies the blockade constraint and $\sigma_-^i = |g_i\rangle\langle r_i|$ and $\sigma_+^i = |r_i\rangle\langle g_i|$. For finite values of z_1 and z_2, this ansatz covers a phase of RVB with spinon excitations. Similar PEPS-based tensor network descriptions of Rydberg atom states have also been suggested in Refs. [103, 104].

With growing interest in using PEPS ansatz to study the quench dynamics, it would be interesting to ask some questions that PEPS ansatz can answer. Does the system thermalize and equilibrate to some final state? Will it retain the information of the

initial state? Does the quench lift the local degeneracy? Do the internal symmetries survive? In order to guide the experimental strategies to answer these questions, there have to be some theoretical predictions for these questions. Furthermore, the results of these experiments have to be verified before they can be reliably put to practical use. Currently, efficient numerical techniques to study the quench dynamics exist in one-dimensional systems [6, 105, 106] in the form of tDMRG and MPS, but computing the non-equilibrium dynamics that follow a quantum quench is a tedious task in two-dimensional quantum spin systems [3]. As of now, except for some few-body integrable models [107–109], no reliable numerical techniques exist for two-dimensional systems. Thus, the aim of this thesis is to build numerical tools to simulate the quench dynamics of a closed system of zero-temperature pure states using the framework of tensor networks. The tools shall then be used to study the quench dynamics of the plain-RVB state, which is said to have critical dimer-dimer correlations. While the primary focus is on the dynamics of the RVB state on the square lattice, the tools presented in the thesis could be generalized to other two-dimensional lattices.

Chapter 2

Basics of tensors networks

In this chapter, we shall discuss the basics of tensor networks. For an introduction to the diagrammatics using Penrose notations [110] and the basics of tensors, please refer to the appendix A, For a more comprehensive review, refer to Refs. [111, 112]

2.1 Matrix Product States

2.1.1 Introduction to MPS

One of the major hurdles in studying the physics of quantum many-body systems using numerical methods is the exponential growth of the Hilbert space of the system with the number of particles. In order to circumvent this problem, one has to employ approximation techniques to make the study of such quantum many-body systems feasible. While any approximation prevents us from accessing the entire possible Hilbert space, a good approximation always covers the part of the Hilbert space that is most relevant to a given problem. In the case of ground states of gapped and gapless Hamiltonians in 1-D, the relevant part of the Hilbert space is the set of states that follow the 'area law.'

The general wavefunction describing a system of N particles on a chain is given by

$$|\psi\rangle = \sum_{i_1} ... \sum_{i_N} C_{i_1 i_2 ... i_N} |i_1 i_2 .... i_N\rangle .$$

For a given set of local basis $|i_1\rangle\,|i_2\rangle\,....\,|1_{N-1}\rangle\,|i_N\rangle$, the entire information related to the wavefunction is present in the coefficients of $C_{i_1 i_2 ... i_N}$ which gets extremely hard to describe numerically as the Hilbert space grows exponentially with the number of particles. One way of managing this is using Schmidt decomposition to reduce the massive coefficient into a simple contraction of rank-3 tensors.

Consider a partition of a system into two subsystems A and B whose Hilbert spaces are of dimensions d_A and d_B. The Schmidt decomposition of this partition is given by,

$$|\psi_{AB}\rangle = \sum_i \lambda_i |\phi_i^A\rangle |\phi_i^B\rangle . \tag{2.1}$$

This is equivalent to decomposing a tensor $|\psi\rangle$ into 2 component tensors with orthonormal bases, connected by an auxiliary index i. The dimension of the auxiliary index i is the Schmidt rank which gives us information regarding the entanglement between the two subsystems A and B. If the systems are completely independent with zero entanglement, the size of the auxiliary index would be 1 and the system can be rewritten as a product state. Alternatively, one can use the coefficient tensor to perform the same decomposition. By considering the coefficient tensor as an n-dimensional vector, we can reshape it into a matrix of size $(d_A \times d_B)$. Using SVD, one can perform either an exact or approximate decomposition, creating a new index D. We can repeat this process of tensor decomposition to get a set of rank-3 tensors called the matrix product state (MPS).

$$C_{i_1 i_2 ... i_N} = \lambda_{12}\lambda_{23}...\lambda_{(N-1)N} = \sum_{a_1 a_2 ... a_{N-1}} M^{i_1}_{a_1} M^{i_2}_{a_1 a_2} ... M^{i_{N-1}}_{a_{N-2} a_{N-1}} M^{i_N}_{a_{N-1}}$$

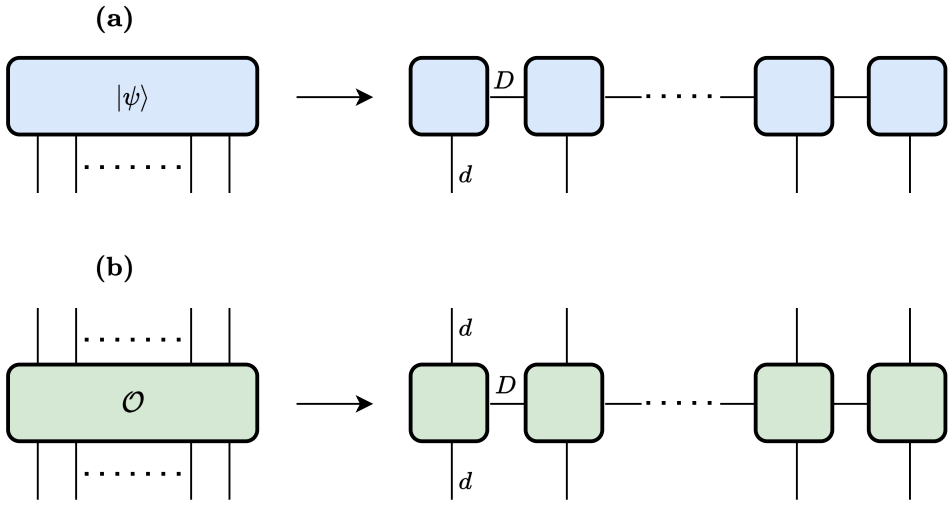

FIGURE 2.1: (a) The tensor decomposition of a 1D wavefunction. The whole translational invariant wavefunction can be represented by a set of rank-3 tensors and two boundary rank-2 tensors. The dimension of the virtual indices D sets the limit of the entanglement entropy that the MPS can capture. (b) The tensor decomposition of a matrix-product operator (MPO).

$$|\psi\rangle = \sum_{i_1 \ldots i_N} \sum_{a_1 a_2 \ldots a_{N-1}} M^{i_1}_{a_1} M^{i_2}_{a_1 a_2} \ldots M^{i_{N-1}}_{a_{N-2} a_{N-1}} M^{i_N}_{a_{N-1}} \tag{2.2}$$

We can extend the same argument to operators and obtain a tensor decomposition called matrix product operator (MPO). The diagrammatic notation of the same is shown in figure 2.1. A typical MPS consists of rank-3 tensors with one physical index d and two virtual indices of bond dimension D. The size of the virtual bond D controls the accuracy of MPS and MPO. For a sufficiently large D, one can cover a larger portion of the Hilbert space and can approximate a given wavefunction with better accuracy. If one were to construct a reduced density matrix from an MPS, the resultant matrix would always have a shape of $(D \times D)$. This implies that the entanglement entropy, which is maximum when the reduced density matrix spectrum is uniform, has an upper bound $S \leq \ln(D)$. Thus the maximum amount of entanglement entropy is given by $\mathcal{S}_{max} = \ln(D)$. Since the boundary length $|\partial A|$ of a 1D system is a constant, the matrix product states naturally obey the area law. Additionally, the rank-3 tensors can be used to enforce the spatial symmetries of the tensor. In order to construct a translationally invariant spin chain, one can use the same rank-3 tensor at every site. From here on, unless otherwise stated, we shall only deal with translationally invariant tensors.

2.1.2 AKLT chain - SU(2) symmetric MPS

In order to explain the construction of SU(2) symmetric matrix product states, we shall use the example of 1D AKLT state.

As explained in section 1.2.3, to construct the ground state of the AKLT Hamiltonian, we break each spin-1 particle into a set of two auxiliary spin-$\frac{1}{2}$ particles. Each auxiliary spin-$\frac{1}{2}$ particle forms a singlet with the auxiliary spin-$\frac{1}{2}$ particles of the neighboring spins such that the overall spin-z component of the wavefunction remains zero as shown in figure 2.2-(a).

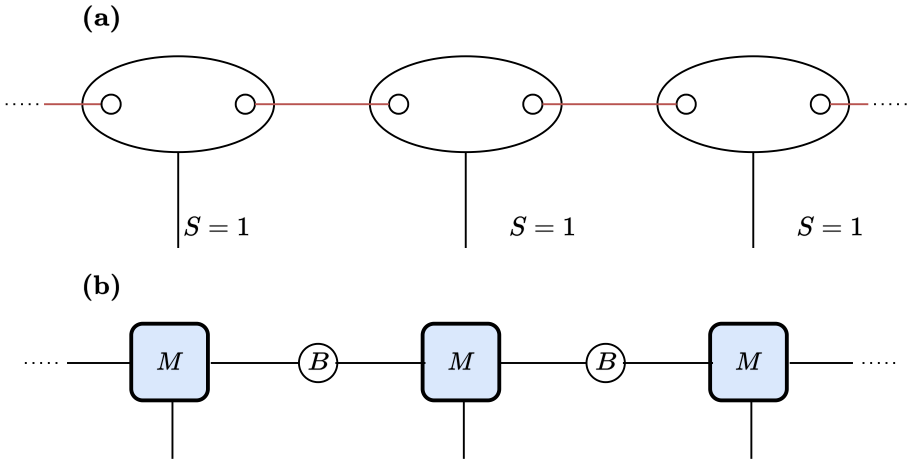

FIGURE 2.2: (a) The construction of the AKLT ground state involving two auxiliary spin-$\frac{1}{2}$ particles (represented by the circles) that form a singlet (represented by a red line segment). (b) The collection of rank-3 MPS that represent the AKLT ground state. The rank-3 tensor M is given by equation 2.4 whereas the bond matrix B is given by equation 2.6.

$$|S=1;\sigma_z\rangle = \begin{cases} |-1\rangle = |\downarrow\rangle\,|\downarrow\rangle \\ |0\rangle = \frac{1}{\sqrt{2}}(|\uparrow\rangle\,|\downarrow\rangle + |\downarrow\rangle\,|\uparrow\rangle) \\ |+1\rangle = |\uparrow\rangle\,|\uparrow\rangle\,. \end{cases} \tag{2.3}$$

Hence, in order to construct a rank-3 tensor, we use the following projector that projects the two spin-$\frac{1}{2}$s onto a spin-1 $\mathcal{M} : (\frac{1}{2} \otimes \frac{1}{2}) \rightarrow 1$ given by,

$$M = \sum_{\alpha,a,b} m_{\alpha ab}\,|\alpha\rangle\,\langle a|\,\langle b| = |-1\rangle\,\langle\downarrow|\,\langle\downarrow| + \frac{1}{\sqrt{2}}\,|0\rangle\,(\langle\uparrow|\,\langle\downarrow| + \langle\downarrow|\,\langle\uparrow|) + |+1\rangle\,\langle\uparrow|\,\langle\uparrow| \tag{2.4}$$

$$M^{(0)} = \begin{pmatrix} 1 & 0 \\ 0 & 0 \end{pmatrix}, \&M^{(1)} = \frac{1}{2}\begin{pmatrix} 0 & 1 \\ 1 & 0 \end{pmatrix}, \&M^{(2)} = \begin{pmatrix} 0 & 0 \\ 0 & 1 \end{pmatrix}. \tag{2.5}$$

The entries of the tensor M are the Clebsch-Gordan coefficients. In order to force the two neighboring auxiliary spins to form a singlet, we introduce a bond matrix B that forms maximally entangled spin singlets.

$$B = \frac{1}{\sqrt{2}}\begin{pmatrix} 0 & 1 \\ -1 & 0 \end{pmatrix}. \tag{2.6}$$

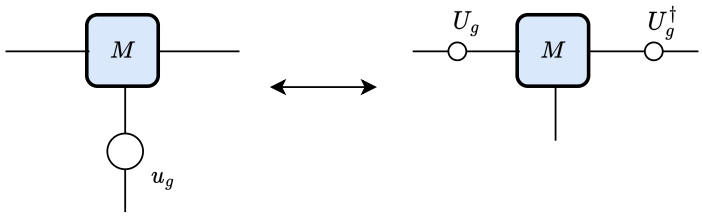

FIGURE 2.3: When an MPS is written as a linear map of irreps, a unitary u_g on the physical index can be replaced by a pair of unitaries U_g and $U_g^\dagger$ in the two virtual indices.

The final AKLT state is then given by the contraction of several such identical rank-3 tensors M with bond dimension $D = 2$ along their virtual indices. Diagrammatically, the MPS tensor of the AKLT state can be represented as shown in figure 2.2-(b).

From this exercise, we conclude that we can construct an SU(2) symmetric wavefunction by

- A linear projector map $\mathcal{M} : \mathbb{C}^D \times \mathbb{C}^D \to \mathbb{C}^d$ that obeys SU(2) fusion rules.
- A bond matrix B that forms singlets between two virtual vector spaces $\mathbb{C}^D$.

In order to construct an SU(2) symmetric MPS with a larger bond dimension D, we simply reduce D as a direct sum of SU(2) irreps and proceed to construct a linear map from the virtual space to the physical space. By ensuring that the linear map complies with the SU(2) fusion rules, we can ensure that the resultant tensor network is invariant under the action of a generator of the SU(2) symmetry group. We now describe an important consequence of one of the *fundamental theorems of MPS* [113] that will be useful later.

Consider a translationally invariant MPS made up of a set of rank-3 tensors $\{M^\alpha_{ij}\}$. If a unitary applied to the physical index leaves the whole state invariant, then the action of the unitary on the physical index can be replaced by a local transformation on the virtual index. Since the bond operator, B, is a real orthogonal matrix, this implies that if we were to absorb two different bond matrices into a single tensor, there should exist a unitary transformation in the physical space that can replace the effect of the transformations in the virtual space of an MPS. This reduces the whole MPS into a bi-partite system, with the odd sites having the unitary transformation and the even sites being unaffected, as shown in figure 2.4. Since there is no bond matrix, the contraction of two tensors via the virtual indices is a simple trace. Since the unitary transformation replaces the bond matrix, which causes the neighboring spins to form a singlet, we deduce that the unitary matrix is $i\sigma_y$ where σ_y is a Pauli spin matrix.

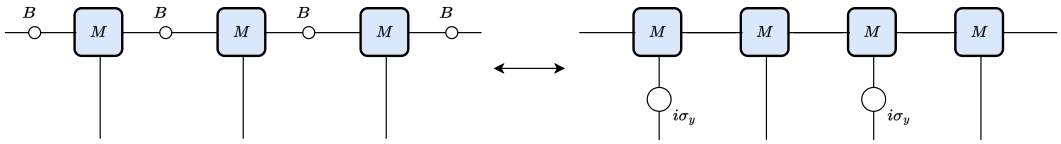

FIGURE 2.4: The bond matrices on each bond can be absorbed into the odd sites, and the resultant effect of the absorption can be replaced by a unitary transformation on the physical index.

2.1.3 Basic MPS operations

Since we have explained how we can construct the MPS of a wavefunction, we shall now see how the MPS can be used to compute the properties of the wavefunction. One of the key objects that one has to compute is the transfer matrix (TM) operator T, shown in figure 2.5-(a). This transfer matrix operator is the inner product of the MPS tensor at a site with its conjugate, leaving the four virtual indices open, which are then reshaped into a matrix of size $(D^2 \times D^2)$. One can also find the transfer operator with an operator sandwiched between the bra and the ket MPS tensors as shown in figure 2.5-(b). For a translationally invariant MPS, the TM is identical for every site up to a change of basis. The total norm of the wavefunction on a N-site ring, i.e., the inner product $\langle\psi|\psi\rangle$ is given by the trace of the product of these transfer matrices.

$$\begin{aligned} T^I_J = T^{ii'}_{jj'} &= \sum_\alpha M^\alpha_{ij} (M^\alpha_{i'j'})^* \\ (T_o)^I_J = (T_o)^{ii'}_{jj'} &= \sum_\alpha M^\alpha_{ij} O_{\alpha\beta} (M^\beta_{i'j'})^* \\ \langle\psi|\psi\rangle &= \mathrm{Tr}(T^N). \end{aligned}$$

Once the norm of the MPS is calculated, the expectation values can be obtained by placing the matrix product operators between the bra and the ket MPS. If one has to apply multi-site operators, one can construct the reduced density operator as shown in figure 2.5-(c) by contracting the bra and the ket tensors of all the sites except the ones on which the operators have to be applied.

The transfer matrix T also gives us information about the correlations of the wavefunction [114]. Since the multi-site correlators involve multiplying the transfer matrix operator T multiple times, we can compute the long-range behavior from the eigenvalues of T. Let t_n be the n-th largest eigenvalue of T. If we normalize the eigenvalues such that the largest eigenvalue is equal to 1, then we can conclude that the largest eigenvector is the only vector that survives in the thermodynamic limit.

Let $|\alpha\rangle$ be the eigenvector corresponding to the eigenvalue t_α, then $T|\alpha\rangle = t_\alpha|\alpha\rangle$. The long range correlation function of an operator O between two sites x and $x+r$ in a spin chain of N spins with periodic boundary conditions is given by,

$$C^o_{x,x+r} = \mathrm{Tr}\left(T^{N-r-1} T_o T^{r-1} T_o\right) / \mathrm{Tr}(T^N). \tag{2.7}$$

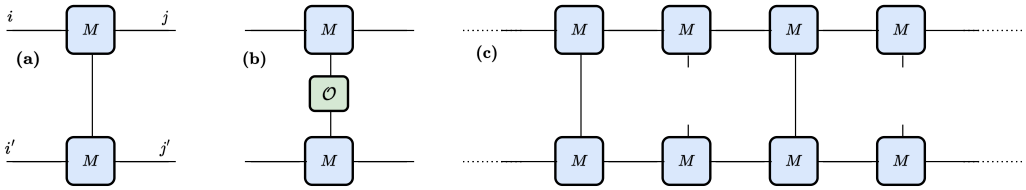

FIGURE 2.5: (a) The transfer matrix $T^I_J = T^{ii'}_{jj'}$, obtained by contracting the bra and ket MPS tensors. (b) The transfer matrix $(T_o)^I_J$ with an operator O sandwiched between the bra and ket MPS tensors. (c) The reduced density operator is obtained by contracting the bra and ket on all sites except the ones where the operators have to be placed.

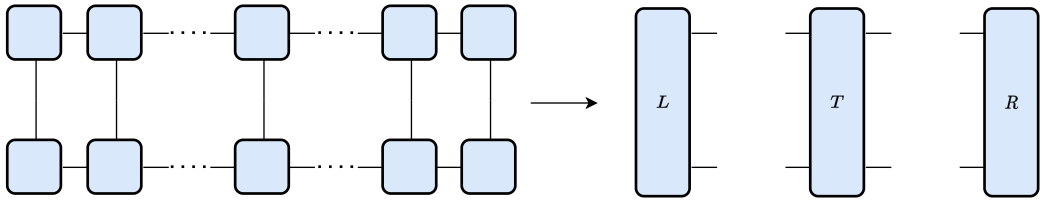

FIGURE 2.6: Reducing the MPS environment into right and left vectors R and L. The MPS is said to be in canonical form if the Hermitian matrices corresponding to L and R are purely diagonal.

Using translational invariance, we get

$$C^o_{x,x+r} = \sum_{\alpha,\beta} t_\alpha^{N-r-1} t_\beta^{r-1} \mathrm{Tr}\left(|\alpha\rangle \langle\alpha| T_o |\beta\rangle \langle\beta| T_o\right) / \sum_\alpha t_\alpha^N. \tag{2.8}$$

In the thermodynamic limit $N \to \infty$ where $\sum_\alpha t_\alpha^N = t_0^N$ and a large separation $r \gg 1$, we get,

$$\begin{aligned} C_{x,x+r} &= \sum_\alpha \left(\frac{t_\alpha}{t_0}\right)^{(r-1)} \langle\alpha| T_o |0\rangle \langle 0| T_o |\alpha\rangle \\ &= |\langle 0| T_o |0\rangle|^2 + |\langle 0| T_o |1\rangle|^2 \left(\frac{t_1}{t_0}\right)^{(r-1)} + \ldots \end{aligned} \tag{2.9}$$

The maximum possible correlation length is obtained from the relation $C(r) = e^{-\frac{|r|}{\xi}}$, i.e., $\xi = (\ln(\frac{t_1}{t_0}))^{-1}$. Hence, the ratio of the leading and the sub-leading eigenvalue will give us information about the maximum correlation length.

2.2 Introduction to Tensor networks

The major problem with MPS formalism is that MPS are well-defined for one-dimensional systems but are not very effective when one applies them to two-dimensional critical states. In order to study two-dimensional systems with MPS, one has to use a 'snake' mapping to map a two-dimensional system to a one-dimensional chain. The problem with this mapping is that two nearest neighbor particles that

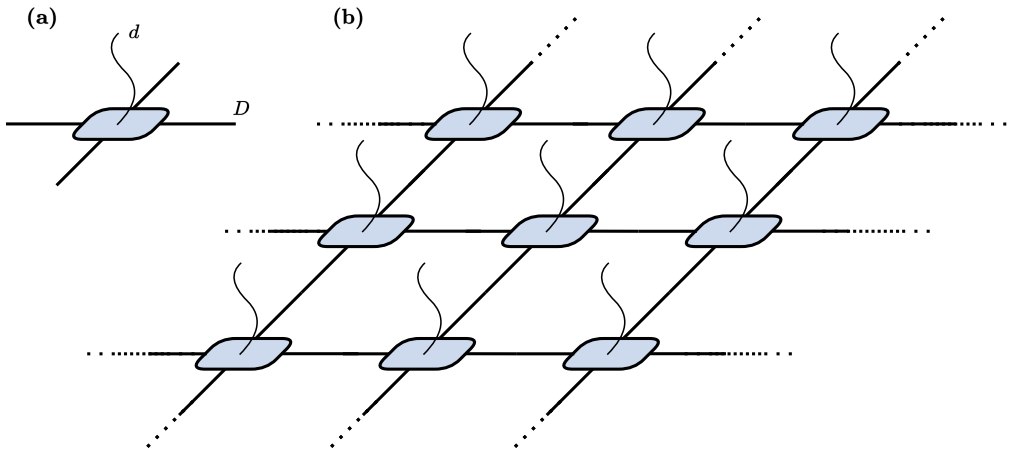

FIGURE 2.7: (a) A typical square lattice PEPS tensor with one physical index shown by a curved line and four virtual indices shown by straight lines. (b) The contraction of several PEPS tensors to give a wavefunction. By using identical tensors on every site, we can incorporate translational symmetry into the wavefunction.

are strongly correlated can be mapped to far away points on the one-dimensional chain. In order to overcome this, we use a different class of tensor networks called the Projected Entangled Pair States (PEPS). We shall now see how the concepts of MPS are extended to PEPS formalism.

2.2.1 Projected Entangled Pair States

The concept of PEPS is a generalization of MPS in two dimensions. A typical PEPS tensor consists of a physical index of dimension d and a set of virtual indices of dimension D [114]. The number of virtual indices is ideally taken to be equal to the coordination number z of the lattice. For a square lattice, we use a rank-5 tensor with four virtual indices and one physical index. Diagrammatically, we prefer to use a curvy line to represent the physical index and distinguish them from the virtual indices that are represented by straight lines. One can construct a given wavefunction from a PEPS tensor by contracting the virtual indices with the virtual indices of the neighboring PEPS tensors, as shown in figure 2.7. A PEPS tensor network obeys the area law by construction [115]. For any given area, the number of open virtual indices that intersect with the boundary grows linearly with the length of the boundary as shown in figure 2.8-(c). Since each open virtual index contains a maximum entanglement of $\ln(D)$, the maximum entanglement between a compact region and the rest of the lattice scales linearly with the length of the boundary. Naturally, the spatial symmetries of the wavefunction are reflected in the spatial symmetries of the PEPS tensor. For the system to be translationally and rotationally invariant, the PEPS tensor should be invariant under the action of the point group symmetry C_{4v}. The basic operations of the C_{4v} point group symmetry are shown diagrammatically in figure 2.8-(a), and the character table is given in table 2.1. For the rest of the thesis, we shall only deal with a translationally invariant C_{4v}-symmetric SU(2) tensors unless otherwise specified.

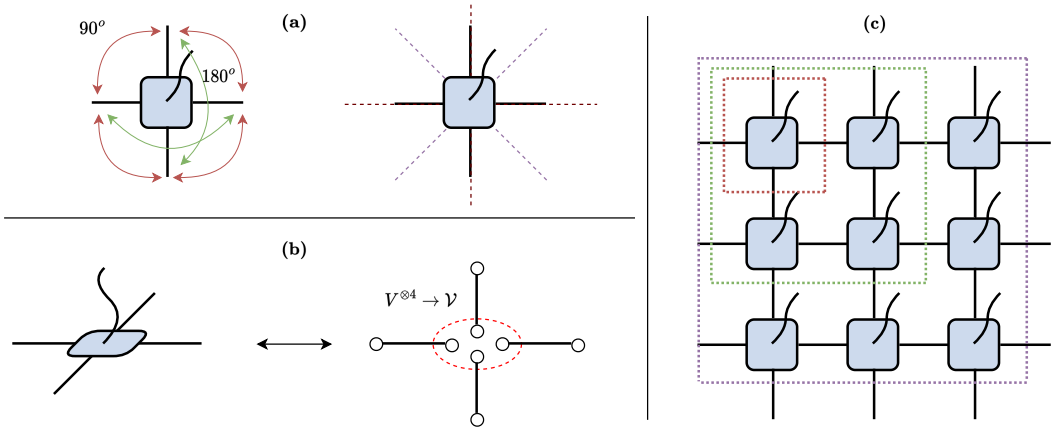

FIGURE 2.8: Basics of PEPS tensor on a square lattice (a) C_{4v} point group symmetry operations. A C_{4v} symmetric PEPS tensor has 90^o rotational symmetry (shown in red) and 180^o rotational symmetry (shown in green) about the center of the tensor. The tensor also has a reflection symmetry about the X-axis, the Y-axis and two XY-axes which are at 45^o angle to X and Y (shown in dotted lines). (b) PEPS tensor as a linear map. (c) Area law of a PEPS tensor network. The maximum entanglement captured by the tensor network is equal to the number of virtual bonds crossing the boundary times the maximum entanglement per bond (given by $\ln(D)$). The number of bonds is proportional to the perimeter of the boundary, hence the area law is always satisfied.

The construction of SU(2) symmetric PEPS is similar to the construction of the AKLT state in 1D [115, 116]. The basic rules of the construction of SU(2) symmetric PEPS are,

- Every SU(2) PEPS tensor can be seen as a linear map from the virtual space $\mathcal{V}^{\otimes 4}$ to the physical space following the SU(2) fusion rules, where the components of the virtual space $\mathcal{V}$ are direct sums of irreducible representations of the SU(2) group.

- Every PEPS tensor has an associated bond matrix that maximally entangles the virtual spaces of neighbouring PEPS tensors by forming SU(2) invariant singlet states.

Additionally, just like 1D-AKLT, we can absorb these bond matrices into the odd sites and create a bipartite lattice of the $A-B$ kind and the resultant tensor B can also be rewritten as the initial tensor $\mathcal{A}$ with a gauge transformation on the physical index as shown in figure 2.9. Later, we shall see how this plays a key role in keeping the bi-layer tensor invariant. We shall now discuss how we can parameterize the PEPS tensor by constructing a basis of SU(2) symmetric linear maps that obey the SU(2) fusion rules.

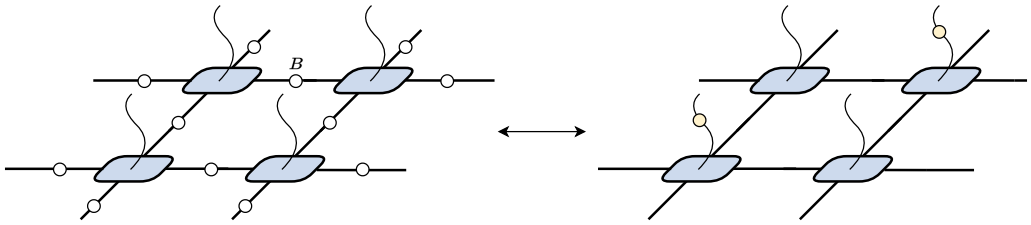

FIGURE 2.9: The absorption of the bond matrices onto the even sites of the tensor network is equivalent to applying a unitary transformation on the physical index of the PEPS tensors of the even sites. This turns the tensor network into an A-B type bipartite lattice.

2.2.2 Construction of SU(2) symmetric PEPS

Let $\mathcal{A}$ be a rank-5 tensor that results in a spin-S wavefunction on a square lattice. Then the dimension of the physical index d is $(2S+1)$. If D is the dimension of the virtual space, then tensor $\mathcal{A}$ can be considered as a linear map from the virtual space to the real space. i.e.

$$\mathcal{A} = A^{s}_{v_1 v_2 v_3 v_4} |s\rangle \langle v_1| \otimes \langle v_2| \otimes \langle v_3| \otimes \langle v_4| \,. \tag{2.10}$$

In order to construct an SU(2) symmetric tensor, the virtual space $\langle v_i|$ should belong to an SU(2) representation $\mathcal{V}$ of dimension D. Further, this virtual representation $\mathcal{V}$ is a direct sum $\mathcal{V} = \bigoplus V_i$ of $\mathcal{N}$ SU(2) irreps V_i such that the total dimension is D, i.e. $D = \sum_i^{\mathcal{N}} (2s_i + 1)$ where s_i is the spin quantum number corresponding to the irrep V_i.

We shall now see how to construct a tensor basis for the tensor $\mathcal{A}$. The $(2S+1)$ components A^s of a tensor $\mathcal{A}$ encode the projectors $P_s : \mathcal{V}^{\otimes 4} \to |s\rangle$ on to the physical state $|s\rangle \equiv |S; S_z = s\rangle$. Hence the problem reduces to finding all possible orthogonal projections from $\mathcal{V}^{\otimes 4}$ to any spin-S Hilbert space that obey the SU(2) fusion rules,

$$\mathcal{A} : |v_1\rangle \otimes |v_2\rangle \otimes |v_3\rangle \otimes |v_4\rangle \to |s\rangle \,, \tag{2.11}$$

and fulfill the orthonormalization property

$$\sum_{s, v_1 v_2 v_3 v_4} A^{s}_{v_1 v_2 v_3 v_4} (B^*)^{s}_{v_1 v_2 v_3 v_4} = \delta_{AB} \tag{2.12}$$

To do this, we have to decompose all possible virtual subspaces $\mathcal{V}^{\otimes 4}$ into disconnected subspaces given by the occupation numbers $n_{\text{occ}} = \{n_1, n_2, \ldots, n_{\mathcal{N}}\}$ of $\mathcal{N}$ spins such that the number of particles is 4, i.e., $\sum_{i=1}^{\mathcal{N}} n_i = 4$. Then we use the S_z quantum number to identify the valid occupation numbers that give us the S_z quantum number of the physical state. For example, for $D = 5$ and $\mathcal{V} = 0 \oplus \frac{1}{2} \oplus \frac{1}{2}$, the possible occupation numbers that result in a spin-$\frac{1}{2}$ physical state are $n_{\text{occ}} = (\{3,1,0\}, \{3,0,1\}, \{1,3,0\}, \{1,0,3\}\{1,1,2\}, \{1,2,1\})$. We the classify the various spin-S wave functions according to their point symmetry,i.e., spherical-symmetry A_1, $d_{x^2-y^2}$ wave B_1, doubly-degenerate p-wave E, g-wave A_2, d_{xy}-wave B_2. To achieve this, we shall construct the following operator that acts on $\mathcal{V}^{\otimes 4}$.

$$O_{\sigma,\sigma_z,\rho,\delta,\mu} = \sigma \mathbf{S}^2 + \sigma_z S_z + \rho R + \delta R_x + \mu D, \tag{2.13}$$

	dim	$2C_4$	C_2	$2\sigma_v$	$2\sigma_d$
A_1	+1	+1	+1	+1	+1
A_2	+1	+1	+1	-1	-1
B_1	+1	-1	+1	+1	-1
B_2	+1	-1	+1	-1	+1
E	+2	0	-2	0	0

TABLE 2.1: Character table for the point group C_{4v}.

where $\mathbf{S}^2$ and S_z are the spin operators. R is the 90^o rotation operator. R_x is the reflection operator and D is the diagonal operator characterizing n_{occ}. The coefficients are chosen such that the eigenstates are easily classifiable based on their corresponding quantum numbers. For the A_1 class, all the operators commute. Since the eigenvectors of the resultant matrix are also eigenvectors of $\mathbf{S}^2$, they commute with the basis generators of SU(2) group. By choosing the eigenvectors corresponding to $S_z = 0$, we can ensure that the resultant vectors are SU(2) symmetric.

Example-1: D=2

We shall now apply the routine described above for $D = 2$ with $\mathcal{V} = \frac{1}{2}$. For more details about the construction of SU(2) symmetric PEPS for spin liquids, refer to Ref. [116].

For $D = 2$ and $\mathcal{V} = \frac{1}{2}$. The size of $\mathcal{V}^{\otimes 4}$ is $2^4 = 16$. Hence each operator in equation 2.13 is a (16×16) Hermitian matrix. The resultant operator $\hat{O}$ in the equation 2.13 is normal and hence diagonalizable. We then assign the values of the coefficients $(\sigma, \sigma_z, \rho, \delta, \mu) = (10^6, 10^4, 10^2, 1, 0)$. Note that since there is only one species of virtual spin, in this case, the occupation number is always $n_{\text{occ}} = 4$, so we put $\mu = 0$. The other coefficients differ by at least two orders of magnitude.

If we diagonalize the resultant operator, the resultant eigenvalues (in decreasing order of magnitude of the absolute value) are: 6020101, 6010101, 6000101, 5990101, 5980101, 2010000, 2010000 + 100i, 2010000 - 100i, 2009900, 2000000 - 100i, 2000000 + 100i, 1999901,1990000 + 100i, 1990000 - 100i, 1989901, -101, 101

One straightforward observation is that the eigenvalues can be directly classified into three groups based on how close the absolute value is to $6 * 10^6, 2 * 10^6$, or 0. Since we have assigned the highest coefficient (10^6) to the $\mathbf{S}^2$ operator, we deduce that the three groups correspond to the expectation values $6, 2$ and 0 of one quintuplet $(S = 2)$, three triplets $(S = 1)$ and two singlets $(S = 0)$ respectively. This is expected because the fusion of the four virtual spin-$\frac{1}{2}$ particles would lead to, $(\frac{1}{2} \otimes \frac{1}{2} \otimes \frac{1}{2} \otimes \frac{1}{2}) = (0 \oplus 1) \otimes (0 \oplus 1) = (2) \oplus 3(1) + 2(0)$. The state with $(S = 2)$ and A_1 spherical symmetry is the AKLT state described above. In each group, we observe the change in the next orders of magnitude to identify the quantum numbers of S_z, R, and R_x. We also notice that the triplets have states with complex-valued eigenvalues which correspond to the operators R and R_x, implying the presence of states with E symmetry. The table 2.1 summarizes the character table of the point group C_{4v}.

$S_z = +1/2$	$S_z = -1/2$
$T_{\frac{1}{2}}(2,0,0,0) = \frac{1}{2}$	$T_{-\frac{1}{2}}(1,0,0,0) = \frac{1}{2}$
$T_{\frac{1}{2}}(0,2,0,0) = \frac{1}{2}$	$T_{-\frac{1}{2}}(0,1,0,0) = \frac{1}{2}$
$T_{\frac{1}{2}}(0,0,2,0) = \frac{1}{2}$	$T_{-\frac{1}{2}}(0,0,1,0) = \frac{1}{2}$
$T_{\frac{1}{2}}(0,0,0,2) = \frac{1}{2}$	$T_{-\frac{1}{2}}(0,0,0,1) = \frac{1}{2}$
$T_{\frac{1}{2}}(1,1,2,0) = -\frac{1}{2\sqrt{6}}$	$T_{-\frac{1}{2}}(1,2,2,0) = \frac{1}{2\sqrt{6}}$
$T_{\frac{1}{2}}(1,1,0,2) = -\frac{1}{2\sqrt{6}}$	$T_{-\frac{1}{2}}(1,2,0,2) = -\frac{1}{\sqrt{6}}$
$T_{\frac{1}{2}}(1,2,1,0) = \frac{1}{\sqrt{6}}$	$T_{-\frac{1}{2}}(1,0,2,2) = \frac{1}{2\sqrt{6}}$
$T_{\frac{1}{2}}(1,2,0,1) = -\frac{1}{2\sqrt{6}}$	$T_{-\frac{1}{2}}(2,1,2,0) = -\frac{1}{\sqrt{6}}$
$T_{\frac{1}{2}}(1,0,1,2) = \frac{1}{\sqrt{6}}$	$T_{-\frac{1}{2}}(2,1,0,2) = \frac{1}{2\sqrt{6}}$
$T_{\frac{1}{2}}(1,0,2,1) = -\frac{1}{2\sqrt{6}}$	$T_{-\frac{1}{2}}(2,2,1,0) = \frac{1}{2\sqrt{6}}$
$T_{\frac{1}{2}}(1,1,0,2) = -\frac{1}{2\sqrt{6}}$	$T_{-\frac{1}{2}}(1,2,0,2) = \frac{1}{2\sqrt{6}}$
$T_{\frac{1}{2}}(2,0,1,1) = \frac{1}{\sqrt{6}}$	$T_{-\frac{1}{2}}(2,0,1,2) = \frac{1}{2\sqrt{6}}$
$T_{\frac{1}{2}}(0,1,1,2) = -\frac{1}{2\sqrt{6}}$	$T_{-\frac{1}{2}}(2,0,2,1) = -\frac{1}{\sqrt{6}}$
$T_{\frac{1}{2}}(0,1,2,1) = -\frac{1}{2\sqrt{6}}$	$T_{-\frac{1}{2}}(0,1,2,2) = \frac{1}{2\sqrt{6}}$
$T_{\frac{1}{2}}(0,1,2,1) = \frac{1}{\sqrt{6}}$	$T_{-\frac{1}{2}}(0,2,1,2) = -\frac{1}{\sqrt{6}}$
$T_{\frac{1}{2}}(0,2,1,1) = -\frac{1}{2\sqrt{6}}$	$T_{-\frac{1}{2}}(0,2,2,1) = \frac{1}{2\sqrt{6}}$

TABLE 2.2: Tensor entries of the SU(2) basis tensors $A_1^{(1)}$ and $A_1^{(2)}$ for $D = 3$ and $\mathcal{V} = 0 \oplus \frac{1}{2}$.

The top row of the table consists of the symmetry actions. The first column contains the classification of states. The entries of the table represent the expectation value of the state w.r.t the symmetry action. One can use this to identify the eigenvalue corresponding to a particular state.

Example-2: D=3

For $D = 3$, the virtual space is $\mathcal{V} = 0 \oplus \frac{1}{2}$. The size of $\mathcal{V}^{\otimes 4}$ is $3^4 = 81$. Hence each operator in equation2.13 is a (81×81) non-Hermitian matrix. The coefficients are taken as $(\sigma, \sigma_z, \rho, \delta, \mu) = (10^8, 10^6, 10^4, 10^2, 1)$. Upon diagonalizing and identifying the tensors corresponding to $S = \frac{1}{2}$, we notice that n_{occ} can only take $\{3,1\}$ and $\{1,3\}$ and that each occupation number has only one independent orthogonal tensor. We label them by $A_1^{(1)}$ and $A_1^{(2)}$ respectively. Using these, we can construct any SU(2) symmetric PEPS tensor with D=3 by,

$$A = \lambda_1 A_1^{(1)} + \lambda_2 A_1^{(2)}. \tag{2.14}$$

The corresponding tensors are given in table 2.2

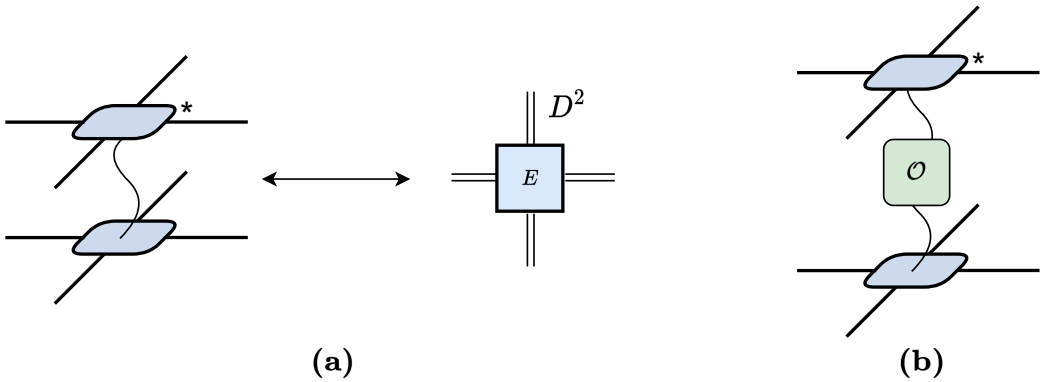

FIGURE 2.10: (a) The bi-layer tensor obtained by contracting the physical indices of the bra and ket tensors. (b) Bi-layer tensor with one-site operator sandwiched between the two tensors.

2.3 Infinite Projected Entangled Pair States

Once we have defined a way to construct any PEPS with a given bond dimension and virtual spaces, how do we study the properties of the state that it represents? From its local observables to entanglement properties, one cannot simply use the wavefunction itself as contracting all the virtual indices because the resultant tensor would have a growing exponential Hilbert space. In order to solve this, we shall use the reduced density matrix, where we shall trace over all the "idle" physical degrees of freedom. This can be done by constructing a bi-layer tensor E as shown in figure 2.10. This bi-layer tensor is the two-dimensional equivalent of the transfer matrix operator for MPS. As we have noted earlier, every SU(2) symmetric PEPS tensor will result in a bipartite lattice. However, since the tensors at the odd and the even sites in such a bipartite lattice differ by rotation on a physical basis, the bi-layer tensor of both the sub-lattices is identical. This makes the reduced density matrix truly translationally invariant. We shall now exploit this translational invariance to capture the power of tensor networks.

2.3.1 Corner Transfer Matrix Renormalization Group

Contracting the PEPS tensors for a large number of bodies is computationally expensive. In the thermodynamic limit, we have to perform an infinite number of tensor contractions to compute the exact wave function, which is practically not possible. Hence, we have to use an approximation scheme. We start by asking a basic question, how can we extend the transfer matrix formalism to two dimensions? How are the right and left environment vectors, shown in figure 2.6, generalized to two dimensions? The major advantage of MPS formalism is that boundary vectors and the transfer matrix are always fixed in size. Unfortunately, the same is not true for PEPS. The boundary vector generalizes to a matrix called the corner matrix, and the transfer matrix generalizes to a rank-3 tensor called the edge tensor[1]. They are described using the Corner transfer matrix (CTM) description. In this section, we shall discuss

[1]The actual transfer matrix is obtained by contracting two edge tensors. The left and right boundaries of such a transfer matrix are given by two corners

the *Corner Transfer Matrix Renormalization Group* (CTMRG) scheme introduced by Nishino and Okunishi [117] and developed by Orús and Vidal [118].

In the CTM description, we divide the translationally invariant bi-layer contraction into 8 sections, as shown figure 2.11-(a). The principal idea of CTMRG is to replace the contracted tensors in each of these regions with a boundary tensor such that when all the tensors are contracted, we get the exact environment. Since the individual PEPS tensor has a C_{4v} symmetry, it is natural to assume that the boundary tensors C and T have spatial symmetries that reflect the same. For a finite-size tensor, the contraction can be exact with each of the boundaries containing the exact contraction of the local tensors of the region. However, we notice that as the number of sites increases, the size of the boundaries increases exponentially. The aim of CTMRG is to approximate the boundaries C and T to a matrix of size $\chi \times \chi$ and a rank-3 tensor of size $\chi \times D^2 \times \chi$ such that the resultant contraction is as close to the infinite-size environment as possible. The accuracy of the environment can be controlled by varying the value of χ. In order to get the most reliable environment that captures the long-range correlations, we have to use the real-space numerical renormalization group scheme. One of the most interesting and important results in Nishino's work is that the reduced density matrix formed by contracting four corners C^4, as shown in figure 2.11-(b) can play the role of the density matrix in DMRG. Hence one can diagonalize it to identify the most relevant subspace. A typical CTMRG step consists of absorbing a single bi-layer tensor to enlarge the corner and edge tensors and then renormalizing them back to a smaller size by applying appropriate isometries as shown in figure 2.11-(c). This process is repeated multiple times till the spectrum of the corner converges to a fixed set of values. How we calculate these isometries depends on the nature of the corner and the symmetries of the tensor. Section 3.3 contains the details of the CTMRG for real-symmetric and complex-symmetric corners.

2.3.2 Reduced density matrix and Observables

Once we obtain an approximation of the corner matrix and the edge tensor, we can use them to form the environment of the reduced density matrices of a particular region. The environment of a region with $(n \times m)$ sites is constructed such that each site on the perimeter of the region is connected to an edge tensor T. The Edge tensors at the corner of the region are connected by the corner matrix. Figure 2.12-(a) shows the CTM environment of a region with (3×2) sites. Once we define the environment, translational invariance ensures that the environment of every site is identical. In order to compute the expectation value, we place the bi-layer tensors with the operator sandwiched into the environment. Once we trace all the virtual indices, we get the $\langle O \rangle$. We then divide it with the norm of the wavefunction, computed by tracing the elementary bi-layer tensors E with the environment. Hence, the expectation value of an observable per site is equal to the average of the expectation values obtained in that region. As explained before, the dimension of χ controls the approximation of the environment. As $\chi \to \infty$, the expectation value approaches the exact value. Thus, in order to calculate an expectation value, we compute it using CTMRG for various χ and then extrapolate the value at infinity.

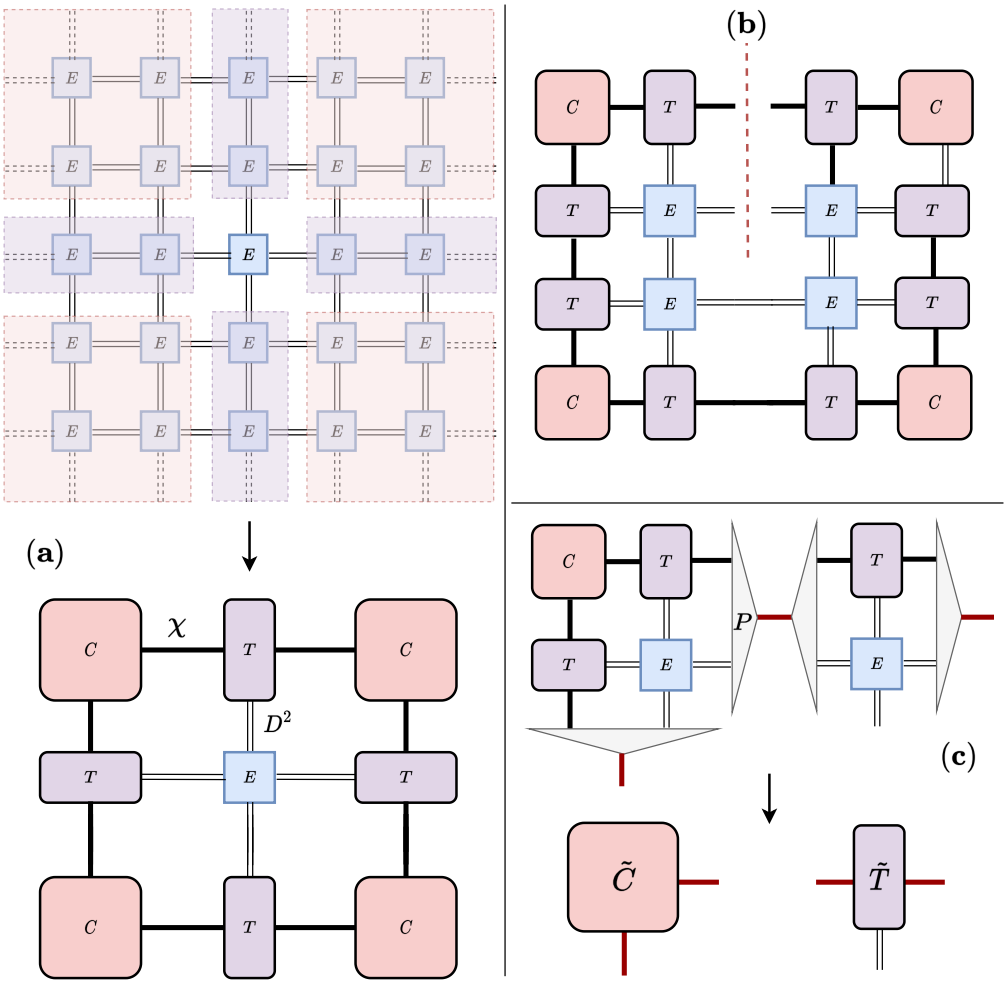

FIGURE 2.11: (a) In the corner transfer matrix formalism, the contraction of the reduced density matrix of the iPEPS wavefunction is replaced by four corner matrices C of dimension $(\chi \times \chi)$ and four edge tensors T of dimensions $(D^2 \times \chi \times \chi)$. The C_{4v} symmetry and translational invariance of the wavefunction result in all the identical corner matrices that are complex-symmetric. Similarly, the edge tensors T are identical and have a reflection symmetry about the axis passing through the leg of dimension D^2. (b) The reduced density matrix that has to be approximated. (c) Renormalization step that reduces the bond dimension of the corner from $(\chi D^2 \times \chi D^2)$ to $\chi \times \chi$ and the edge tensor T from $(D^2 \times \chi D^2 \times \chi D^2)$ to $(D^2 \times \chi \times \chi)$.

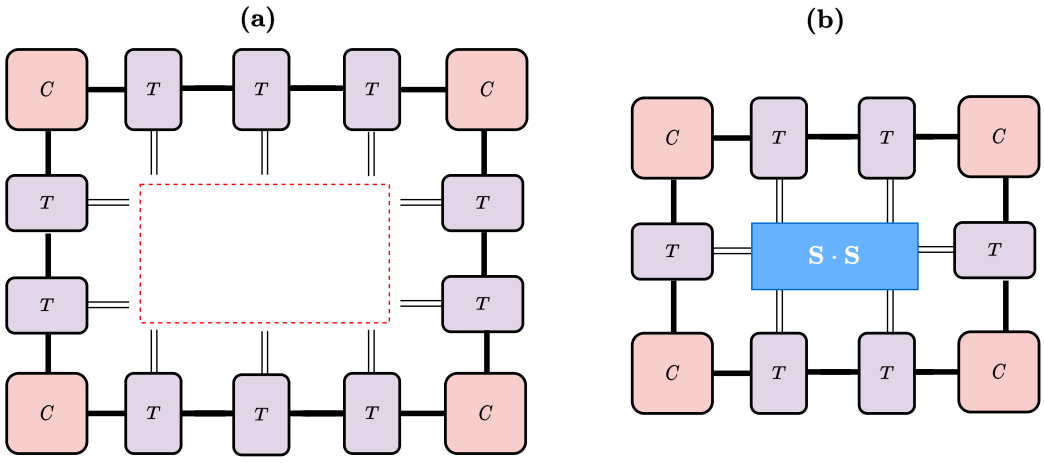

FIGURE 2.12: (a) Environment of a 3×2 unit cell computed from CTMRG. (b) Expectation value of two-site correlator $\langle \mathbf{S} \cdot \mathbf{S} \rangle$. Note that in order to get the actual value, we should divide it with the norm of the environment, which is obtained by replacing the bi-layers corresponding to $\mathbf{S} \cdot \mathbf{S}$ with elementary bi-layer tensors E.

Chapter 3

Tensor network algorithms for time evolution

In this chapter, we shall explain the methods and algorithms used to perform the time evolution of PEPS. It starts with Suzuki-Trotter decomposition and how it can be used to reduce the time evolution operator into a simple local PEPO. We then explain the simple update procedure along with a form of matrix decomposition called the Autonne-Takagi decomposition. Before moving to the variational optimization procedure, we explain the details of the CTMRG algorithm used to obtain the environment.

3.1 Time Evolution Operator

3.1.1 Basics

The general time evolution of a quantum state $|\psi_0\rangle$ under a Hamiltonian $\mathcal{H}$ is given by solving the time-dependent schrödinger equation.

$$\begin{aligned} \mathcal{H}|\psi(t)\rangle &= i\frac{d\,|\psi(t)\rangle}{dt} \\ \Rightarrow |\psi(t)\rangle &= e^{-i\int_0^t \mathcal{H}dt}|\psi_0\rangle \end{aligned} \tag{3.1}$$

For a time-independent Hamiltonian one can get the time evolution by applying the time evolution gate $U(t) = e^{-i\mathcal{H}t}$.

However, this gate suffers from the same problem as the wavefunction on which it acts, i.e., the Hilbert space grows exponentially with system size. This makes finding the exponential of the Hamiltonian computationally expensive. In this section, we shall see various ways to approximate this time evolution operator to a local tensor operator that acts on a local tensor.

3.1.2 Suzuki-Trotter decomposition

Consider a Hamiltonian that can be written as a sum of local terms that act on small and finite Hilbert space whose exponentials are easy to compute. If the local terms compute, then the exponential of the Hamiltonian is easy as The Suzuki–Trotter expansion is a way of approximately expressing the exponential of a large matrix as a product of exponentials of component matrices. This is particularly useful if we can write the matrix as a sum of components whose exponentials are easier to compute since the exponential sum of commuting matrices is the same as the product of exponentials of the said commuting matrices. If two matrices A and B commute, then,

$$e^{A+B} = e^A e^B = e^B e^A. \tag{3.2}$$

However, this form of factorization is not valid if the matrices A and B do not commute. Suzuki-Trotter factorization is a way of approximately factorizing the exponential of a large matrix [119, 120]. The simplest Suzuki-Trotter decomposition can be described as,

$$e^{\epsilon(A+B)} = e^{\epsilon A} e^{\epsilon B} + O(\epsilon^2), \tag{3.3}$$

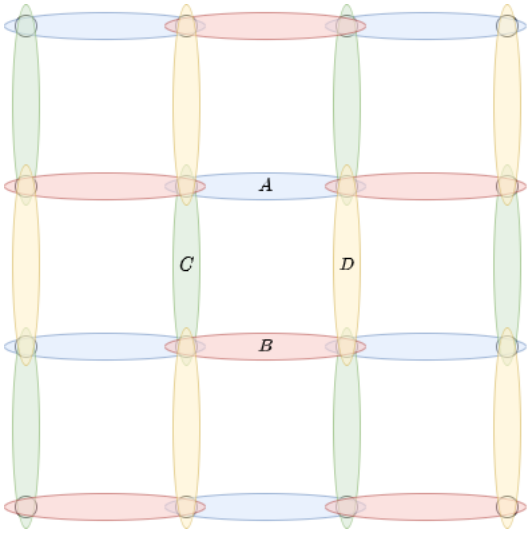

FIGURE 3.1: The Hamiltonian two-site terms are divided into four groups, A, B, C, D. The groups are shown in colors blue, red, green and yellow respectively.

where A and B are non-commuting matrices and ϵ is a parameter. If we can break our Hamiltonian H as sum of non-commuting operators i.e., $H = \sum_{k=1}^{n} h_k$, the 1st order Suzuki-trotter decomposition is defined as,

$$e^{itH} = e^{it(\sum_k h_k)} = \prod_k e^{ith_k} + O(t^2). \tag{3.4}$$

The first term of the R.H.S. acts as the approximation and the second term gives us an estimate of the error. Similarly, the second-order Suzuki-Trotter decomposition is defined as,

$$e^{(\sum_k h_k)it} = \prod_{k=1}^{n} e^{ih_k t} \prod_{k=1}^{n} e^{ih_{n-k+1}t} + O(t^3). \tag{3.5}$$

One can easily verify the above two decompositions by expanding the Taylor series of the exponentials. Note that the decomposition is not unique as there are multiple ways of writing a matrix as a sum of its components. Though, all such decompositions are equally identical up to an error that scales as $O(t^2)$ for the first order (and $O(t^3)$ for the second order decomposition).

3.1.3 Suzuki-Trotter decomposition of 2D spin systems

In this section, we shall apply the above-explained Suzuki-Trotter decomposition of the time evolution operator of the Heisenberg Hamiltonian on a square lattice.

$$\mathcal{H} = J \sum_{\langle i,j \rangle} \mathbf{S}_i \cdot \mathbf{S}_j.$$

For this Hamiltonian, one can group all the two-site interactions into four non-commuting groups [121] A, B, C and D as shown in figure 3.1.

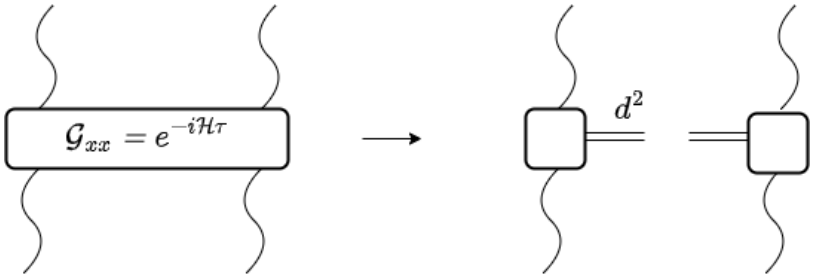

FIGURE 3.2: Using Autonne-Takagi decomposition, we can break the Gate into a symmetric PEPO. Notice that the virtual index has a size of d^2. This tells us that the resultant enlarged bond of the PEPS tensor is at most d^2D.

Since each group comprises of local two-site Hamiltonian terms that compute, the exponential of the entire group is equal to the product of exponentials of the individual two-site terms.

Putting these interaction terms in equation 3.5, we get,

$$\begin{aligned} U(t) &= e^{-i\mathcal{H}_a t} e^{-i\mathcal{H}_b t} e^{-i\mathcal{H}_c t} e^{-i\mathcal{H}_d t} + O(t^2) \\ &= \mathcal{G}_a(t)\mathcal{G}_b(t)\mathcal{G}_c(t)\mathcal{G}_d(t) + O(t^2) \\ &= U_I(t) + O(t^2) \end{aligned} \tag{3.6}$$

From here on, let $e^{-i\mathcal{H}_k t}$ be called by the gate $\mathcal{G}_k(t)$ and $U_I(t)$ be their product as shown in the equation 3.6. In order to minimize the error, we perform the time evolution in small steps. Let $\tau = \frac{t}{n}$. Then $e^{-i\mathcal{H}t} = (e^{-i\mathcal{H}t/n})^n$. Using this, we get

$$\begin{aligned} U(t) &= U(\tau)^n \\ &= (\mathcal{G}_a(\tau)\mathcal{G}_b(\tau)\mathcal{G}_c(\tau)\mathcal{G}_d(\tau) + O(\tau^2))^n \\ &= (\mathcal{G}_a(\tau)\mathcal{G}_b(\tau)\mathcal{G}_c(\tau)\mathcal{G}_d(\tau))^n + O(\tau) \\ &= U_I(\tau)^n + O(\tau) \end{aligned} \tag{3.7}$$

In order to minimize the error, the time-step τ should be as small as possible. Thus, we can reduce the time evolution operator into a simple set of two-site operations. One can also use an SVD decomposition (or Autonne-Takagi decomposition as discussed in section 3.2.1) to convert them into a one-site PEPO, as shown in figure 3.2. We shall now expand the L.H.S. and R.H.S. of the equation 3.7 to understand how the local two-site operators collectively give rise to terms that act upon multiple sites.

On expanding the L.H.S., we get,

$$\begin{aligned} e^{it\sum_k h_k} &= \mathcal{I} + it\sum_k h_k - \frac{1}{2!}t^2(\sum_k h_k)^2 + \ldots \\ &= \mathcal{I} + \sum_{m>0} \frac{1}{m!}(it)^m (\sum_k h_k)^m \end{aligned} \tag{3.8}$$

Similarly, by expanding the R.H.S., we get

$$\begin{aligned}
(\prod_k e^{ith_k})^n &= (\mathcal{I} + i\tau \sum_k h_k + O(\tau^2))^n \\
&= \mathcal{I} + n(i\tau) \sum_k h_k - \frac{n(n-1)}{2}(i\tau)^2(\sum_k h_k)^2 + ... \\
&= \mathcal{I} + \sum_m \frac{n(n-1)(n-2)...(n-(m-1))}{m!}(i\frac{t}{n})^m(\sum_k h_k)^m \\
&= \mathcal{I} + \sum_m \frac{(1-\frac{1}{n})(1-\frac{2}{n})...(1-\frac{m-1}{n})}{m!}(it)^m(\sum_k h_k)^m \\
&= \mathcal{I} + \sum_m C_m \frac{1}{m!}(it)^m(\sum_k h_k)^m \qquad (3.9)
\end{aligned}$$

where

$$C_m = (1-\frac{1}{n})(1-\frac{2}{n})...(1-\frac{m-1}{n}),$$

which deviates from 1 as $\frac{m^2}{2n}$. For large n, and for $m \ll n$, the value C_m is close to one. Hence, as the number of steps n increases, the Suzuki-Trotter decomposition covers more terms in equation 3.8, resulting in a more accurate representation of the operator.

Restoring C_{4v} symmetry

We observe in equation 3.6 that L.H.S. $U(\tau) = e^{-i\mathcal{H}\tau}$ is invariant under the action of elements of the point group C_{4v} as the Hamiltonian $\mathcal{H}$ itself is invariant under the action of C_{4v}. However, the same cannot be said about the R.H.S. as the terms $\mathcal{H}_k$ do not commute. We get a different approximation if we change the order in which we apply the gates. In the course of this thesis, we encounter conditions where it is necessary for the resultant tensor to have C_{4v} symmetry. For this, consider all the possible orders in which we can apply the four gates. We now use the fact that any linear combination of two distinct Suzuki-trotter decompositions is also a valid decomposition if the coefficients add up to one, i.e. if $\tilde{U}_1(\tau)$ and $\tilde{U}_2(\tau)$ are two different Suzuki-trotter decompositions, then

$$U(\tau) = \alpha U(\tau) + (1-\alpha)U(\tau) = \alpha\tilde{U}_1(\tau) + (1-\alpha)\tilde{U}_2(\tau) \qquad (3.10)$$

Hence, we can restore the C_{4v} symmetry by taking the average of all the permutations of the order in which the gates can be applied. Note that the act of taking the average of the tensor is meaningful only if the virtual space of the tensors are in the same canonical form. It is crucial to fix the virtual space of the tensors before performing the time evolution.

Note that since the gates $\mathcal{G}_k$ are Unitary, the Suzuki-Trotter approximations are unitary too. However, once we take the average, the resultant approximation is only approximately unitary, with the deviation scaling as τ^2. Hence, one will have to decide if the approximation has to be C_{4v} or unitary. For small enough τ, the deviation would be small enough not to affect the results.

3.2 Simple Update

Once we reduce the global time evolution operator to a single-site PEPO, we can apply it to the physical space of the tensor to update it. Since each Trotter-step PEPO operator increases the virtual bond dimension by a factor of d^2, the bond dimension of the tensor is expected to grow exponentially with the number of Trotter steps. Thus, an approximation scheme is necessary to control the bond dimension after every step since $U(\tau) = \mathcal{G}_a\mathcal{G}_b\mathcal{G}_c\mathcal{G}_d$, each step of the update can be divided into four substeps where the approximation is made after applying the individual gate $\mathcal{G}_k$.

An approximation scheme after application of a gate $\mathcal{G}_k$ to a wave $|\psi\rangle$ is a procedure of finding a wavefunction $|\phi\rangle$ such that minimizes the distance $\||\phi\rangle - \mathcal{G}_k|\psi\rangle\|$. The difference between various approximation schemes depends on the way in which the distance is calculated.

The simplest of such approximations is the simple update scheme where the distance is minimized at a local tensor level. Considering that the wavefunction is parameterized by the local PEPS tensor, the simple update reduces the problem of updating the wavefunction to updating the local PEPS tensor. The simple update scheme was first introduced by Jiang [122] and has been widely used [123–125] ever since. In each step of the simple update, we apply the gate $\mathcal{G}_k$ that acts on two sites, obtain a two-site tensor, and then truncate the enlarged bond using singular value decomposition. Since we are only concerned with C_{4v} symmetric translationally invariant tensor networks, the SVD has to be symmetric. Before we discuss the details of the simple update scheme, we shall first discuss the details of the symmetric form of singular value decomposition called the Autonne-Takagi decomposition used in this work.

3.2.1 Autonne-Takagi decomposition

The Autonne-Takagi decomposition is a way to factorize a symmetric matrix into a product of two matrices that are transposed of each other [126]. For a complex symmetric matrix A, it is defined as follows:

$$A = USU^T, \tag{3.11}$$

where S is a diagonal matrix containing the singular values of the matrix A and U is a complex unitary. In order to find the right unitary U, we follow the procedure described in ref. [127].
For any complex matrix, we define the singular value decomposition as

$$A = USV^\dagger,$$

where S is the diagonal with singular values and U and V are unitary matrices with corresponding singular vectors and † denotes Hermitian conjugate.

We define a matrix $Z = U^\dagger V^*$ where V^* denotes the complex conjugate of V. Since A is complex symmetric, we can rewrite the SVD as,

$$USV^\dagger = A = A^T = V^*SU^T.$$

$$\Rightarrow \quad SV^{\dagger}U^{*} = U^{\dagger}V^{*}S \Rightarrow \quad ZS = SZ^{T} \tag{3.12}$$

$$\Rightarrow \quad ZSZ^{*} = S. \tag{3.13}$$

Since the above equation preserves the spectrum of S, it is a similarity transformation. Hence, Z and Z^{*} should be the multiplicative inverse of each other. i.e. $Z^{\dagger} = Z^{*} \Rightarrow Z = Z^{T}$. This implies that Z and S commute with each other.

$$\begin{aligned} ZS &= SZ \\ \Rightarrow \quad (z_{ij}S_{jj} - S_{ii}z_{ij}) &= 0 \\ \Rightarrow \quad z_{ij}(s_i - s_j) &= 0 \\ \Rightarrow \quad z_{ij} &= 0 \quad \forall s_i \neq s_j. \end{aligned} \tag{3.14}$$

Hence, we note that any such matrix Z that commutes with a diagonal matrix S should be diagonal if all the entries in S are distinct. If S has repeated singular values, Z has a block diagonal structure with the size of the blocks equal to the degeneracy of the singular values, i.e., $Z = \bigoplus_k B_{n_k \times n_k}$ where n_k is the multiplicity of the k-th distinct singular value and $B_{n_k \times n_k}$ is the corresponding block diagonal part of Z. Similarly, we can rewrite $S = \bigoplus_k s_k \cdot \mathbb{I}_{n_k \times n_k}$. Since every block $B_{n_k \times n_k}$ commutes with the identity matrix, the overall matrix to commutes with the diagonal matrix S. Since a power of Z can also be written in the block diagonal form, they too commute with the diagonal matrix D. Hence we can write, $Z^{\frac{1}{2}}S = SZ^{\frac{1}{2}}$. If the matrix equation 3.12 to $n = \frac{1}{2}$. Hence we get,

$$A = USV^{\dagger} = USV^{\dagger}U^{*}U^{T} = USZ^{T}U^{T} = U(Z^{\frac{1}{2}})^{T}S(Z^{\frac{1}{2}})^{T}U^{T} = U_Z S U_Z^{T}. \tag{3.15}$$

Hence we get $A = U_Z S U_Z^{T}$. Where $U_Z = U(Z^{\frac{1}{2}})^{T}$.
Note that the resultant unitary U_Z is not unique since the singular matrices U and V themselves are not unique. Let two such unitaries U_{Z_1} and U_{Z_2} be related by $U_{Z_1} = U_{Z_2}\phi$, where ϕ is a unitary matrix, then

$$A = U_{Z_1}S(U_{Z_1})^{T} = U_{Z_2}(\phi S \phi^{T})(U_{Z_2})^{T} = U_{Z_2}S(U_{Z_2})^{T}, \tag{3.16}$$

i.e. $(\phi S \phi^{T}) = S$. Since this transformation preserves the spectrum of S, it has to be a similarity transformation, i.e., $\phi\phi^{T} = I$. This also implies that the matrix ϕ has to commute with S. Hence, if the singular values S are all distinct, the matrix ϕ is an orthogonal diagonal matrix i.e., it's a diagonal matrix with only ± 1 as its diagonal entries. If S has multiplicities, the matrix ϕ can take a block diagonal structure with $n_k \times n_k$ orthogonal blocks where n_k is the multiplicity of the corresponding singular value S_k.

By using the Autonne-Takagi decomposition, we can factorize a symmetric matrix as,

$$A_{n \times n} = USU^{T} = U\sqrt{S}\sqrt{S^{T}}U^{T} = (U\sqrt{S})(U\sqrt{S})^{T} = MM^{T}. \tag{3.17}$$

Now, if we have to approximate A as a factorization, we can find the approximate M by keeping the k largest singular values in S.

3.2.2 SU algorithm

We shall now go through the SU algorithm for a two-site nearest-neighbor Hamiltonian.

For the simple nearest-neighbor antiferromagnetic Heisenberg Hamiltonian, the Trotter step is defined as applying the four gates as defined in equation 3.6. Applying two-site tensor results in a rank-8 tensor as shown in figure 3.3-(c), which can be reshaped into a matrix of dimensions $dD^3 \times dD^3$. The resultant simple update matrix's low-rank approximation can be found by doing a singular value decomposition. In order to reduce the computational cost, we can separate the active bond to which the gate $\mathcal{G}_k$ is applied, as shown in figure 3.3. Then, the simple update matrix is reduced to a matrix of dimension $dD \times dD$. If the initial one-site tensor is C_{4v} symmetric and the two-site gate $\mathcal{G}_k$ is symmetric, we can use Autonne-Takagi decomposition. The procedure is then repeated on all four bonds to complete the simple update step. Thus simple update scheme can be summarized in figure 3.3 and contains the following steps:

1. The tensors at a site and its neighbor are first split by singular value decomposition (SVD) to isolate the active bond on which the complex symmetric gate $\mathcal{G}_k$ is applied.

2. The resulting two-site symmetric complex SU-matrix is factorized using Autonne-Takagi decomposition. The D_{cut} largest singular values are retained, and the rest are discarded to reduce the dimension of the bond.

3. The updated components are used to construct the new tensor.

4. The procedure is repeated on the remaining bonds

5. Once all the bonds are updated, the tensor is symmetrized and projected back into the SU(2) manifold to get the relevant coefficients.

In order to determine the relevant virtual space of the resultant tensor so that we can choose the appropriate set of tensors to project into, we can simple look at the multiplicities of the singular values obtained in step-2. The presence of a spin-s particle in the virtual bond gives rise to a multiplet of degeneracy $(2s + 1)$. While truncating the bond, care has to be taken not to cut through the multiplicities as it would result in the breaking of SU(2) symmetry.

The last step in the simple update scheme introduces a new set of challenges. The Autonne-Takagi decomposition is not unique, as there are multiple unitaries U that give rise to a valid symmetric SVD. In particular, for any symmetric matrix decomposition $A = MM^T$, one can get a gauge matrix g that is complex-orthogonal such that,

$$A = Mgg^T M^T = (Mg)(Mg)^T.$$

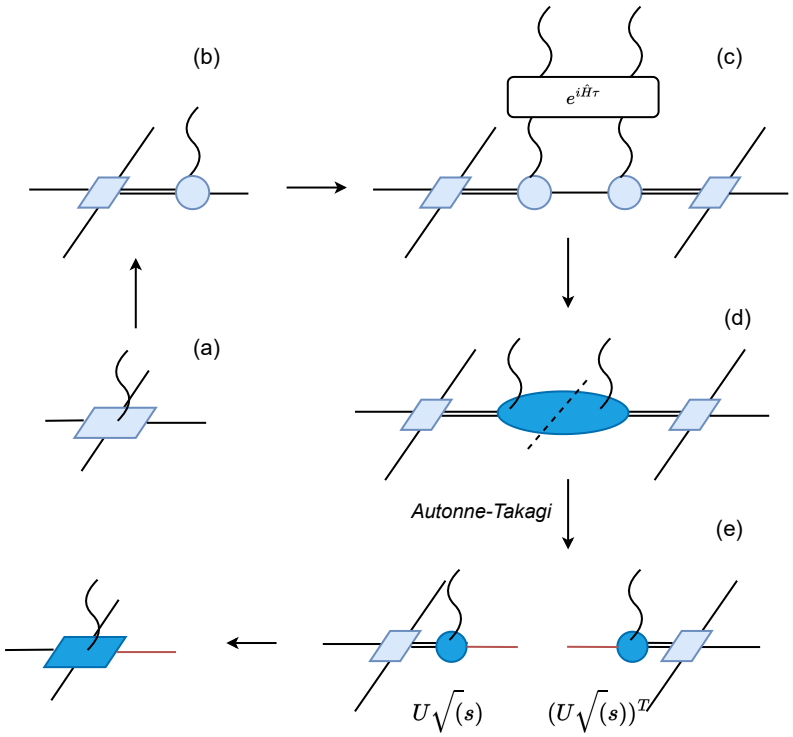

FIGURE 3.3: The basic idea of a simple update. By applying the two-site gate, we get an enlarged tensor that can be split into two symmetric halves using Autonne-Takagi decomposition. In practice, we shall separate the bond and perform the 'gauge fixing process'.

Since this gauge matrix is arbitrary and cannot be fixed, each step of the simple update procedure might introduce a different gauge matrix on different bonds and result in a change of basis. Without correcting this gauge freedom, we cannot symmetrize the tensor or project it into the relevant SU(2) subspace. We shall now discuss how this is done.

3.2.3 Gauge fixing

The singular values of the SVD give us a picture of the virtual subspace. The presence of a spin-s particle in the virtual bond gives rise to a multiplet of degeneracy $(2s+1)$. For example, under the NN AF Heisenberg Hamiltonian, the NN RVB state results in multiplets of degeneracy 1,2,3, which imply the virtual space correspond to $\mathcal{V} = 0 \oplus \frac{1}{2} \oplus 1$ whereas the non-U(1) invariant RVB state has a multiplet structure of $\mathcal{V} = 0 \oplus \frac{1}{2} \oplus 1 \oplus \frac{3}{2}$.

In order to identify the gauge matrix, we trace back our steps from the final result. Once the gauge freedom is eliminated, the virtual bonds are all moved into the same virtual space. This tensor has the least C_{4v} asymmetry among all the tensors connected by the gauge matrices. We shall thus try to identify the gauge to minimize this asymmetry. First, note that the gauge arises from the fact that there can be multiple valid unitaries for a given Autonne-Takagi decomposition. Let's say we fix the order of the singular values in two different decompositions and get two different unitaries U and V. Let $\Phi = U^\dagger V$

$$USU^T = VSV^T \implies S\Phi^T = \Phi S.$$

Following the arguments from equation 3.12, we conclude that Φ commutes with S and should have a block-diagonal structure where the size of the blocks depends on the multiplicity of the diagonal values in S. Since Φ commutes with S, we get

$$M'M'^T = VSV^T = U\Phi S\Phi^T U^T = US^{\frac{1}{2}}\Phi\Phi^T S^{\frac{1}{2}}U^T = Mgg^T M.$$

Thus, the gauge matrix is a block diagonal matrix made up of complex orthogonal matrices. Since SU(2) symmetric matrices have blocks of size $(2s+1)$ where s is the spin of the irrep, the gauge matrices have a continuous degree of freedom which is hard to optimize. However, if the degeneracy is broken and the singular values are all unique, the resultant tensor has a U(1) gauge symmetry which restricts the gauge matrix to a set of diagonal matrices. The orthogonality forces the diagonal values to be ± 1. This reduces the range of the matrices g to a discrete set of size 2^D. In order to suppress the multiplicity, we introduce a very small multiplicative noise (typically of the order of 10^{-10}) to the tensor in step 1 of the SU algorithm. This slightly breaks the multiplicity of the singular values. However, this introduces another problem. Since the multiplicity breaking of singular values of different bonds can't be controlled by the noise, there is a possibility of misalignment of the virtual states. For example, a multiplicity of three would imply a virtual spin-1 particle, and the multiplet order would correspond to a particular canonical order $(S_z = -1, 0, +1)$. To handle this, optimization should include the action of a permutation matrix that reorders the degenerate vectors to minimize the asymmetry. Thus, the most general gauge transformation is given by

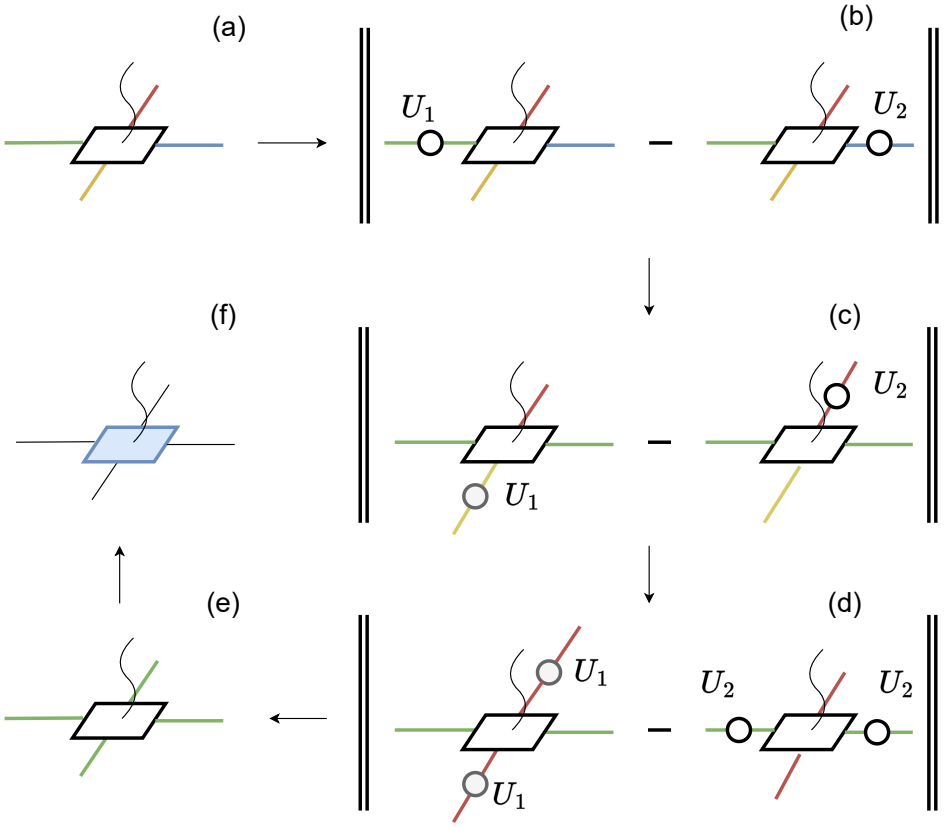

FIGURE 3.4: Gauge fixing procedure. (a) The tensor was obtained after updating all four legs. The arbitrary gauge kills the near-C_{4v} symmetry. (b) Scan the horizontal virtual indices over all the possible discreet gauges to identify the set of gauges that minimize the reflection symmetry. (c) Scan the vertical virtual indices over all the possible discreet gauges to identify the set of gauges that minimize the reflection symmetry. (d) Scan to match the basis of the four legs. (e) The resultant state is almost C_{4v} symmetry but slightly broken S(2) symmetry. (f) Restore the C_{4v} and SU(2) symmetries by projecting the tensor back to SU(2) PEPS manifold.

$$\mathcal{U} = \begin{pmatrix} \pm 1 & & \\ & \ddots & \\ & & \pm 1 \end{pmatrix} \begin{pmatrix} \mathcal{P}_{v_1} & & \\ & \ddots & \\ & & \mathcal{P}_{v_n} \end{pmatrix}, \tag{3.18}$$

where $\mathcal{V} = \oplus_{i=1}^{n} v_i$ and $\mathcal{P}_{v_i}$ is a permutation matrix in the v_i subspace (n stands here for the total number of species). This reduces all the possible gauge transformations from infinitely many continuous degrees of freedom to a discreet $2^D \prod_{i=1}^{n} \mathrm{Dim}(v_i)!$ number of possibilities. For $\mathcal{V} = 0 \oplus \frac{1}{2} \oplus 1$, this implies a 384 possible transformations. We can then scan the set of gauge matrices to reduce the asymmetry of two bonds at a time, as shown in figure 3.4.

Once the C_{4v} asymmetry is minimized, we restore the C_{4v} symmetry by averaging out the asymmetry. Once the C_{4v} symmetry is restored, we project the tensor back to the symmetric tensor basis. This restores the SU(2) symmetry of the tensor that is broken by the introduction of multiplicative noise.

Before we proceed to discuss the update schemes that involve the iPEPS environment, we shall first explain how to calculate the environment using CTMRG algorithms.

3.3 CTMRG Algorithms

In Corner Transfer Matrix formalism, as explained in section 2.3.1, we divide the translationally invariant environment into 8 sections, as shown figure 2.11-(a). The principle idea is to replace the contracted tensors in each of these regions with an approximate boundary tensor. In this section, we shall discuss how one can obtain these boundary tensors C and T for a complex-valued C_4v symmetric wavefunction. The symmetries of the individual PEPS tensor are reflected in the environment. To achieve this, we chose to perform the single-corner symmetric CTMRG. This ensures that all four corners are identical and symmetric. Similarly, the four edges T are identical and have reflection symmetry.

Now, we shall summarize the key outline of the CTMRG.

1. **Initialize C and T**: We get the initial corner by contracting two legs of the bi-layer tensor E Similarly, we get the initial corner by splitting one of the legs of the bi-layer tensor E into two legs with dimension D and then contracting them.

2. **Enlarge C**: We absorb a single site bi-layer tensor into the corner. This increases the size of the corner from $\chi \times \chi$ to $(\chi D^2) \times (\chi D^2)$.

3. **Enlarge T** We absorb a bi-layer tensor into the edge tensor. This increases the size of T from $\chi \times D^2 \times \chi$ to $(\chi D^2) \times D^2 \times (\chi D^2)$

4. **Obtain the projectors**: An appropriate projector P_i is a matrix that truncates each enlarged bond from (χD^2) to χ.

5. **Renormalize C and T**: Apply the projectors P_i on enlarged C and enlarged T and reduce them back to the best their initial size. Hence, the new corner will be $P_1 C P_2^T$ and the new edge will be $P_3 T P_4^T$ as shown in figure 3.5.

6. **Convergence** steps (b) to (f) will be repeated till the convergence criterion is satisfied.

The difference between the real and complex CTMRGs is the way we obtain the projectors that truncate the enlarged corner and edge, i.e., the steps (a), (b) & (d) remain the same. We shall now see how the projectors are obtained when the PEPS tensor is purely real and complex.

3.3.1 Real symmetric CTMRG

This form of CTMRG is useful when the PEPS is constructed from the basis tensors and purely real coefficients. Since the basis tensors themselves have only real entries, the resultant corner C is always real-symmetric, hence, Hermitian. The best approximation of this can be obtained by diagonalizing via SVD and retaining the χ largest singular values. Since the matrix is real symmetric, the eigenvalues and singular values have the same absolute value. Hence, one can use eigenvalue decomposition to approximate the reduced density matrix. Thus, the optimal projector is obtained by the orthogonal eigenvectors corresponding to χ largest eigenvalues. The whole process can be described in figure 3.5.

The SU(2) symmetry of the PEPS tensor results in degenerate singular values. In order to preserve the SU(2) symmetry, one has to prevent cutting through the multiplicities. For that, one has to discard the eigenvalues in groups. In practice, the tolerance with which the eigenvalues are grouped together is higher than the machine precision. This often results in discarding more eigenvalues than necessary. This usually implies that the dimension χ, to which the corner is truncated to, is more of an upper limit than an exact value. The estimation of information lost is the quantification of the loss due to the application of the projector. At each CTMRG step, this is given by the norm of the difference between CTMRG environment before and after truncation.

3.3.2 Orthogonal decomposition

We shall now discuss the orthogonal decomposition of a complex symmetric matrix that shall be used for the CTMRG with complex symmetric corners.

If the complex symmetric matrix A is diagonalizable, one can diagonalize it by using a set of orthogonal eigenvectors, i.e.,

$$A = ODO^T$$

where D is a diagonal matrix whose entries are the eigenvalues of A and O is an orthogonal matrix with the corresponding eigenvectors. However, most numerical

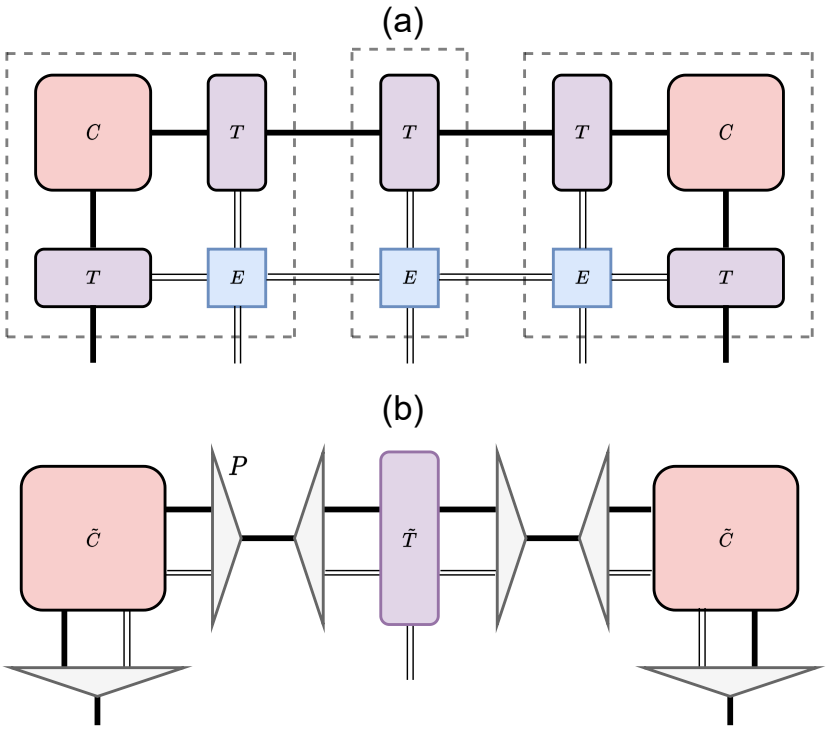

FIGURE 3.5: A simple CTMRG step. It starts with absorption of a bi-layer tensor into the corner and edge as shown in (a). Using SVD (for real corner) or orthogonal decomposition (for complex symmetric corner), obtain the right projectors P that renormalize the corner and the edge as shown in (b).

routines that are used to diagonalize a matrix do not provide us with orthogonal vectors. Hence, we shall try to extract the right orthogonal basis from a given set of eigenvectors.

In order to calculate O, we first find a set of eigenvectors E of the matrix A.

$$AE = ED \Rightarrow \quad A = EDE^{-1}. \tag{3.19}$$

Now, we use the symmetry argument $A = A^T$

$$\begin{aligned} A = EDE^{-1} = \quad A^T \quad &= (E^{-1})^T DE^T \\ \Rightarrow \quad ED = (E^{-1})^T DE^T E \quad &\Rightarrow \qquad (E^T E)D = D(E^T E). \end{aligned} \tag{3.20}$$

Note that eigenvectors of different eigenvalues of any complex symmetric matrix are always orthogonal(not orthonormal). Let u and v be two eigenvectors corresponding to two different eigenvalues λ and μ, then

$$u^T \cdot Av - (u)^T A^T \cdot v = u^T \cdot Av - (Au)^T \cdot v = \mu u^T v - \lambda v^T u = (\lambda - \mu)(u^T \cdot v). \tag{3.21}$$

If the matrix A is symmetric, the L.H.S. of the equation should be zero, and since λ and μ are distinct, the dot product $u^T \cdot v$ should be zero which can only happen when u and v are orthogonal. Hence the matrix $E^T E$ is a diagonal matrix if the A has nonrepeating distinct eigenvalues. However, in the presence of multiplicities, the matrix exhibits a block diagonal form. Unlike Takagi decomposition, this block diagonal form has to do with the absolute values of the diagonal entries D. eigenvalues which have the same absolute value but are a complex phase away(like the complex conjugate) can still have the same eigenvectors because if u is an eigenvector, the vector $e^{i\phi}u$ is also an eigenvector. We take $Z = E^T E$ and get $ZD = DZ$. Following the same arguments as in the previous section, we get, $Z^{\frac{1}{2}}D = DZ^{\frac{1}{2}}$. Notice that the square root of Z should also have the same block diagonal form as Z. Then, we get

$$\begin{aligned} A = EDE^{-1} = EDE^{-1}(E^T)^{-1}E^T = EDZ^{-1}E^T = EZ^{-1/2}DZ^{-1/2}E^T \\ \Rightarrow \quad A = (EZ^{-1/2})D(EZ^{-1/2})^T = ODO^T. \end{aligned} \tag{3.22}$$

Thus the matrix $O = EZ^{-1/2} = E(E^T E)^{-1/2}$ is a set of orthogonal eigenvectors of A. Note that in practice, eigenvectors of eigenvalues that are distinct but whose absolute values are quite close can generate very similar eigenvectors.

Relation between singular values and eigenvalues

Since both methods would give us a decomposition of the matrix into a product of a matrix and its transpose, we can try to establish a relation between them by comparing the resultant matrices. Since the number of non-zero elements of S and D is a equal to the rank of the matrix, the size of non-zero elements of S and D should be the same.

$$\begin{aligned} A = USU^T = U\sqrt{S}\sqrt{S}U^T = (U\sqrt{S})(U\sqrt{S})^T \\ A = ODO^T = O\sqrt{D}\sqrt{D}O^T = (O\sqrt{D})(O\sqrt{D})^T \end{aligned}$$

Comparing the two, we get

$$(U\sqrt{S})(U\sqrt{S})^T = (O\sqrt{D})(O\sqrt{D})^T \tag{3.23}$$
$$\implies (U\sqrt{S})\phi = (O\sqrt{D}) \tag{3.24}$$

for some complex orthogonal matrix ϕ,

$$O = U\sqrt{S}\phi\sqrt{D}^{-1}.$$

Making use of $O^T O = I$, we then obtain

$$\begin{aligned} & (U\sqrt{S}\phi\sqrt{D}^{-1})^T(U\sqrt{S}\phi\sqrt{D}^{-1}) = I \\ \Rightarrow \quad & \sqrt{S}U^T U\sqrt{S} = \phi D\phi^T. \end{aligned} \tag{3.25}$$

Taking the trace of L.H.S. and R.H.S. of equation 3.25, we get,

$$\begin{aligned} & Tr(D) = Tr(\sqrt{S}U^T U\sqrt{S}) \\ & \Rightarrow Tr(D) = Tr(S(U^T U)) \\ & \Rightarrow \textstyle\sum_{i=1}^{k} d_i = \sum_{i=1}^{k} s_i(U_i^T \cdot U_i). \end{aligned} \tag{3.26}$$

From equation 3.25, it is clear that the eigenvalues and singular values are equal if and only if the unitary U is purely real. Additionally, if the singular values are degenerate, the pre-factor term $U_i^T U_i$ need not be the same. Hence, D might not always have the exact same multiplet structure of S. This is particularly important while truncating the matrix. Since we do not want to cut through the multiplets, we should be more lenient with cutting through multiplets of D, often grouping values that are slightly off as degenerate. Additionally, we have,

$$\sum_i |d_i| = \sum_i |s_i||(U_i^T U_i)| \leq \sum_i s_i||U_i|| \leq \sum_i s_i.$$

Thus, since sum total of the magnitude of the first n eigenvalues is lower than the sum of first n singular values, we can infer that the eigenvalue spectrum decays quickly when compared to the singular values.

3.3.3 Complex-C_{4v} CTMRG

The major problem with complex CTMRG is that the eigenvalues and the singular values are not identical. While the Autonne-Takagi SVD provides the best approximation of the corner, the unitary obtained from it cannot be used as a projector since it is not orthogonal. Instead, we shall obtain the projectors from the approximation the reduced density matrix, similar to Nishino and Okanishi's original formulation of CTMRG in The reduced density matrix is formed by the four corners C^4 as shown in figure 3.6. The exact orthogonal decomposition of this reduced density matrix can change this matrix in a diagonal basis where it can be directly truncated. From equation 3.26, one can see that this orthogonal truncation is identical to the Autonne-Takagi truncation. In practice, since the orthogonal decomposition of this reduced density matrix would have the same orthogonal eigenvectors as corner C, we use the orthogonal decomposition of corner C to obtain the projectors.

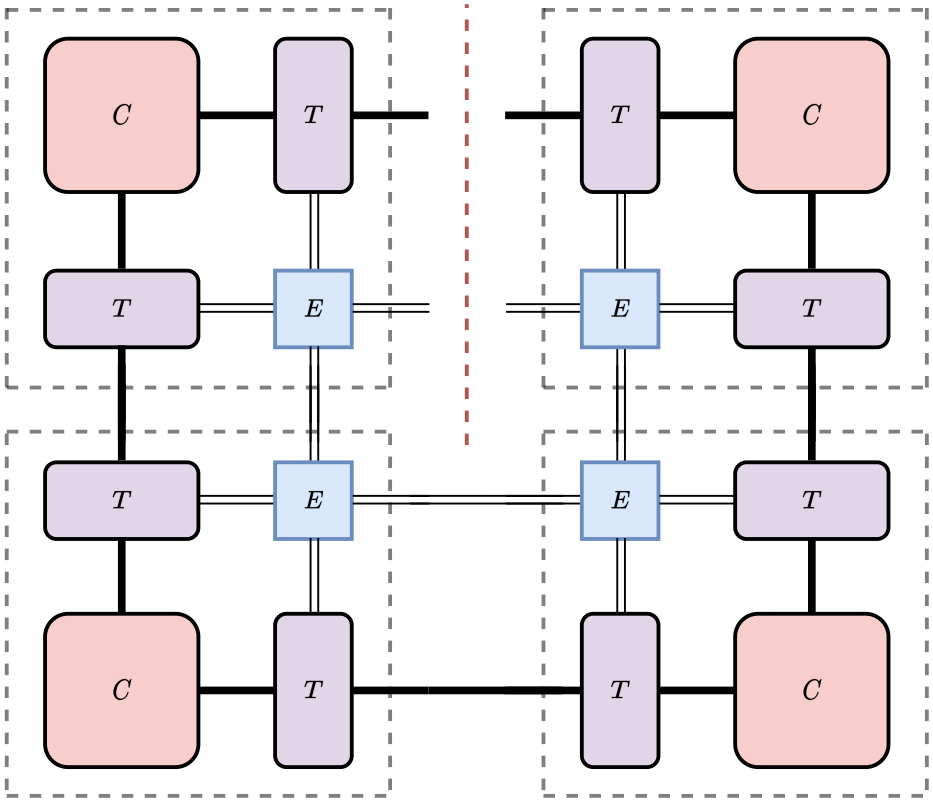

FIGURE 3.6: The reduced density matrix of the tensor network. The Projectors from the orthogonal decomposition of this matrix are the ideal projectors.

Additionally, The SU(2) symmetry of the PEPS tensor results in a multiplicity of singular values. In order to preserve the SU(2) symmetry, one has to prevent cutting through the multiplicities. For that, one has to discard the eigenvalues in groups. In practice, the tolerance with which the eigenvalues are grouped together is much higher than the machine precision, higher than the tolerance used in the real-symmetric case. In case of instability in maintaining SU(2) symmetry, this tolerance can be reduced to improve accuracy. This often results in discarding more eigenvalues than necessary. This usually implies that the dimension χ, to which the corner is truncated, is more of an upper limit than an exact value. Raising the tolerance might lead to a lower dimension and hence more significant error.

Error in complex-symmetric CTMRG

The estimate of information lost in the corner is tricky in the complex-symmetric case. Unlike the real-symmetric case, there is no exact estimate of the loss. Instead, we estimate the upper bound of the possible loss. By proving that the upper bound reduces with an increase in the final dimension, we can confirm that the quality of truncation generally increases with the final dimension.

For the upper bound, we make use of the inequality concerning the Frobenius norm of the product of two matrices, i.e., $\|AB\| \leq \|A\|\|B\|$. Let $\tilde{D}(q)$ denote the diagonal matrix with q diagonal values obtained from the orthogonal decomposition, and $\Delta(D)$ denote the diagonal values discarded. Then the loss due to truncation is given by,

$$\begin{aligned} \text{Loss} &= \|C - O\tilde{D}(q)O^T\| = \|O(D)O^T\| \\ &= \|(O\sqrt{\Delta(D)})O\sqrt{\Delta(D)})^T\| = \|MM^T\| \leq \|M\|^2 \\ \Rightarrow \text{Loss} &\leq O\sqrt{\Delta(D)}\|^2 \leq \|O\|^2\|\Delta(D)\|. \end{aligned} \tag{3.27}$$

Now, since $\Delta(D)$ has only $(p - q)$ non-zero values (where p is the dimension of the corner C before truncation), the O in the above equation can be replaced by the corresponding eigenvectors, i.e.,

$$O\Delta\sqrt{D(q)} = O_{p\times(p-q)}\sqrt{\Delta D(q)_{(p-q)\times(p-q)}}$$

Let us call this truncated O with (p q) eigenvectors as O_{reduced}. Now, since O is made up of columns of orthogonal vectors,

$$\|I_{(p-q)\times(p-q)} = \|O_{\text{reduced}}O^T_{\text{reduced}}\| \leq \|O_{\text{reduced}}\|^2.$$

Hence, we get

$$\text{Loss} \leq (p-1)\|\Delta(D) = (p-q)\sqrt{\sum_{k=q+1}^{p}|d_k|^2}. \tag{3.28}$$

Hence, as both $\sum_{k=q+1}^{p}|d_k|^2$ and $(p-q)$ go down with increasing q, we conclude that the upper bound goes down with the increase in q.

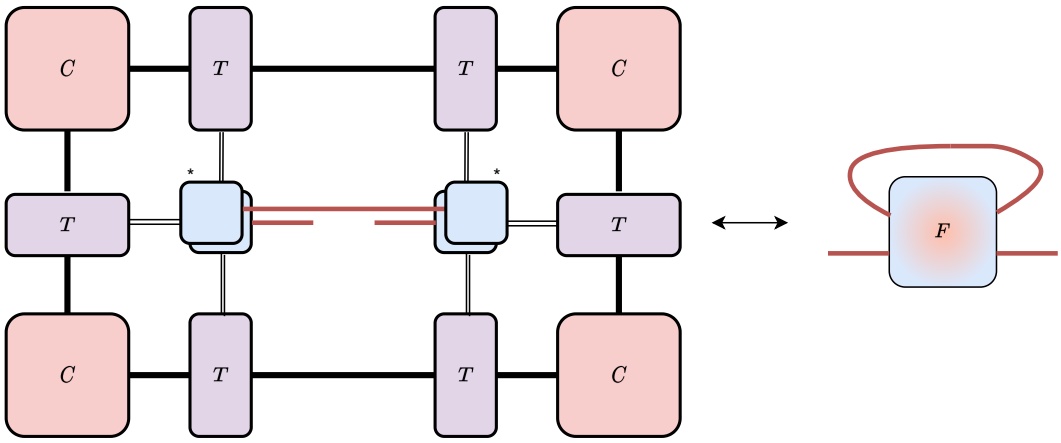

FIGURE 3.7: The full-update matrix. The comparison of the singular values of this matrix with that of the singular values of the simple update, we can infer the effect of long-range correlations. When the singular values from both matrices are similar, we can say that both truncations provide similar results.

3.4 Variational Optimisation

While the simple update procedure is a simple and efficient way to optimize the local tensor, it is totally oblivious to the effects of the environment. The result of the SU is identical whether the wavefunction describes just two sites or infinite sites. The changes in To see the effects of the environment on a bond, one can simply contract all the virtual indices of a tensor network except for the particular bond. This results in a matrix, as shown in figure 3.7. By comparing the absolute values of the eigenvalues of this "full matrix" with that of the singular values of the simple update, we can determine if the simple update is a good truncation scheme. An alternative way that considers the iPEPS into consideration is called full update (FU) [128]. In an ideal full update scenario, one applies all the commuting gates simultaneously and optimizes the enlarged bonds. However, in practice [129–131], it is assumed that the effect of all such updating has very little effect on the effective environment of the iPEPS for a short time step τ. Hence, the problem is reduced to updating the two-site PEPS, which is done by variationally optimizing the single-site PEPS tensor and hence shall be called Variational optimization (VO). Notice that this is an uncontrolled approximation and could have a significant effect on the results.

3.4.1 Evolution of CTMRG

Before we go into the specifics of the algorithm, we shall first discuss how the corner and the edge tensors are expected to evolve over time evolution. Considering the fact that the spectrum of the reduced density matrix is preserved under the action of a unitary operator and that the reduced density matrix can be represented by the contraction of four corners, as shown in figure 3.6, we conclude that the spectrum of the corner matrix should remain invariant under time evolution. In fact, one can quantify the validity of an algorithm by measuring the deviation of the spectrum of the corner. So does this mean one can avoid performing CTMRG entirely and recycle the CTMRG of the initial state? The answer is no because one still has to update the edge

tensor T. Since it is an approximation of a single column of tensors, the effect of the PEPO is very significant. However, we use the fact that while optimizing the tensor in various substeps of the variational optimization, we need not really be worried about the fact that the CTMRG is not being updated for the individual substeps.

3.4.2 VO algorithm

Unlike in simple update, the varitational optimization minimizes the distance between the resultant wavefunction $|\psi\rangle$ and the wavefunction $U(\tau)|\phi\rangle$ by maximizing the fidelity, defined as,

$$\mathcal{F}(\lambda_k) = \frac{|\langle\psi(\lambda_k)|U(\tau)|\phi\rangle|}{\sqrt{(\langle\psi(\lambda_k)|\psi(\lambda_k)\rangle\langle\phi|\phi\rangle)}}, \tag{3.29}$$

where λ_k are the coefficients that are used to construct the variational PEPS tensor as discussed in section 2.2.2. The overlap $\langle\phi|\phi\rangle)$ is a two-site overlap with the environment obtained from the CTMRG scheme. Notice that $\mathcal{F}$ is a non-linear scalar function. One can use gradient-based optimizations like the conjugate gradient method [132] to optimize it w.r.t the coefficients of the tensors [133]. Since the fidelity $\mathcal{F}$ can be expensive to compute, one can reduce the number of coefficients by optimizing the tensor over the manifold with the symmetries that can be expected from the resultant tensor. The variational optimization can be summarized in the following steps:

1. *substep-1:* Apply the gate $\mathcal{G}_a$ to the two one-site tensors $\mathcal{A}$. Construct a tensor with C_s symmetry as explained in section 2.2.2. Find the fidelity $\mathcal{F}$ by finding the overlap, as shown in figure 3.8-(a). Optimize the tensor by using a conjugate-gradient routine to maximize the fidelity $\mathcal{F}$ over the coefficients of basis tensors with C_s symmetry.

2. *substep-2*: Apply the gate $\mathcal{G}_c$. Optimize the tensor by using a conjugate-gradient routine to maximize the fidelity $\mathcal{F}$ over the coefficients of basis tensors with C_s symmetry by using the coefficients obtained from substep-1 as the starting point of the optimization.

3. *substep-3*: Apply the gate $\mathcal{G}_c$. Now, the system has completely broken symmetry; hence use the tensor basis with no spacial symmetry to optimize the overlap.

4. *substep-4*: Apply the gate $\mathcal{G}_d$. At this substep, one can either use the tensor basis with no spacial symmetry and then symmetrize the resultant tensor, or we can consider the fact that the C_{4v} symmetry is broken only in the order of τ^2, and use the C_{4v} symmetric basis to find the tensor that maximizes the fidelity.

Once the tensor at a site is updated, we use it to construct the environment for the next step. The value of fidelity obtained at each step gives us an idea of the validity of the update. If the optimization is perfect, then the fidelity value is exactly one. The deviation of the fidelity from this maximum value is a good quantification of the error that arises from restricting the Hilbert space by keeping the bond dimension

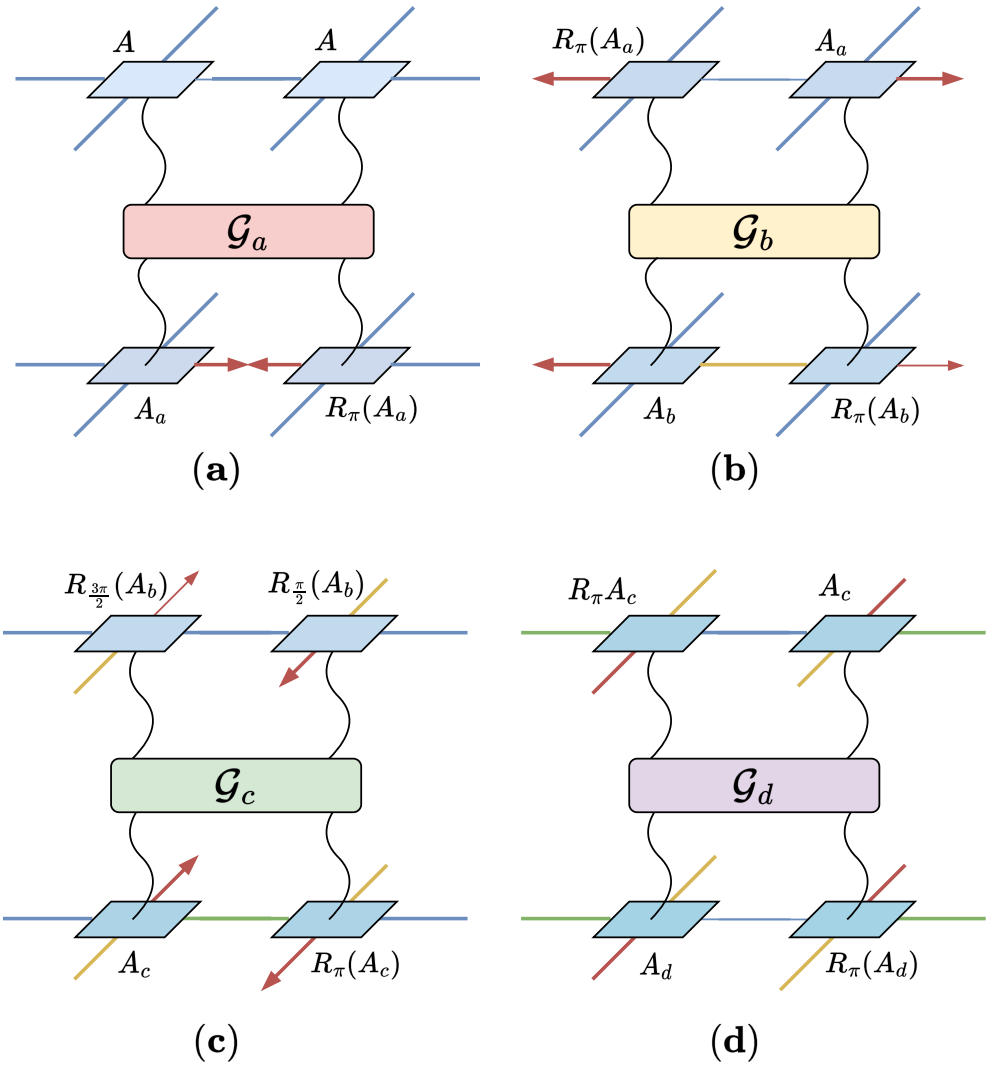

FIGURE 3.8: The variational optimization scheme involving four bonds. The open bonds in each of the subfigures are contracted with the two-site environment obtained from CTMRG, which is kept constant in all four substeps. The red arrows indicate the initial bond, which is updated on the initial step. The arrows and the colors of the bonds are useful in keeping track of the rotations on the tensor. In each step, the upper tensors are kept fixed whereas the lower tensors are optimized to maximize the fidelity given by the equation 3.29. By the end of the four substeps, the resultant tensor is almost C_{4v} symmetric with an asymmetry that scales as τ^2.

fixed. Additionally, the other source of error is from restoring the C_{4v} symmetry. As discussed earlier, the individual gates are unitary. Hence, before restoring the C_{4v} symmetry, the Environment can be considered to be exactly identical to the initial environment. By restoring the C_{4v}, we break the unitary nature of the PEPO. This implies that the environment is no longer invariant and has to be re-evaluated after every Trotter step.

3.4.3 Simplified VO

Over the course of performing the variation optimization, we notice that the optimization of the fidelity is computationally very expensive. Particularly when we work with critical states that demand large χ and large D. Hence, we introduce a simplified version of the variational optimization to reduce the computation burden while trying to stay as accurate to the complete variational optimization as possible. We have a simplified version of Suzuki-Trotter expansion where one can use the increment $(\mathcal{G}_k - \mathcal{I})$ from one gate to obtain the equivalent increments from other gates.

Consider the same classification of the Hamiltonian terms as in equation 3.6 where $\mathcal{H}_a$, $\mathcal{H}_b$, $\mathcal{H}_c$ and $\mathcal{H}_d$ are identical up to a rotation. Upon performing a Taylor expansion, we get,

$$\begin{aligned} U(\tau) &= e^{-i(\mathcal{H})\tau} \\ &= \mathcal{I} - i\mathcal{H}\tau - \frac{1}{2!}\mathcal{H}^2\tau^2 + \frac{i}{3!}\mathcal{H}^3\tau^3 + \ldots \\ &= \mathcal{I} + \sum_{k=a,b,c,d} (-i\mathcal{H}_k\tau - \frac{1}{2!}{\mathcal{H}_k}^2\tau^2 + \frac{i}{3!}{\mathcal{H}_k}^3\tau^3 + \ldots) + O(\tau^2) \\ &= \mathcal{I} + \sum_{k=a,b,c,d} (\mathcal{G}_k - \mathcal{I}) + O(\tau^2) \\ &\approx \mathcal{I} + (\mathcal{G}_a - \mathcal{I}) + \mathcal{R}_{\frac{\pi}{2}}(\mathcal{G}_a - \mathcal{I}) + \mathcal{R}_{\pi}(\mathcal{G}_a - \mathcal{I}) + \mathcal{R}_{\frac{3\pi}{2}}(\mathcal{G}_a - \mathcal{I}) \end{aligned} \tag{3.30}$$

Where $\mathcal{R}_\theta$ represents the rotation operator, which rotates the tensor about an axis passing through the center and is perpendicular to all the virtual axes by an angle of θ. The resultant gate acts only on two-sites and hence has a virtual dimension of d^2. Note that $(\mathcal{G}_k - \mathcal{I})$ represents the change due to the application of the gate $\mathcal{G}_k$. Hence, while performing optimization, one can simply perform an optimization on $\mathcal{G}_k$ and then calculate the change $(\mathcal{G}_k - \mathcal{I})$ and then apply the rotation operator on it.

Since the increments from different gates are identical and differ only by rotation and reflection. One can do the optimization once and do the appropriate rotation and reflection to obtain the increment from other gates. Hence, the simplified variation optimization can be summarized as:

1. Apply the gate $\mathcal{G}_a$ on the tensor $\mathcal{A}$. Optimize the tensor over C_s symmetry basis to obtain the updated tensor A'.

2. Obtain the increment δA,

$$\delta A = A' - \frac{(A|A')}{(A|A)} A. \tag{3.31}$$

3. Calculate the resultant tensor by applying the increment from all the four gates that are given by

$$A(t+\tau) = A(t) + \delta A + \sum_{n=1}^{3} \mathcal{R}^n(\delta A). \tag{3.32}$$

where $\mathcal{R}$ is the rotation by $\frac{\pi}{2}$ operator that acts on the local tensor.

Chapter 4

Time evolution of a critical RVB state

We shall now use all the methods explained so far to study the real-time evolution of the nearest-neighbor Resonating Valance Bond (NN-RVB) state. The results primarily consist of the data obtained from the simple update results published in reference [134].

4.1 The nearest-neighbor RVB state

The NN-RVB state was originally put forward by Anderson in 1972 [22] as a possible ground state candidate for triangular lattice and later as a possible explanation of high-Tc superconductivity in cuprates [135] and has been extensively studied ever since [136–138].Before we move on to the time evolution of this state, we shall spend some time understanding this state better.

4.1.1 Definition and properties

If we have a lattice of atoms, with a single particle at each site, like a lattice with half-filled electrons, we can pair up all the electrons into singlets(Valence bonds). Any such valence bond configuration can be represented as a product state. A resonating valence bond state is a superposition of several valence bond configurations such that the resultant state breaks no lattice symmetries. A nearest-neighbor RVB state is obtained by taking the equal-weight superposition of all the possible configurations that have each site paired with one of the nearest neighbours such as the configuration shown in the figure 4.1-(a). It has been shown that this state can be exactly represented by a PEPS tensor with bond dimension D=3 [139] and virtual space $V = 0 \oplus \frac{1}{2}$. For a square lattice, this corresponds to a PEPS tensor with rank-5, of which 4 are virtual indices and one physical index. The PEPS tensor can be seen as a projection from the virtual subspace $V^{\otimes 4}$ onto the physical spin-$\frac{1}{2}$ subspace. From the SU(2) fusion rules, it is known that it takes an odd number of half-integer spins to get a spin-$\frac{1}{2}$. Hence we have two classes of tensors, one which has three spin-0 and one spin-$\frac{1}{2}$, i.e., the occupation number $n_{\text{occ}} = \{3, 1\}$ and another which has three spin-$\frac{1}{2}$ and one spin-0, i.e., the occupation number $n_{\text{occ}} = \{1, 3\}$. The first one corresponds to the RVB state that comprises of nearest-neighbor valence bonds. The second one consists of RVB state with longer range singlets [139, 140] as shown in the figure 4.1-(b). The relationship between longer-range singlets and tensors with $n_{\text{occ}} = \{1, 3\}$ can be understood through the concept of teleportation bond as explained in figure 4.2. Using this information and the scheme to obtain basis Tensors that can be used to construct any C_{4v} PEPS tensor as described in section 2.2.2, we obtain two orthogonal tensors T_1 and T_2 using which we can construct any SU(2)-symmetric $D = 3$ C_{4v} PEPS by,

$$A_{RVB} = \lambda_1 T_1^{D=3} + \lambda_2 T_2^{D=3} \tag{4.1}$$

Since we are considering only the nearest-neighbour RVB state $\lambda_1 = 1.$ and $\lambda_2 = 0.$, the PEPS tensor is given by,

$$\begin{aligned} T_1 \quad = \quad & |0\rangle \left(\langle 0222| + \langle 2022| + \langle 2202| + \langle 2220|\right) \\ & + |1\rangle \left(\langle 1222| + \langle 2122| + \langle 2212| + \langle 2221|\right) \end{aligned} \tag{4.2}$$

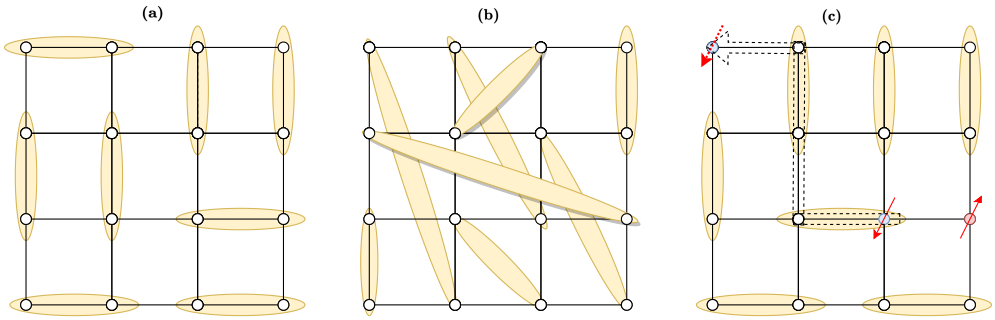

FIGURE 4.1: (a) An example of nearest neighbor valence bond configuration. The NN-RVB state is the equal-weight superposition of all such configurations. (b) A VBS with long-range dimers. (c) A spinon excitation in a NN VBS state. The dotted line corresponds to the path taken by a spinon.

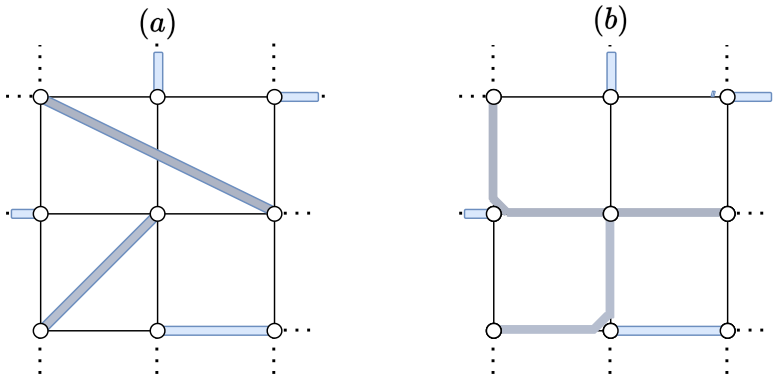

FIGURE 4.2: An example of RVB configuration with long-range singlets. Notice that a single long-range singlet can be 'teleported' along other lattice sites. The tensor of the sites through which this singlet teleports can be constructed by a PEPS tensor with $\mathcal{V} = 0 \oplus \frac{1}{2}$ and occupation number $n_{\text{occ}} = \{1, 3\}$

.

where the index 0 and 1 correspond to the spin-up and spin-down, while index 2 corresponds to spin-0. It has been shown that the RVB phase with $0.85(5) < \frac{\lambda_2}{\lambda_1} < 2.85(5)$ hosts a topological $\mathbb{Z}_2$ spin liquid phase [48] with deconfined spinons.

4.1.2 Height model and U(1) gauge symmetry

For a square lattice, the height representation is a way of mapping a quantum dimer model to a continuum theory [141, 142]. The idea is to assign a height field at the center of every plaquette, and as we move from one plaquette to the next, for an even site, the value of the height field changes by +3 in the presence of a singlet and by -1 otherwise. Similarly, for and odd sites, the height changes by -3 and +1, respectively. To give a final value to the height field, once can fix the height field of an arbitrary plaquette to zero. While at a local level, the height field is discreet and might have local fluctuations, the coarse-graining of this field will result in a continuous field. For such a description, the removal (or introduction) of a singlet on

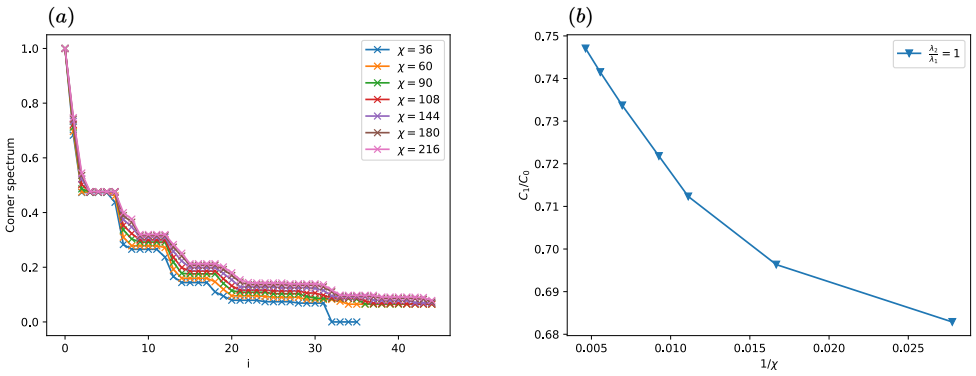

FIGURE 4.3: The corner spectrum of the NN-RVB iPEPS. Plot (a) shows the decay in spectrum for various values of χ. Plot (b) shows the sub-leading value for increasing value of as a function of χ. We notice that the spectrum does not approach a fixed value with the increase of χ.

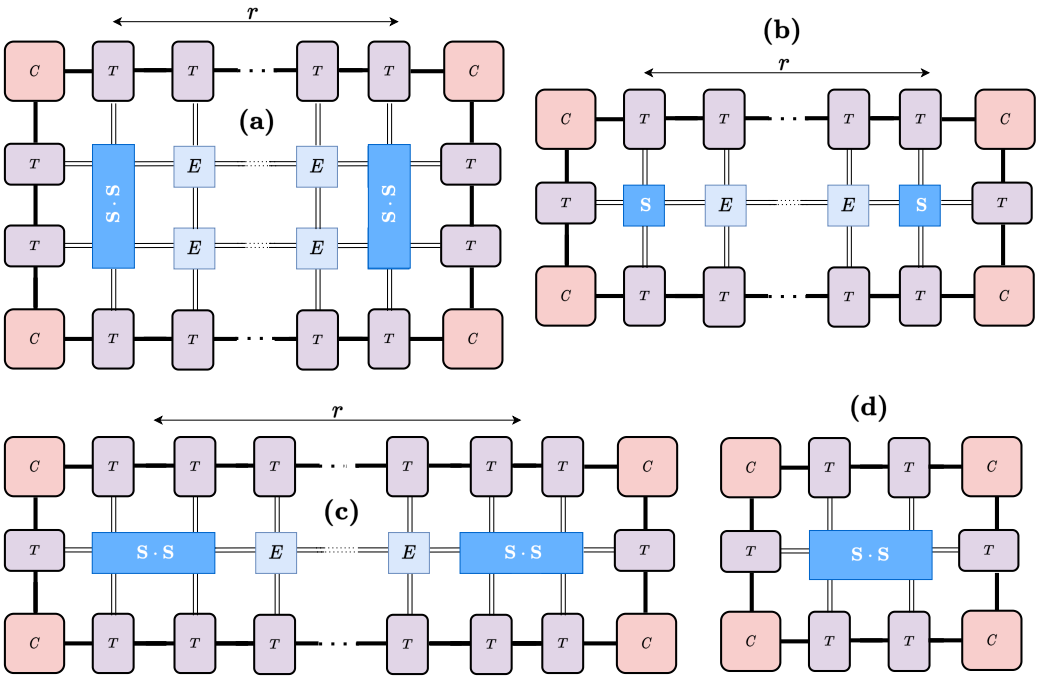

FIGURE 4.4: (a) Transverse dimer-dimer correlations $\langle D \cdot D(r)\rangle_T$ (b) Spin-spin correlations $\cdot S(r)\rangle$ (c) Longitudinal dimer-dimer correlations $\langle D \cdot D(r)\rangle_L$ (d) Heisenberg Hamiltonian $JS_i \cdot S_j$.

a bond shared by two plaquettes changes the height by -4 (or -4). If we considers a closed loop configuration such that the bonds can be rearranged within the group without influencing the height field outside the loop, the difference in the height field for such configurations will be ±4 whereas the effective action of the state as a whole remains invariant. With this, we can conclude that changing $h(x) \rightarrow h(x) + 4$ in a region does not change the description of the state. Based on this, we can conclude that the 'potential' of this height field can only have $\cos(4\pi n\phi)$ term with n an integer and $\phi(x)$ is a compactified field $\phi(x) = \frac{\pi}{2}h(x) \in [0, 2\pi)$. As we coarse-grain, only terms with a minimal number of space derivatives survive, i.e., only the elastic term $|\nabla(h)|$ survives. Hence, we can say that the effective long-distance properties can be captured by a sine-Gordon model,

$$S_{\text{eff}} = \int d\mathbf{r} \left(K|\nabla h(\mathbf{r})|^2 + \sum_{n=4,8,12,\ldots} V_n \cos(2\pi n h(\mathbf{r})) \right) \tag{4.3}$$

A 2d sine-Gordon model has two clear phases depending on the relevance of the V_n term compared to the stifness term $K|\nabla h(r)|$, a *smooth* phase where $K > \frac{n^2}{4}$ and V_n is relevant and a *rough* phase where $K < \frac{n^2}{4}$ and the cosine terms are renormalized to zero. In coulomb gas terms, the rough phase is analogous to a particle conserving U(1) Gauss law.

For the NN-RVB, every configuration has exactly one singlet per site. This implies that the change in height field around a lattice point is always zero (one singlet bond causes ±3 and three empty bonds to return ∓1) as shown in figure This implies that, in the coarse grain model, the height field is essentially flat and the stiffness term $K|\nabla h(r)|$ doesn't dominate, and the system remains critical. In fact, a similar statement can be made for the state that has exactly $n_{\text{occ}} = 1, 3$ at every site. The height field around every site adds up to a 4π (due to three singlet bonds and one empty bond and $\phi(x) = \frac{\pi}{2}h(x) \in [0, 2\pi)$ argument). Using an electric field analog, this constant flux can be interpreted as the presence of a fixed charge and the entire state obeying a fixed particle number conserving 'Gauss' law [46, 142].

However, the same cannot be said about a state that is a linear superposition of these two states, as it would imply that the resultant state has some nearest-neighbor singlets and other long-range singlets leading. During the course of the time evolution, it would be interesting to see if the Hamiltonian quench introduces long-range singlets and the effect it has on U(1) symmetry.

A consequence of the U(1) gauge symmetry is that the state exhibits critical dimer-dimer correlations that decay algebraically [143]. The dimer-dimer correlations are defined as,

$$\begin{aligned} C_d^L(r) &= \langle D_i^x D_{i+r\cdot e_x}^x \rangle - \langle D_i^x \rangle \langle D_{i+r\cdot e_x}^x \rangle \\ C_d^T(r) &= \langle D_i^y D_{i+r\cdot e_x}^y \rangle - \langle D_i^y \rangle \langle D_{i+r\cdot e_x}^y \rangle \qquad (4.4) \\ C_s(r) &= \langle \mathbf{S}_i \cdot \mathbf{S}_{i+r\cdot e_x} \rangle \qquad (4.5) \end{aligned}$$

where the dimer operators are defined as $D_i^x = \mathbf{S}_i \cdot \mathbf{S}_{i+e_x}$ and $D_i^y = \mathbf{S}_i \cdot \mathbf{S}_{i+e_y}$ as shown in figure 4.4. We also note that the critical nature of the state implies that

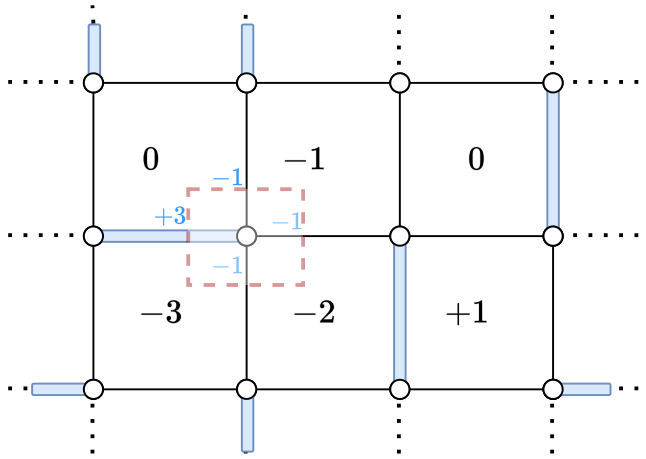

FIGURE 4.5: Height representation of a typical NN-RVB configuration. The height value of the top-left plaquette is fixed to zero. A clockwise move around the odd-site changes the height value by −1 if there is no singlet bond and +3 in the presence of a singlet bond. For the even sites, the same rule applies except for the direction, which has to be counter-wise. Notice that the change about a lattice point is always zero because of the single bond per site constraint.

the values of the corner spectrum at the point of convergence never settle to a fixed set of values even if we steadily increase χ. Figure 4.3 shows the corner spectrum for various values of χ. Despite this, as we increase the value of χ, the expectation values converge to a finite value.

4.2 Time evolution

This section contains the results of the real-time evolution of NN-RVB state described above under a Hamiltonian quench.

4.2.1 Quench setup

With the NN-RVB on a infinite square lattice as the starting point, we assume a global Hamiltonian quench at t=0, by turning on the anti-ferromagnetic nearest-neighbour (NN) Heisenberg Hamiltonian,

$$\mathcal{H}(t) = \begin{cases} 0, & \text{for } t \leq 0 \\ H = \sum_{\langle i,j \rangle} J\mathbf{S}_i \cdot \mathbf{S}_i, & \text{for } t > 0 \end{cases} \tag{4.6}$$

For convenience, we shall measure the energy in units of J, i.e., $J = 1$. Both the initial state and the Hamiltonian H are SU(2) invariant. If we were to construct a PEPO from the two-site term, the virtual bond would contain a $V = \frac{1}{2} \otimes \frac{1}{2} = 0 \oplus 1$. As we have seen in section 3.1.2, the time evolution operator can be broken down into an exponential of the two-site operator, which shall also contain the same virtual space. Additionally, since time evolution is an algebraic function of the Hamiltonian, the expectation value is expected to stay constant. The expectation value of the Hamiltonian for the initial NN-RVB state for $\chi = 180$ is ~ 0.59185 (in units if J).

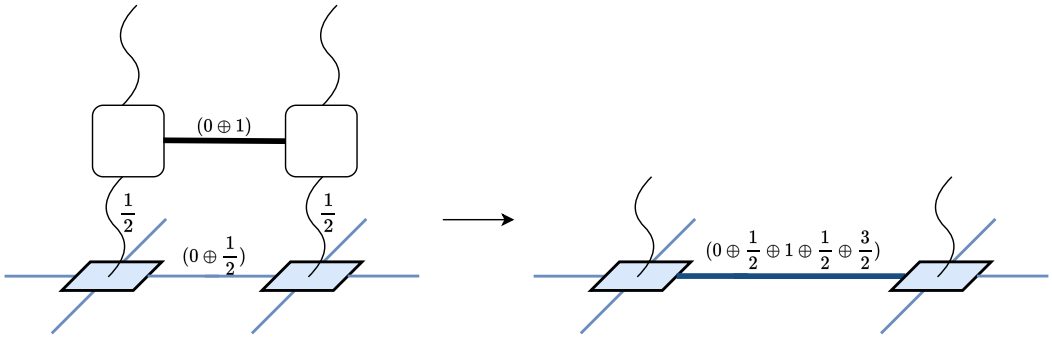

FIGURE 4.6: The resultant virtual space after the application of the time evolution gate. The new virtual space has a dimension $D = 12$ with $\mathcal{V} = (0 \oplus \frac{1}{2} \oplus 1 \oplus \frac{1}{2} \oplus \frac{3}{2})$. Using the respective weights of the individual spins, we decide on using the $D = 6$ tensors with $(\mathcal{V} = 0 \oplus \frac{1}{2} \oplus 1)$ to best capture the dynamics of the NN-RVB state.

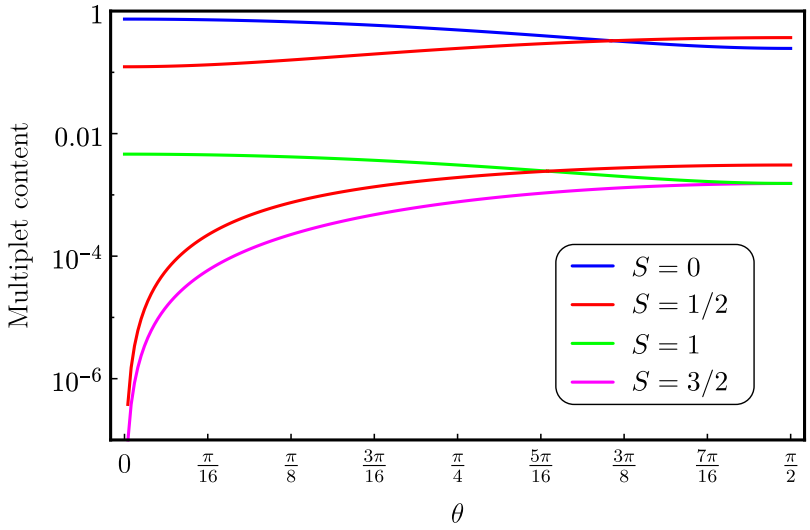

FIGURE 4.7: The singular values of the Autonne-Takagi factorization of two-site tensor after absorption of the time evolution gate G_a as a function of θ where $\lambda_1 = \cos(\theta)$ and $\lambda_2 = \sin(\theta)$.

4.2.2 Virtual space

As noted before, the breaking down of the Heisenberg Hamiltonian and the time evolution operator reveals that the virtual space of the PEPO contains a virtual space of $V = (0 \oplus 1)$. When one acts the time evolution operator onto the NN-RVB state, the resultant bond dimension would have a virtual space of $V = (0 \oplus 1) \otimes (0 \oplus \frac{1}{2}) = 0 \oplus \frac{1}{2} \oplus 1\frac{1}{2} \oplus \frac{3}{2}$ as shown in figure 4.6. The relative weights of each of these virtual spins can be calculated from the spectrum of the bond dimension obtained from the simple update. In figure 4.7, we show how the weights of the virtual spins various values of λ. From it we conclude that a bond dimension of D=6 along with the virtual space of $V = (0 \oplus \frac{1}{2} \oplus 1)$ as the ideal virtual space to describe the time evolution of NN-RVB state. To ensure that this isn't altered by the effect of the environment, we also calculate the spectrum of the "Full update matrix" and notice that it agrees quite well with the singular values of the simple update.

D	$\mathcal{V}$	C_s	C_s/U(1)	C_{4v}	C_{4v}/U(1)
3	$0 \oplus \frac{1}{2}$	7	4	2	1
6	$0 \oplus \frac{1}{2} \oplus 1$	41	30	11	8

TABLE 4.1: Number of SU(2)-symmetric local tensors of bond dimension $D = 3$ or $D = 6$, virtual space $\mathcal{V}$, C_s or C_{4v} point-group symmetry, and with/without U(1) gauge symmetry (see text). The number of C_s symmetric tensors gives the number of degrees of freedom available at every time sub-step. We explicitly find that the non-U(1) symmetric tensors keep a vanishing weight under time evolution.

Once we decide on the virtual space, we can use the method discussed in chapter2 to construct a basis of tensors. With $V = (0 \oplus \frac{1}{2} \oplus 1)$, the possible occupation numbers of virtual spin-0, spin-$\frac{1}{2}$ and spin-1 at each site that can be projected to a physical spin-$\frac{1}{2}$ space are $n_{\text{occ}} = \{1,3,0\}, \{3,1,0\}, \{0,3,1\}, \{2,1,1\}, \{0,1,3\}, \{1,1,2\}$. Notice that the first two in the list correspond to the a tensor basis with bond dimension D=3. The resultant lattice-C_{4v}/spin-SU(2) symmetric tensor basis $\{T_a\}$ contains a set of 11 real-valued orthogonal tensors. Using these one can construct any complex-valued C_{4v}/spin-SU(2) symmetric PEPS tensor by,

$$A(t) = \sum_{a=1}^{1} \mu_a(t)\, T_a, \tag{4.7}$$

where $\mu_a(t) \in \mathbb{C}$. An overview of the basis tensors for D=3 and D=6 with C_{4v} and C_s symmetries is given the table 4.1

4.3 Simple update results

In this section, we shall discuss the results obtained from the simple update scheme for the quench setup described above.

4.3.1 PEPS

First, we would like see if the virtual space $V = (0 \oplus \frac{1}{2} \oplus 1)$ captures the state better than others. Since entanglement quickly grows with time, we expect the other virtual states to become more significant. This can be observed from the fact that the weights of the singular values corresponding to the other discarded states increases with time as shown in figure 4.6. However, we also observe that the 3 multiplets of D=6 stay well above the rest of the spectrum. We also observe that singular values of the 3 multiplets of D=6 tend to become equal in order to reach the maximum available entanglement entropy $S_{max} = \ln(D) = \ln(6)$. In figure 4.8-(a), we plot the singluar values λ_i obtained from the Autonne-Takagi decomposition of the simple-update procedure and the corresponding bond entanglement entropy $S_{D=6} = -\sum_{i=1}^{6} \lambda_i \ln(\lambda_i)$.

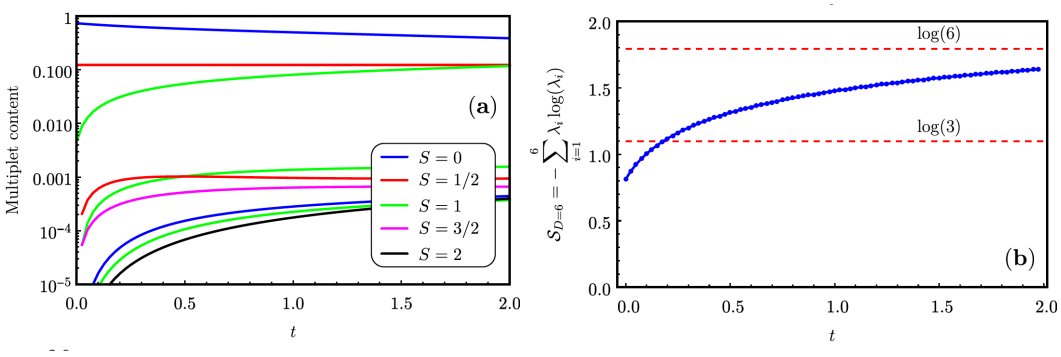

FIGURE 4.8: (a) Singular values λ_i of the Autonne-Takagi factorization of the SU gate matrix represented in figure 4.6. (b) The bond entanglement entropy obtained using the singular values shown in subplot (a) $S_{D=6} = -\sum_{i=1}^{6} \lambda_i \ln(\lambda_i)$.

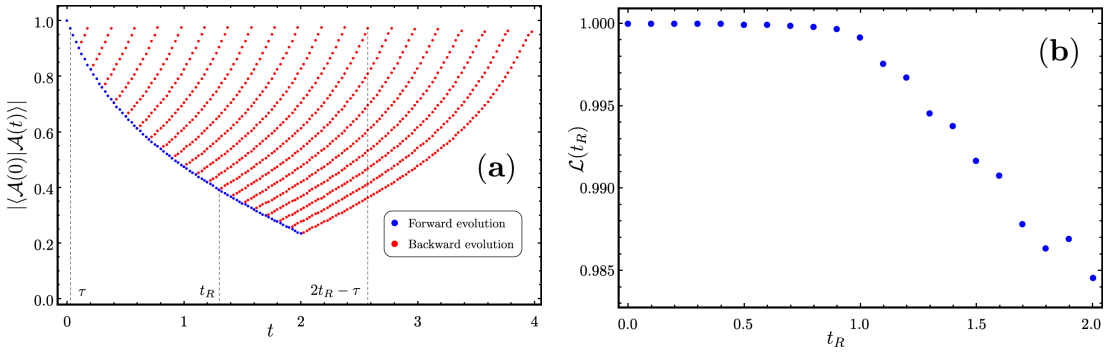

FIGURE 4.9: (a) Overlap $|\langle \mathcal{A}(t)|\mathcal{A}(0)\rangle|$ of the time-dependent tensor with the initial tensor defining the NN RVB state ($\lambda_2 = 0$) as a function of time (blue dots). Red dots are used after time reversal at $t = t_R$, going backwards in time. (b) Loschmidt echo $\mathcal{L}(t_R) = |\langle \mathcal{A}(t = 2t_R - \tau)|\mathcal{A}(\tau)\rangle|$ vs t_R. Note that for convenience $\mathcal{L}(t_R)$ is not evaluated between times 0 and $2t_R$ but between times τ and $2t_R - \tau$ to avoid dimensional jump from $D = 3$ at time 0 to $D = 6$ at time $t > 0$. In (a) and (b) the SU method is used with $\tau = 0.025$.

Loschmidt echo

In order to establish the ultimate maximum time above which our procedure breaks down, we have performed the following "time reversal" procedure; (i) time evolution is performed with e^{iHt} from $t = 0+$ to $t = t_R$; (ii) then, at $t = t_R$ time is "reversed", $t \to -t$, i.e. time evolution is performed withe^{iHt}. In the case of an exact unitary evolution, one should recover exactly the initial NN RVB state at time $t = 2t_R$. In other words, (the modulus of the overlap) $|\langle \mathcal{A}(t)|\mathcal{A}(0)\rangle|$ of the time-dependent tensor with the initial tensor (defining the $\lambda_2 = 0$ NN RVB state) should come back to 1 at $t = 2t_R$. The Loschmidt echo is defined as the final overlap at $t = 2t_R$. We plot the overlap and the echo as a function of time in figure 4.9. We notice that the Loschmidt echo starts deviating from 1 at around $t_{max} \sim 1$. At this point, we say that evolution is no longer unitary and the small errors of the simple-update procedure cumulatively add up, and the procedure breaks.

Energy

Under unitary time evolution, the energy, defined as the expectation value of H in the time-evolving state, should be conserved. However, even if our $D = 6$ PEPS may account correctly for the increase of entanglement up to $t_{\max}^{D=6} \simeq 1$, the simple update scheme may fail to optimize properly the local tensor above some intermediate time $t_{\max}^{\mathrm{SU}} < t_{\max}^{D=6}$. We believe a good criterion to estimate the accuracy of the SU scheme is to examine the possible deviation of the energy w.r.t. its $t = 0$ value. We have to note that even though the numerical results are only valid for $t_{\max}^{D=6}$, the qualitative assertions stay relevant for t_{max}.

As explained earlier, the energy of the SU tensors is computed using the complex-symmetric Corner Transfer Matrix Renormalization Algorithm (CTMRG) iPEPS algorithm described in 3.3.3. Due to the critical nature of the wavefunction, the energy values converge very slowly. So several values of χ are considered. figure 4.10 shows the energy per site as a function of time t for χ ranging from D^2 to $3D^2$. At the smallest $\chi = D^2$ value, one clearly sees a plateau at small time $t \lesssim 0.15$ and, then, a clear deviation from the initial $t = 0$ energy. Upon increasing χ the deviation occurs even sooner. Notice the energy scale used in figure 4.10, showing that the energy deviation still remains relatively small up to intermediate time, i.e. 0.6% at $t = 0.2$.

This is possibly because the simple update truncation scheme is not the optimal truncation method for iPEPS calculations. The critical nature of the wavefunction implies that the number of iterations required for the CTMRG to converge increases rapidly with χ. With each iteration, the truncation error of a single PEPS tensor is added to the environment. Thus, the greater the number of iterations, the larger would be the error. When the error accumulated by an increase in χ is larger than the gain in accuracy, increasing the value of χ is no longer reasonable.

Now that we have established the time scale of our simulation, we shall now proceed to study the results within this time frame. In figure 4.11 we plot the time evolution of the (complex-valued) coefficients of the 11 orthogonal basis tensors described in equation (4.7).

4.3.2 Critical behavior

As explained earlier, The basis tensors involved in the construction of our local tensor in Eq. (4.7) can be grouped according to their occupation number of each of the virtual states on the four bonds $n_{\mathrm{occ}} = \{n_0, n_{1/2}, n_1\}$ (with $\sum_\alpha n_\alpha = 4$). In accordance with the SU(2) fusion rules, $n_{1/2}$ can be either 1 or 3 defining two separate classes of U(1) symmetric PEPS. As long as a tensor remains in only one of the two classes, the particle number is conserved and the wavefunction will exhibit a U(1) phase. This can be extended to other larger D. Regardless of the size of the virtual space V, the PEPS is always a projection from the virtual subspace $V^{\otimes 4}$ onto the physical spin-$\frac{1}{2}$ subspace. From the SU(2) conservation rules, the number of it takes an odd number of half-integer spins to get a spin-$\frac{1}{2}$. Thus the particle number shall always be either one or three. We observe, based on the coefficients obtained from the SU scheme,

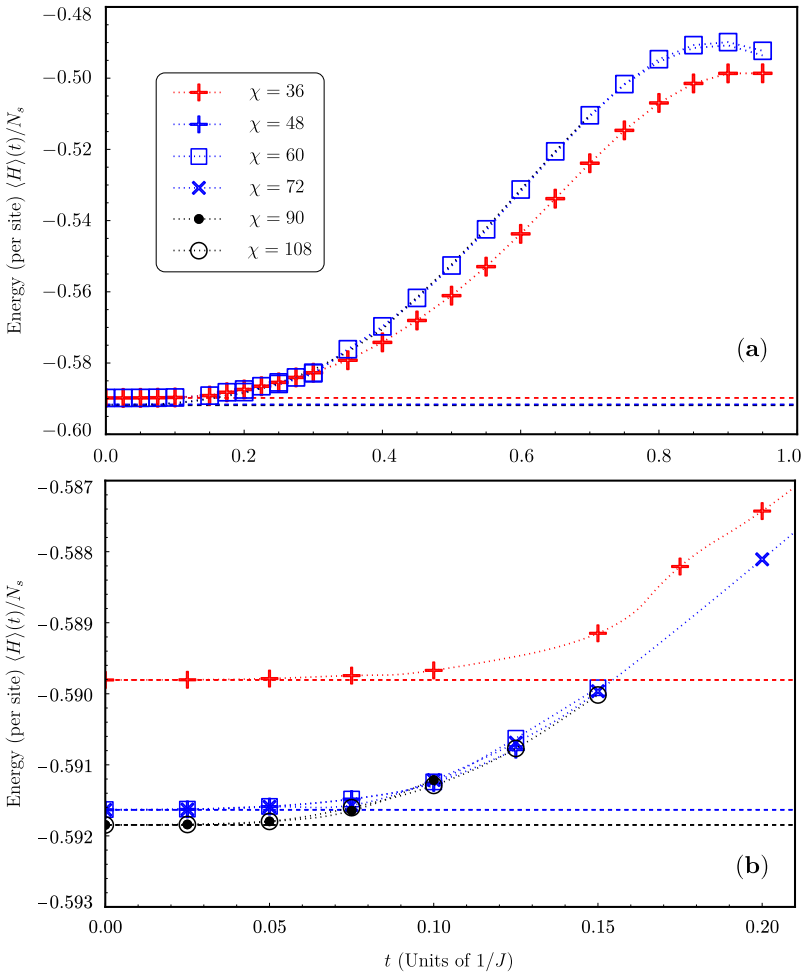

FIGURE 4.10: The energy per site of the wavefunction obtained from the iPEPS result using the $D = 6$ SU tensors.

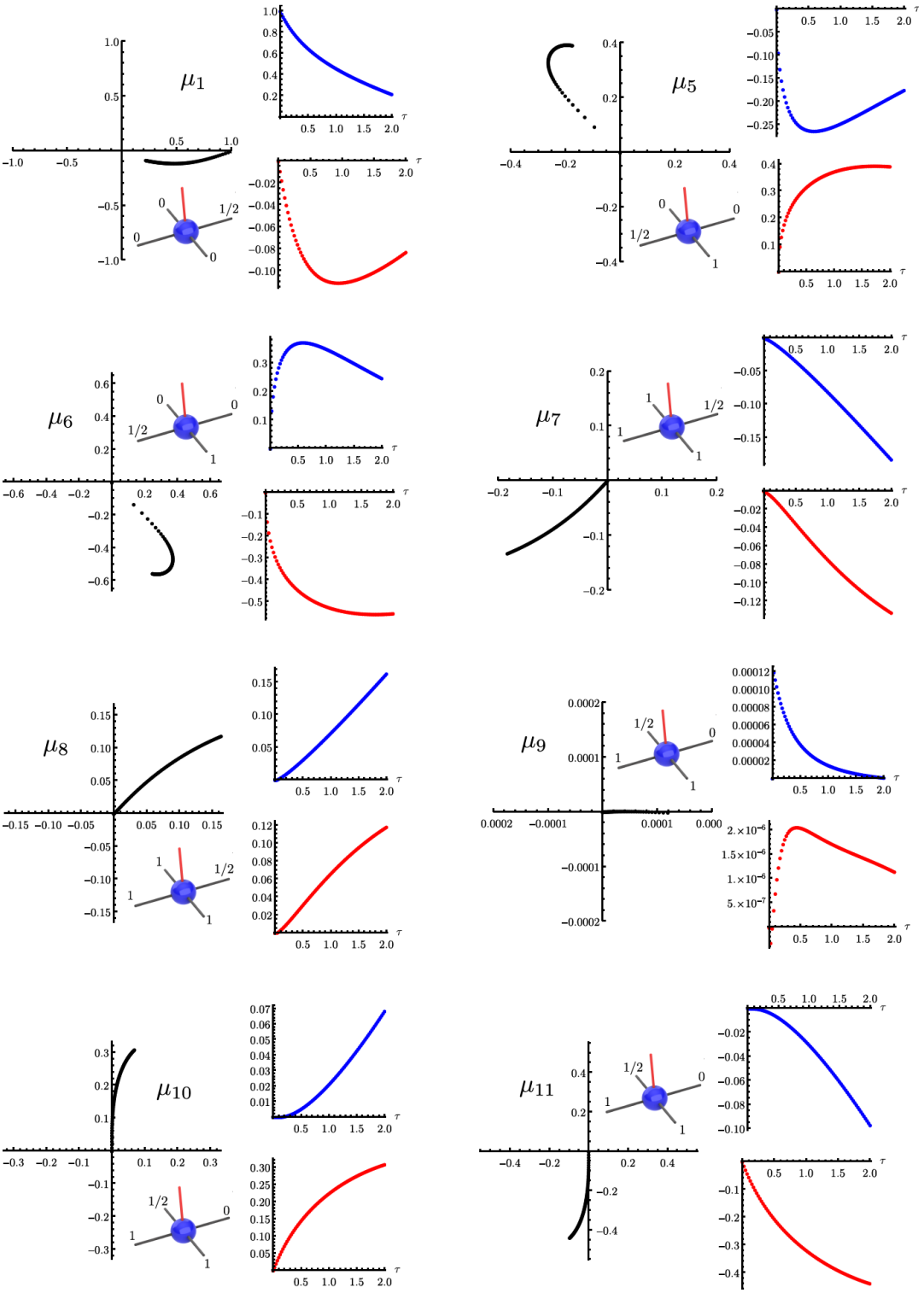

FIGURE 4.11: Time evolution of $\mathcal{A}(t)$ complex components μ_i obtained from simple update scheme with $\tau = 0.025$ in the time range $t \in [0, 2]$. In each panel μ is displayed in the complex plane (black dots) as well as its real part (blue spheres) and imaginary part (red spheres). Components μ_2, μ_3 and μ_4 being identically zero are not displayed.

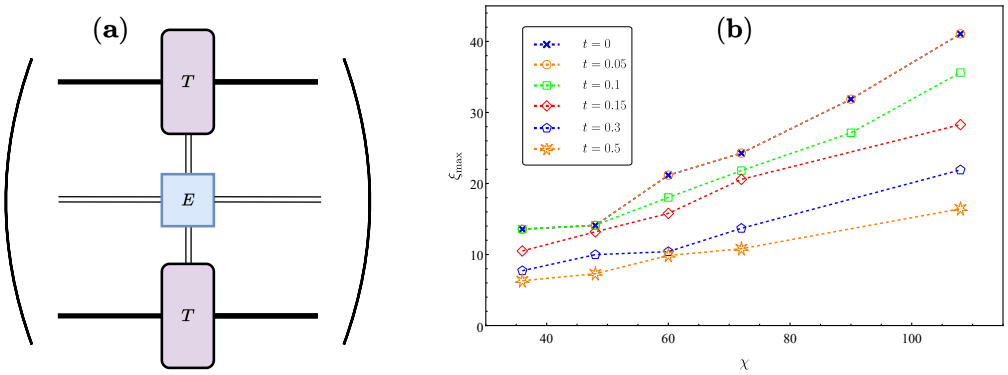

FIGURE 4.12: (a) The transfer matrix constructed using the edge tensor T. (b) ξ_{max} obtained from the log of the ratio of the leading and sub-leading eigenvalues $\frac{\lambda_2}{\lambda_1}$ of the transfer matrix shown.

that the coefficients corresponding to the $n_{1/2} = 3$ always remain exactly zero at all times. As a result of this, from the height representation mapping, we can conclude that the Coulomb phase U(1) Gauss law is upheld throughout the simulation, and the state remains critical.

To explain why we consider the virtual space of the time evolution gate $V = 0 \oplus 1$. As one applies the gate over a bond, the virtual spin S can only be changed to (S+1) or (S-1) and hence will not change the $n_{1/2}$ number. Note that the primary condition here for this to happen is that the entire operator can be decomposed into a set of two-site operators that act only on the NN-bonds. If we have a Hamiltonian that has terms other than the NN-bonds, the U(1) will be broken. Additionally, this logic can be extended to other geometries too. As long as the Hamiltonian is SU(2) symmetric and can be decomposed into a collection of only NN-terms, the time evolution of a NN-RVB state under such a Hamiltonian shall always conserve the particle number.

Transfer Matrix results

To further confirm the critical nature of the state, we construct a transfer matrix (TM) using two edge tensors T as shown in figure 4.12-(a). The spectrum of the transfer matrix implies is calculated, and the leading eigenvalue is normalized to 1. We notice that, with an increase in the value of χ, the gap between the leading and the sub-leading eigenvalue vanishes. The maximum correlation length $\xi_{\max} = -1/\ln(\lambda_2/\lambda_1)$ is then expected to diverge with χ. We notice this in figure 4.12-(b), where for the given values of χ, the plot shows no sign of saturation. This diverging maximum correlation length corresponds to the power-law decay of the dimer-dimer correlations. The multiplicity of the spectrum is used to identify the doublet and singlet sectors, and their corresponding correlation lengths can be extracted. One can then use the spin-spin correlation length calculated from the decay of the spin-spin correlation with distance to see if it matches the one obtained from the transfer matrix. An example of the spin-spin correlation length from the spin-spin correlation values is given in figure 4.14.

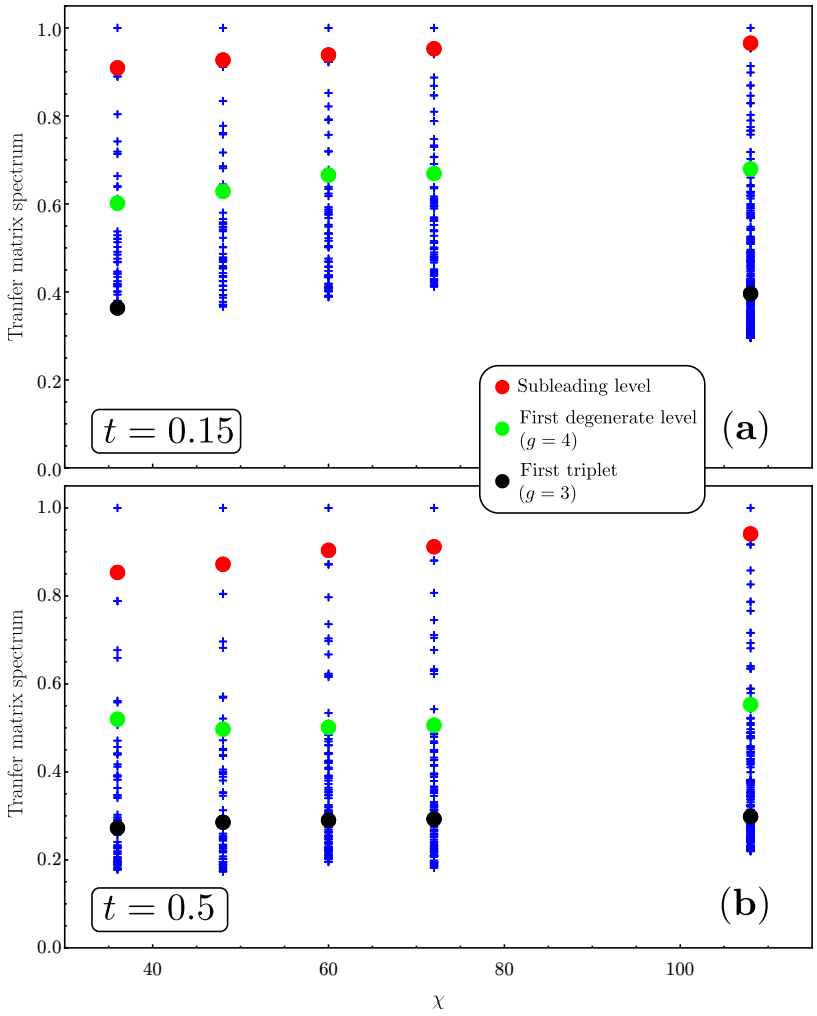

FIGURE 4.13: The full spectrum of the transfer matrix shown in figure 4.12 at $t = 0.15$ and $t = 0.5$. The red dots mark the sub-leading term, the green dots mark the first multiplet (degeneracy g=2), and the black dot represents the first triplet. The vanishing distance between the leading and the sub-leading terms indicates a diverging correlation length.

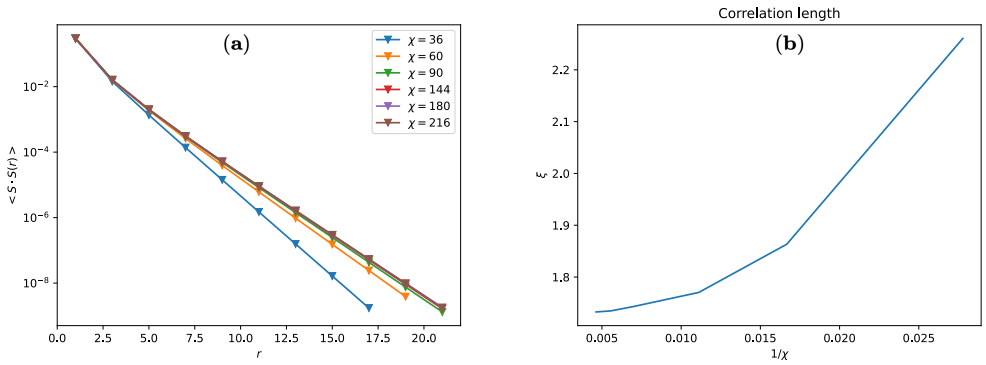

FIGURE 4.14: Spin-spin correlation values $\langle \mathbf{S} \cdot \mathbf{S}(r) \rangle$ for various values of χ. (b) The spin-spin correlation length ξ obtained from the spin-sin correlation data using $C_s(r) = C_s(r = 0)e^{-r/\xi}$.

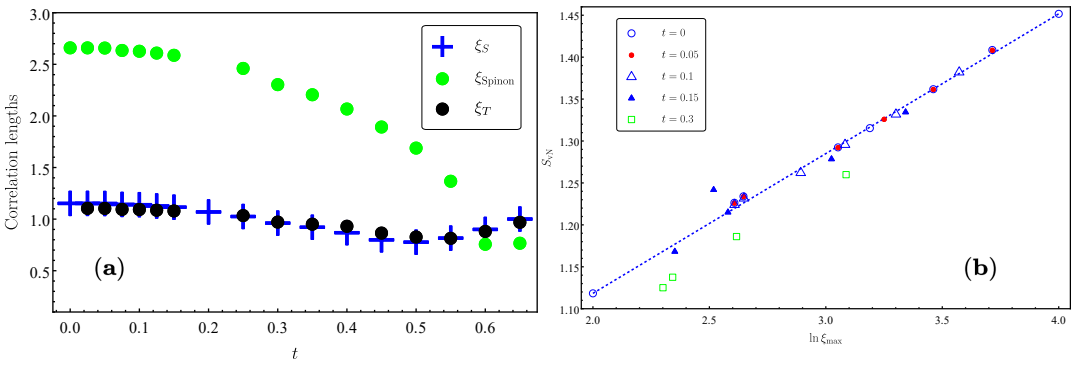

FIGURE 4.15: (a) Correlation lengths obtained from the TM obtained from the exponential decay of the multiplets as observed in 4.13 along with the spin-spin correlation length obtained by an exponential fit of the spin-spin correlation length data. (b) Entanglement entropy of the boundary MPS versus $\ln(\xi_{max})$ for different time t = 0, 0.05,0.1,0.15, and 0.3. The dotted line corresponds to slope= $\frac{1}{6}$, a behavior expected for $c = 1$.

Figure. 4.13 shows the spectrum of the transfer matrix of at times t=0, t=0.15 and t=0.5. The sub-leading term, the degenerate levels corresponding to the singlet and the doublet are marked. As expected, the sub-leading term exhibits a vanishing gap. In figure.4.15-(a) we plot the correlation lengths of the other multiplets obtained from the TM for various χ and at various times. We observe that the singlet correlation length obtained from the TM fits well with the correlation length calculated from the spin-spin correlation data.

The critical nature of the bulk PEPS is also reflected in the critical nature of the boundary MPS with central charge $c = 1$. We confirm this feature by computing the von Neumann entropy S_{vN} and fitting it with the log of maximum correlation length $\ln(\xi_{max})$. The central charge can be calculated using the relation $S_{vN} \sim \frac{c}{6} \ln(\xi_{max})$. In figure 4.15-(b), we show that the fit for $c \approx 1$ confirms the critical nature.

4.4 Variational Optimisation results

In this section, we shall discuss the results obtained from the simplified form of the variational optimization discussed in section 3.4.3. Interestingly, the results obtained from variational optimization have a significantly larger error when compared to the simple update, even at low time scales. This is despite the fact that the tensors obtained from both methods have significant overlap. Figure 4.16 shows the overlap between the tensors obtained from SU and VO methods, obtained by computing the scalar inner product of the two tensors $(A_{SU}|A_{VO})$.The plot shows a significant overlap that deviates from unity only in the order of 10^{-4}. Despite this, the energies obtained from the CTMRG results, shown in figure 4.17, are very different. This could be because of the fact that the critical dimer-dimer correlations demand a large number of CTMRG steps for the environment to converge, making the final value a highly non-linear function of the PEPS tensor. For $\chi > 2D^2$, the number of steps is usually of the

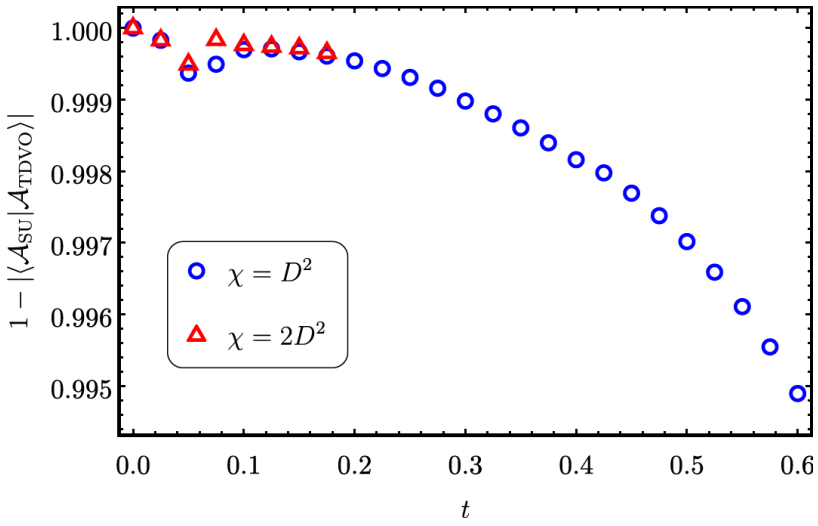

FIGURE 4.16: The overlap between the tensors obtained from the simple update (SU) and the variation optimization. We notice a strong overlap between the two tensors, the deviates from 1 is of the order 10^{-4}. Despite this, the resultant CTMRG results vary significantly, making the variational optimization results unreliable.

order 10^3 and scales exponentially with the value of χ. Hence, even if the overlap is of the order 10^3, the difference accumulates over various renormalization steps and becomes unviable after a significant number of steps. Moreover, the computation time required to perform the variational optimization is too high compared to the simple update. The computation cost itself increases drastically as we reduce the time step τ. This is primarily due to the fact that the gradient of the fidelity function is too flat for the optimization routines like the conjugate gradient to reach a minimum value. Thus we conclude that the variational scheme, which showed reliable results for imaginary time evolution, is not very useful for simulating the real-time dynamics of spin liquids with critical correlations.

Before concluding the chapter, it is also necessary to the reliability of CTMRG. One of the key challenges with CTMRG is to prevent the SU(2) symmetry of the corner. Unlike other tensors, the multiplet structure of CTMRG is less clear, making it hard to keep all the possible multiplets. Though such incidents are seldom, it is possible for two slightly different singular values to correspond to the same set of degenerate states. If we cut through such multiplets, the CTMRG will show features of symmetry breaking. One can try to avoid such instances by being lenient with multiple values, but it does not guarantee success. Such instances are more prominent if the starting point of the CTMRG iterations is a CTMRG result from a different PEPS tensor, even if the virtual space of both the PEPS tensors is exactly identical. These cases of *SU(2)-failure* are not unique to the states with critical correlations as there have been similar issues with some gapped $\mathbb{Z}_2$ spin liquid PEPS too.

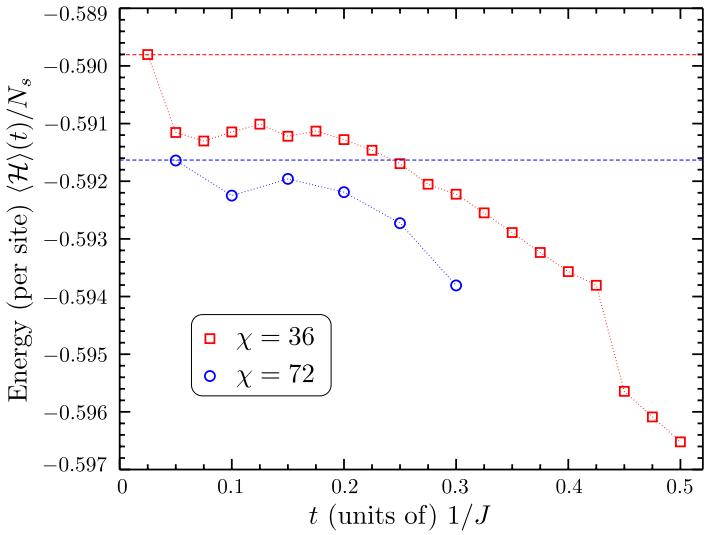

FIGURE 4.17: The expectation value of the energy with time obtained from the variational optimization procedure. We notice that the energy deviates from the initial value from the very first step and the deviation is much more significant than the result obtained from the simple update scheme.

Conclusion

In this thesis, we have used tensor networks to construct the highly entangled nearest-neighbour RVB state and study its time evolution under a Hamiltonian quench. Along the way, we have made some crucial changes that are necessary for the successful implementation of numerical techniques in the context of spin liquids. The simple update algorithm presented in this thesis can be generalized to tensors of other lattices that get more experimental attention. In any tensor network methods that use decompositions or truncations, the Autonne-Takagi decomposition and the orthogonal decomposition discussed in chapter 3 can provide symmetric decompositions. The gauge fixing method discussed in the same chapter too can be used to remove the gauge redundancy. Other tensor network methods like the tree-tensor networks (TTN) and MPS can also take advantage of these decompositions, especially when the system has symmetries that can be exploited. The methods described can also be extended to larger unit cells. The simple update of large unit cells would be similar to the traditional cluster-based methods. Using larger unit cells can also be used to probe systems with VBC phases that break translational symmetry. However, one has to take additional care in making such generalizations. In the initial stages of the thesis, the standard time evolution techniques that were successful in finite-temperature imaginary-time evolution were attempted to study the real-time dynamics. We quickly realized that such a straightforward application is not quite simple, and modifications were necessary to fit the numerical schemes to the problem.

The methods can then be used to study a variety of problems involving non-equilibrium phenomena. As explained in the opening chapter, the PEPS tensors can be used to describe some of the upcoming RVB realizations in cold atom systems. The methods described in this thesis are well suited to studying the non-equilibrium behavior of such systems. Other non-equilibrium phenomena, such as driven-dissipative systems, Floquet systems, etc. can be studied with the methods described. The successful implementation of the complex-symmetric CTMRG can give a major boost to the usage of tensor networks. Other methods that are usually used to study quantum systems with long-range entanglement suffer from the effects of finite size. Since CTMRG gives us an approximation of the system in the thermodynamic limit, it can be used to understand the nature of the system better. The numerical scheme to construct a basis of SU(2) symmetric PEPS tensors can also be extended to construct the basis tensors of other forms. This can be used to improve other tensor networks such as TTN. Future work can also involve considering the effects of temperature.

The simple update results in this thesis form the most crucial part. We have observed a lack of thermalization of the critical wavefunction and argued that any SU(2)

symmetric Hamiltonian that can be broken into a trivial sum of nearest-neighbor terms could never thermalize the NN-RVB state. The iPEPS results confirmed the conclusion that the state remained critical. The correlation length computed from the spin-spin correlation data and the edge tensor T match very well, suggesting the success of the complex-symmetric CTMRG algorithm. While the simple update gave reliable results up to a short time scale, variational optimization turned out to be harder to implement as the approximations that were made during the implementation turned out to be too significant to be ignored.

On a technical level, there is a scope for improvement in the complex-symmetric CTMRG. The complex-symmetric CTMRG breaks down occasionally and provides erroneous results. This can be spotted in the non-zero expectation values of the spin operators. In order to improve upon this, we need to have a better understanding between the eigenvalues of the corner matrix and SU(2) symmetry. Though this has been studied and well understood in real valued PEPS [144], the relationship is less clear in complex-valued CTMRG. The failure of CTMRG, even for a single value, has a major effect on the variational optimization algorithm, as its success depends on the accuracy of the CTMRG.

The single site optimization using CTMRG discussed in chapter 3 and chapter 4 also has major scope for improvement. We show that the traditional variational optimization is inaccurate and performs worse than the simple update. The multi-site full update is yet to be successfully implemented. One key idea that can improve the full update is to perform the truncation and optimization as a part of a CTMRG-step. This is akin to approximating the density matrix instead of finding an approximation that maximizes the fidelity. The enlarged PEPS tensor after applying the time evolution PEPO should keep the CTMRG invariant since the time evolution is a unitary operator. This implies that if we were to perform a CTMRG step with the enlarged tensor, the spectrum of the corner spectrum has to remain invariant. We can use this to construct a reduced CTM with all the virtual indices traced over except for the enlarged bonds. Then, in a step similar to the CTMRG step, we can use orthogonal decomposition to truncate the bond. This truncated bond of the bi-layer tensor would then give us a bi-layer tensor that minimizes the deviation of the corner spectrum. For very small values of time-step or for systems that do not have critical correlations, this method should be identical to the traditional single-site variational optimization. Additionally, one can also extend the single-corner CTMRG to study systems with C_s symmetry. If the system has reflection symmetry along both X and Y axes, then a single corner can be used to perform CTMRG. Using this, we can use C_s-symmetric Suzuki-Trotter gates to perform the variational optimization. Implementation of such work would be tricky. We also observe from chapter 4 that for the time evolution of NN-RVB state under a Heisenberg quench, the error due to truncation is much lesser than the error due to Suzuki-Trotter decomposition for $t \leq 0.05$. Hence, this region of time evolution can be used as a playground to test the accuracy of various truncation schemes.

We also note that a major part of the thesis also consisted of trying to break, restore or play with the symmetries to avoid the possible catastrophes that can arise in their

absence. In chapter 2, we have described a routine to compute a basis of SU(2) symmetric PEPS tensors for a given bond dimension D and virtual space $\mathcal{V}$. In chapter 3, we have adapted the simple update and symmetric-CTMRG for spin liquid ansatz. The implementation of the Autonne-Takagi factorization to save the symmetry of the PEPS tensor, the occasional sacrifice of SU(2) symmetry of the PEPS tensor to restore the C_{4v} symmetry, and the use of multiplets to identify the right ansatz, all demonstrate the crucial role that symmetries play in the numerical simulation of tensor networks.

Appendix A

Tensor Diagrammatics and notation

Diagrammatic notation

A tensor T is a multidimensional array of complex numbers $T_{i_1 i_2 \ldots i_p} \in C$. The rank 'p' of tensor T is the number of indices/dimensions. For instance, a rank-zero tensor (p = 0) is a complex number. Similarly, rank-one (p = 1) and rank-two (p = 2) tensors represent vectors and matrices, respectively. The size of an index i, usually denoted by d_i or $|i|$, is the number of values that the index can take, $i \in 1, 2, , d_i$.

We shall now describe the Penrose diagrammatic notation [110] used in the course of the thesis. Diagrammatic notation is a great tool in representing and thereby making it easier to understand some of the tensor manipulations. We represent tensors, matrices, and any other linear algebra object with solid shapes such as circles, squares, cubes, etc. Note that the size of the solid object is only a visual representation and has no physical meaning. The line segments originating from the shapes represent the various indices of the tensor called *'legs'*. Hence, a vector with only one dimension is represented by a single leg originating from a solid shape like a circle/square, whereas a matrix is represented by a shape with two legs, etc., as shown in figure A.1. We now describe some basic operations that are essential in all tensor network algorithms.

• *Reshaping the tensor*: In any tensor, one can fuse multiple indices to create a new index without changing the information contained in the tensor. For this, one has to find a way to map the indices of every entry to a new and unique set of indices. For example, a tensor T_{ijkl} with dimensions d_i, d_j, d_k and d_l can be recast into a tensor T'_{ijm} of dimensions d_i, d_j and $d_k \cdot d_l$ where the index of the scalar object (i, j, k, l) is changed to $(i, j, kd_k + l)$. as shown in figure A.1-(b).

• *Tensor contraction*: A tensor contraction of two (or more) indices of the same tensor is the (partial) trace of the two (or more) indices. Tensor contraction of two (or more) indices of multiple tensors is the dot product of the two tensors along those indices. For example,

$$\sum_{i_2, i_3} A_{i_1 i_2 i_3 i_4} = A_{i_1 i_4}$$

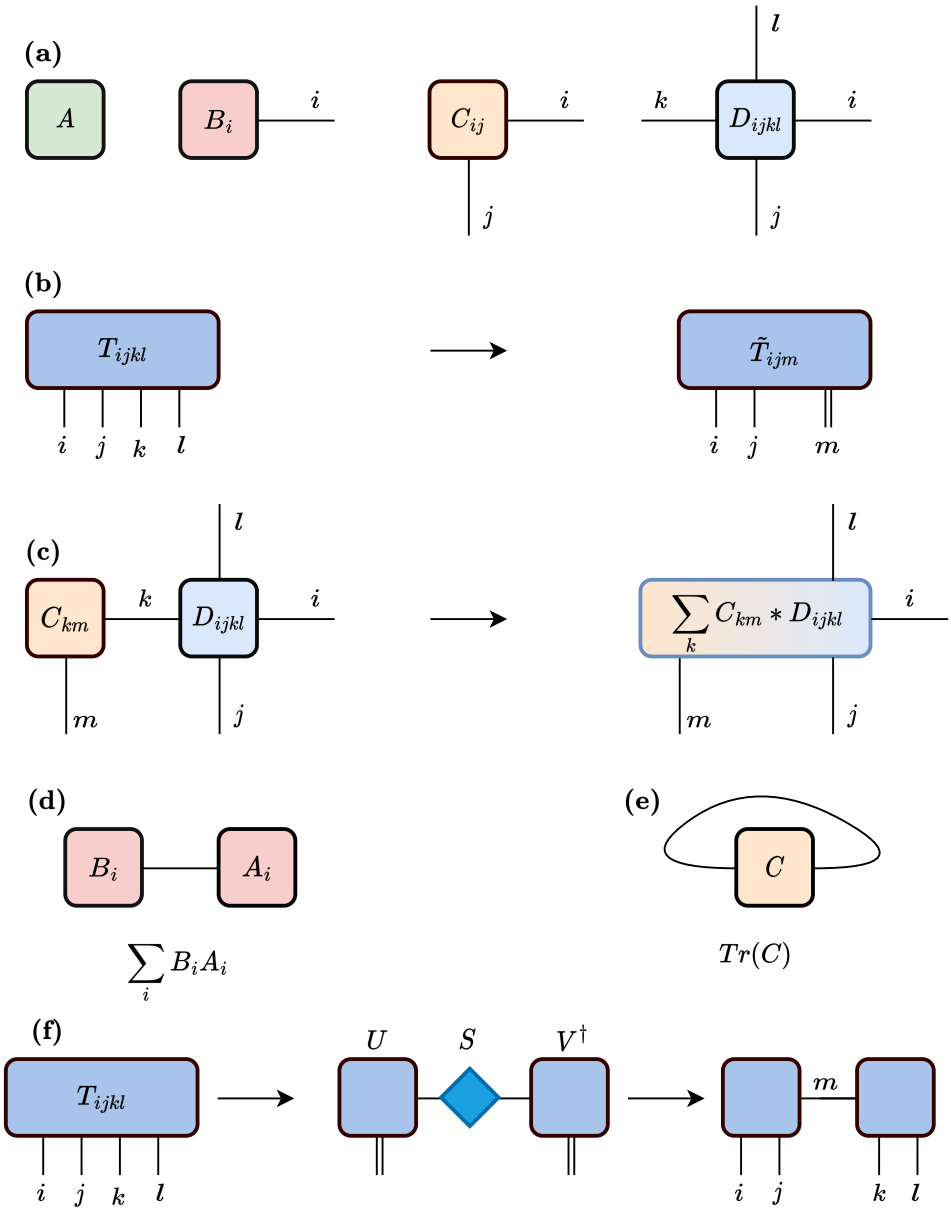

FIGURE A.1: **Basic tensor operations** (a) In order from left to right, a scalar A, a vector B_i, a matrix C_{ij} and a rank-4 tensor D_{ijkl}. The legs emerging out of the figures indicate the indices of the tensors. (b) Reshaping a tensor T_{ijkl} by merging two indices k, l into a new index m. (c) Tensor contraction of a matrix C and a tensor D. The resultant tensor CD is given by $\sum_k C_{km} D_{ijkl}$. (d) The scalar product of two vectors is represented by joining the legs of the vectors. The resultant product has no open legs. (e) The trace of a matrix is represented by joining the legs that represent the two indices. (f) A tensor decomposition involves reshaping the tensor into a matrix and then performing an SVD. The resultant diagonal matrix S can be absorbed into the tensors, leaving us with two tensors that can be contracted to give us the original tensor.

$$\sum_k A_{i_1 i_2 k} B_{j_1 j_2 k} = [AB]_{i_1 i_2 j_1 j_2} \tag{A.1}$$

Diagrammatically, this is shown by joining two legs as shown in figure A.1-(c) .

• *Tensor decomposition*: A tensor decomposition is a generalization of matrix decomposition. By reshaping any tensor into a matrix, one can use traditional factorization techniques such as singular value decomposition (SVD), Eigenvalue decomposition (EVD), or QR decompositions to write a given matrix as a product of two or more matrices. Once decomposed, the indices that were reshaped earlier can be restored to their original form.

One can also use SVD to approximate a tensor. The SVD of a matrix M is defined as the product of a unitary matrix U, a diagonal matrix with positive values S and another unitary matrix $V^\dagger$, i.e.,

$$M = USV^\dagger \tag{A.2}$$

The diagonal entries of the matrix S are called the singular values of M. The sum of squares of the singular values is the 2-norm of the matrix M.

$$\begin{aligned} ||M|| &= \sqrt{\sum_{i,j} |m_{ij}|^2} = \sqrt{\sum (m_{ij} m^*{}_{ji})} = \sqrt{\mathrm{Tr}(MM^\dagger)} \\ &= \sqrt{\mathrm{Tr}(US^2U^\dagger)} = \sqrt{\mathrm{Tr}(S^2)} \end{aligned} \tag{A.3}$$

If one were to approximate a matrix M_{ij} as a product of two matrices of X and Y, for some $n < p$, such that the resultant matrix minimizes the 2-norm, the best way is to use an SVD and keeping the n largest singular values.[145] Let $\tilde{M} = XY$ be a low-rank approximation of M whose singular values are $\tilde{S}$. Let matrices M and $\tilde{M}$ be reshaped as column vectors m_i and $\tilde{m}_i$.

$$\begin{aligned} ||M - \tilde{M}||^2 &= \mathrm{Tr}((M - \tilde{M})(M - \tilde{M})^\dagger) \\ &= ||M||^2 + ||\tilde{M}||^2 - 2||M\tilde{M}^\dagger|| \\ &= \sum_i {S_{ii}}^2 + \sum_j \tilde{S}^2_{jj} - 2||M||||\tilde{M}||(\sum_i m_i \cdot \tilde{m}_i) \\ &= \sum_{i<=n} (S^2_{ii} + \tilde{S}^2_{ii} - S_{ii}\tilde{S}_{ii} cos(\theta_i)) + (\sum_{i>n} S^2_{ii}) \\ &\geq \sum_i |S_{ii} - \tilde{S}_{ii}|^2 + (\sum_{i>n} S^2_{ii}) \qquad \text{(A.4)} \\ &\geq (\sum_{i>n} S^2_{ii}) \qquad \text{(A.5)} \end{aligned}$$

The minimum of the equation A.5 occurs when the remaining discarded singular values are the smallest singular values of M. The $\cos(\theta)_i$ term is given by $(u_i \cdot \tilde{u}_i)(v_i \cdot \tilde{v}_i)$. The maximum of equation A.4 occurs when the unitary vectors of both matrices are identical. Hence, the best low-rank approximation is given by a matrix

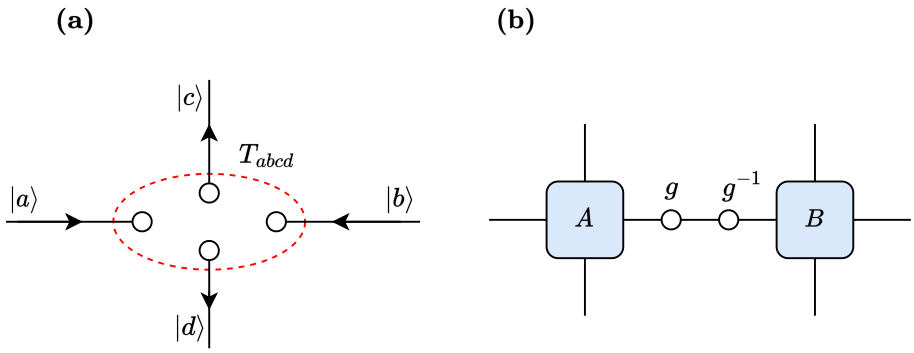

FIGURE A.2: (a) Representation of a tensor as a linear map from the input vector spaces (marked by incoming arrows) and output vector spaces (marked by outgoing arrows). (b) The bond matrices of two virtual spaces cancel out when contracted. When absorbed into the neighboring tensors, these matrices change the individual entries of the tensors while keeping the overall contraction invariant.

that is made of the largest d_n singular values and the corresponding singular vectors. The norm of the difference is given by the square root of the sum of squares of the remaining discarded singular values $\sqrt{(\sum_{i>n} S_{ii})}$.

Hence $X = U\sqrt{S}P_n$ and $Y = P_n^T\sqrt{S}V$ where S is the diagonal matrix with singular values arranged in descending order $S_{11} \geq S_{22} \geq \cdots \geq S_p$ and P_n is the projector matrix of dimensions $p \times n$ which is a diagonal matrix with diagonal entries equal to 1. Using this we can truncate the new index m, as shown in figure A.1-(f).

Just as a larger tensor can be decomposed into a contraction of smaller tensors, one can use a network of smaller tensors to define a larger tensor. The indices in a tensor network that are contracted are called the *virtual indices*, whereas the ones that remain uncontracted are called *real indices*. We should also note that a tensor network is not unique, as one can always change the basis of a tensor by inserting a pair of isometries $\mathcal{I} = gg^{-1}$ on a virtual index which can alter the individual tensors while keeping the global wavefunction invariant as shown in figure A.2-(b). Thus a gauge matrix can transform the vector space of the virtual legs without affecting the final tensor network. This gauge degree of freedom is an important constraint that can hamper the implementation of certain numerical schemes. For example, the gauge transformation can change the numerical values of a tensor. Hence, an SVD truncation of two tensors that are connected through a gauge transformation might not have the same singular values, which affects the overall truncation. This makes it extremely important to identify the right gauge transformation of a tensor before we use the tensor in other schemes.

Tensors as linear maps

A tensor can be considered as a linear map between vector spaces in the following way. Every index of a tensor can be used as a label of a basis $|i\rangle$ of a complex vector

space $V^{[i]} \in \mathbb{C}^{d_i}$ of dimension d_i. Given a tensor T of rank p, we can classify the indices $i_1, i_2, \ldots, i_p$ into either 'incoming' or 'outgoing' indices. In general, for a local tensor, all the virtual indices that are to be contracted over can be considered the incoming indices while the physical indices can be classified as outgoing indices. A tensor can be then considered as a linear mapping from a vector space of incoming indices $\mathcal{V}^{[in]}$ to a vector space of outgoing indices $\mathcal{V}^{[in]}$.

$$\begin{aligned} V^{[in]} &= \bigotimes_{m \in I} v^{[i_m]}. \\ V^{[out]} &= \bigotimes_{n \in O} v^{[i_n]} \end{aligned}$$

For example, if a rank-4 tensor T_{abcd} has two incoming indices $a, b \in I$ and two outgoing indices $c, d \in O$, then it defines a linear map $T : V^{[a]} \otimes V^{[b]} \rightarrow V^{[c]} \otimes V^{[d]}$, defined as,

$$T = \sum_{a,b,c,d} t_{abcd} \, |c\rangle \, |d\rangle \, \langle a| \, \langle b| \tag{A.6}$$

The contraction of two tensors over a given virtual space is then defined as placing a "bond operator" that maximally entangles the corresponding virtual spaces. Diagrammatically, this is shown as A.2-(a). Describing the tensor as a linear map helps us to enforce certain internal symmetries through the vector spaces. For an SU(2) symmetric tensor, one can easily define the vector spaces that go in and out as a direct sum of irreducible representations (irreps). Since we can always transform the individual vector spaces such that the contraction through the bond operator stays invariant, this linear map formulation also suffers from the same gauge freedom. We can overcome this by fixing the canonical basis of the vector space at the time of defining the tensor.

Appendix B

Résumé en français

B.1 Introduction to quantum spin liquids

Pour bien comprendre les bases des systèmes de spin quantiques, il faut commencer par les propriétés fondamentales des électrons. Nous allons commencer par le modèle d'une collection d'électrons se déplaçant dans un matériau à l'état solide.

L'hamiltonien général de ce modèle contient un terme d'énergie cinétique qui prend en charge le mouvement des électrons et un terme d'énergie potentielle qui inclut l'interaction des électrons avec le réseau solide et l'interaction des électrons entre eux.

$$\mathcal{H} = \frac{-\hbar^2}{2m_e}\nabla^2 + U_{\text{ion}}(\mathbf{r}) + \sum_{i\neq j}\frac{e^2}{|\mathbf{r}_i - \mathbf{r}_j|}. \tag{B.1}$$

En supposant un cristal parfait, en ignorant les interactions électron-phonon et d'autres effets dynamiques, cela peut être réduit à,

$$\mathcal{H} = \sum_{ij\sigma} t_{ij} c^\dagger_{i\sigma} c_{j\sigma} + U \sum_{\sigma'} c^\dagger_{i\sigma} c^\dagger_{i\sigma'} c_{i\sigma'}, \tag{B.2}$$

où le terme cinétique,

$$t_{ij} = \langle i| \left[-\frac{\hbar^2}{2m_e}\nabla^2 + U_{\text{ion}}\right] |j\rangle$$

est appelé le terme de "saut", dont l'action se traduit par le saut de l'électron du site i au site j. $c^\dagger_{i\sigma}$ est l'opérateur de création d'électron au site i et de spin σ en base de wannier. En utilisant le principe d'exclusion de Pauli et l'opérateur de nombre de particules, nous pouvons réécrire ceci comme le célèbre Hamiltonien de Hubbard,

$$\mathcal{H} = \sum_{i,j,\sigma} t_{ij} c^\dagger_{i\sigma} c_{j\sigma} + U \sum_i n_{i\uparrow} n_{i\downarrow},$$

où $n_{i\sigma} = c^\dagger_{i\sigma} c_{i\sigma}$. Dans la limite de l'isolant $U \gg |t_{ij}|$, à exactement la moitié du remplissage (un électron par site), l'hamiltonien de Hubbard se réduit à l'hamiltonien de Heisenberg qui, en termes d'opérateurs de spin, peut s'écrire,

$$\mathcal{H} = \sum_{\langle i,j\rangle} J_{ij} \mathbf{S_i} \cdot \mathbf{S_j}, \tag{B.4}$$

où S est l'opérateur de spin de l'électron de saut et $J_{ij} = \frac{4|t_{ij}|^2}{U} > 0$ est le terme d'interaction. Cet hamiltonien, appelé hamiltonien de Heisenberg, peut être réécrit en termes d'opérateurs de spin,

$$\mathcal{H} = \sum_{ij} J_{ij} \left(\frac{1}{2}(S^+_i S^-_j + S^-_i S^+_j) + S^z_i S^z_j\right). \tag{B.5}$$

Pour un système simple de deux particules de spin-$\frac{1}{2}$, cet hamiltonien a quatre états propres avec deux valeurs propres distinctes. Les états propres correspondant à l'énergie la plus élevée valeur de $0.5J$ ont une triple dégénérescence et forment le triplet de spin. L'état propre correspondant à la valeur d'énergie inférieure de $-0.5J$ est appelé un singulet. L'orthogonale les états propres correspondant à ces valeurs propres dans la base S_z sont :

$$|S_{\text{triplet}}\rangle = \begin{cases} |\downarrow\rangle\,|\downarrow\rangle \\ \frac{1}{\sqrt{2}}(|\uparrow\rangle\,|\downarrow\rangle + |\downarrow\rangle\,|\uparrow\rangle) \\ |\uparrow\rangle\,|\uparrow\rangle \end{cases}$$

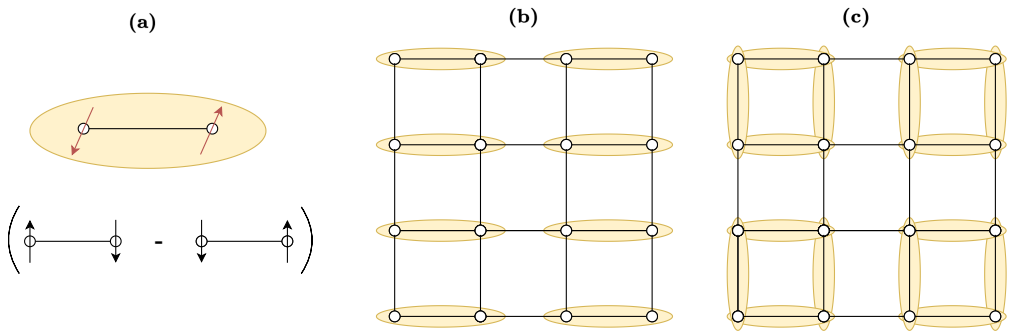

FIGURE B.1: (a) Une représentation visuelle du singulet de spin $\frac{1}{\sqrt{2}}(|\uparrow\rangle|\downarrow\rangle - |\downarrow\rangle|\uparrow\rangle)$ qui sera utilisé dans le reste de la thèse. (b) & (c) Un état colonnaire et un état plaquette - deux configurations distinctes de cristal de liaison de valence (VBC) constituées de singulets de spin disposés périodiquement. Les VBC ne brisent pas la symétrie SU (2) mais brisent la symétrie translationnelle du réseau.

$$|S_{\text{singlet}}\rangle = \frac{1}{\sqrt{2}}(|\uparrow\rangle|\downarrow\rangle - |\downarrow\rangle|\uparrow\rangle)$$

Notez que les deux états sont SU(2) symétriques. Une physique intéressante émerge lorsque nous avons des états entièrement constitués de singulets. Un tel ensemble d'états est appelé cristaux de liaison de valence (VBC) qui ont des singulets disposés périodiquement comme le montre la figure B.1. De tels états brisent la symétrie translationnelle mais ont une symétrie SU(2). Nous pouvons restaurer cette symétrie de translation brisée en considérant une superposition de plusieurs de ces états. L'état résultant aurait un enchevêtrement à longue portée mais pas d'ordre à longue portée ou de symétries brisées. Ces états sont appelés liquides de spin quantique (QSL)

L'un des ingrédients clés d'un système de spin pour réaliser un tel état est la frustration magnétique. Un système magnétique est dit frustré s'il possède des interactions concurrentes qui ne peuvent pas être satisfaites simultanément. En conséquence, les états fondamentaux des aimants frustrés présentent souvent des dégénérescences extrêmes qui ne se traduisent pas par un état ordonné même à une température nulle absolue. Par exemple, l'état fondamental d'un système à trois particules disposé sur un réseau triangulaire a un état fondamental qui est la superposition de trois configurations de liaison de valence, comme indiqué sur la figure B.2-(a).

Ces liquides de spin peuvent être classés en deux catégories en fonction de la différence d'énergie entre l'état fondamental et le premier état excité dans la limite thermodynamique. Les liquides de spin dont l'hamiltonien a un écart d'énergie fini sont appelés liquides de spin à écart et ceux qui ont un écart d'énergie nul dans la limite thermodynamique sont appelés liquides de spin sans écart. Les liquides de spin avec espacement ont des corrélations décroissantes de manière exponentielle, tandis que les liquides de spin sans espacement ont des corrélations décroissantes algébriquement.

De plus, ces liquides de spin sont connus pour obéir à la loi dite des aires. On dit d'un

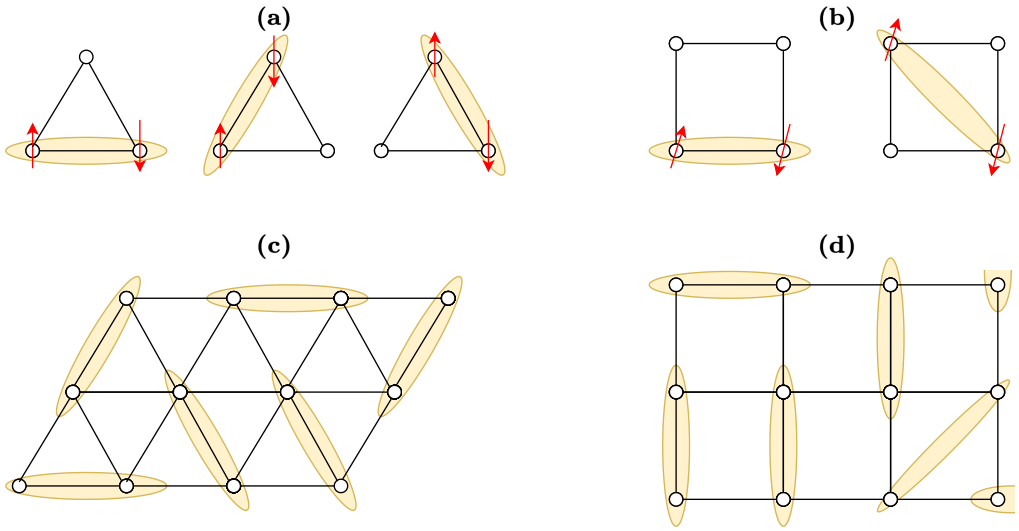

FIGURE B.2: Frustration magnétique. (a) États propres de spin dans une cellule unitaire triangulaire. Chaque configuration minimise l'énergie le long de la liaison singulet mais laisse les deux autres liaisons insatisfaites. (b) Frustration dans une cellule unitaire de réseau carré. La frustration est due à la compétition entre les maillots le long du bord du carré et les maillots le long de la diagonale. (c) Une configuration de liaison de valence aléatoire (VB) dans un réseau triangulaire. (d) Une configuration de liaison de valence aléatoire dans un réseau carré. Les liquides de spin quantique peuvent être construits par une superposition linéaire de plusieurs configurations VB de sorte qu'aucune symétrie n'est brisée.

état de mécanique quantique qu'il obéit à la loi des aires s'il satisfait à la condition suivante. *Si un système de particules peut être décomposé en deux sous-systèmes complémentaires A et B, alors la limite supérieure de l'entropie d'intrication est proportionnelle au nombre de particules à la frontière du sous-système A, c'est-à-dire que* $S_A = O(|\partial A|)$.

L'identification des liquides de spin quantiques dans les matériaux naturels est assez difficile en raison de leur manque général d'ordre dans l'état fondamental. À l'heure actuelle, plusieurs matériaux candidats possibles qui présentent certaines signatures confirmées de liquides de spin, tels que la $ZnCu_3(OH)_6Cl_2$(Herbertsmithite), la $(Cu_3V_2O_7(OH)_2 - 2H_2O)$ (Volborthite) et la Vesignieite $(BaCu_3V_2O_8(OH)_2)$ existent.

Réseau optique et simulateurs quantiques

L'une des techniques expérimentales clés de ces simulateurs d'atomes froids est la création d'un réseau optique d'atomes froids. Elle consiste généralement à désaccorder une lumière laser de telle sorte qu'elle soit éloignée de la longueur d'onde de résonance des atomes. En conséquence, les atomes n'absorbent pas les photons et ne subissent donc pas de chauffage. Lorsque deux lasers se propageant en sens inverse se combinent pour former une onde stationnaire périodique, le potentiel électrique qui en résulte agit comme un treillis. Lorsque ce réseau optique est peuplé d'atomes,

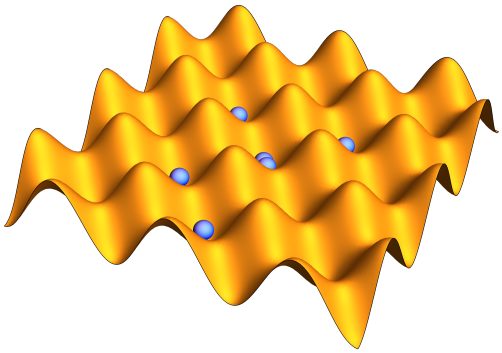

FIGURE B.3: Réseau optique dans une configuration de simulateur atomique ultra-froid. Le réseau est construit à partir d'ondes stationnaires formées par six sources laser en 3 dimensions. A des températures extrêmement basses (de l'ordre de nK), les gaz atomiques occupent les creux du réseau optique. L'intensité du laser contrôle la quantité de tunnel qui peut avoir lieu à travers la barrière de potentiel électrique et peut ainsi être utilisée pour contrôler la quantité de sauts entre divers sites de réseau.

à des températures suffisamment basses, les atomes sont confinés dans les minima du potentiel électrique périodique, comme le montre la figure B.3. Le comportement des atomes confinés dans un tel potentiel est similaire à celui des électrons dans un solide cristallin. La profondeur du potentiel électrique peut être accordée en modifiant l'intensité du laser, ce qui nous permet de contrôler le mouvement dynamique des atomes qui sautent d'un minima à l'autre par effet tunnel quantique. Lorsque le potentiel est élevé, l'effet tunnel est à son minimum, et le système se comporte comme un isolant et peut être utilisé pour simuler les isolants de Mott.

Un simulateur d'atomes de Rydberg est l'un de ces simulateurs d'atomes froids qui utilise le concept de blocus de Rydberg. L'idée clé du blocage de Rydberg est le concept de blocage dipolaire [70–73]. Si nous braquons un laser sur un atome individuel avec la bonne fréquence ω_0, nous pouvons faire passer un électron de l'état fondamental $|g\rangle$ à un état excité $|r\rangle$. Cela crée une paire d'électrons intriqués dans l'état fondamental et excité. L'excitation d'un atome de Rydberg déplace le niveau d'énergie des atomes de Rydberg restants de $V(R)$. Tous les atomes qui se trouvent dans un certain rayon de blocage, R_b , ont leurs niveaux d'énergie suffisamment décalés pour les faire sortir de la résonance de la fréquence laser. Ainsi, l'excitation d'un atome de Rydberg bloque l'excitation des atomes à proximité comme le montre la figure B.4.

Motivation

La plupart des modèles théoriques utilisés pour décrire les matériaux magnétiques réels, y compris ceux décrits précédemment dans la thèse, sont trop idéaux pour être précis. Les atomes ultra-froids dans les réseaux optiques, cependant, fournissent un terrain de jeu presque parfait pour la réalisation de ces systèmes. Puisque ces états sont complètement contrôlés par les puits de potentiel artificiels, nous pouvons changer brusquement le hamiltonien d'interaction plus rapidement que l'échelle de temps de la dynamique de relaxation du système. Après un tel changement quasi instantané de

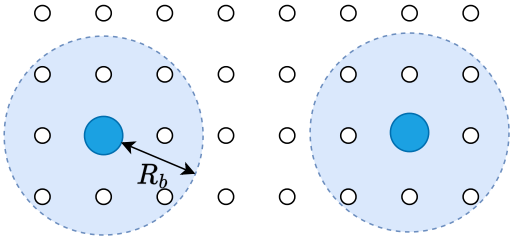

FIGURE B.4: Un arrangement de blocus typique de Rydberg avec le rayon de blocus R_b marqué. Tous les atomes de Rydberg dans R_b ne peuvent pas être excités. L'atome excité peut être considéré comme un singulet intriqué et la condition que le R_b couvre deux points de réseau peut être utilisée pour appliquer la condition d'un dimère par site de réseau.

l'hamiltonien, appelé quench hamiltonien, les valeurs d'espérance des observables locales génériques O deviennent dépendantes du temps. Parmi ces travaux fascinants, celui qui nous semble le plus intéressant par rapport au contenu de cette thèse est un protocole récemment proposé pour optimiser la préparation de liquides de spin topologiques sur des atomes de Rydberg par Giudici *et al.*[1] pour réaliser l'état RVB sur le réseau de Kagome (basé sur la réalisation expérimentale des travaux de G. Semeghini *et al.*[2]). Le protocole proposé vise la préparation du point fixe de l'état de phase topologique (RVB) des dimères durs. L'ansatz proposé pour étudier la dynamique de cet état est donné par un ansatz de réseau tensoriel variationnel à deux paramètres,

$$|\phi(z_1, z)2)\rangle = \mathcal{N}\mathcal{P}[\bigotimes_{i=1}^{N}(1 + z_2\sigma_+^i)(1 + z_1\sigma_-^i)]\,|\mathrm{RVB}\rangle\,, \tag{B.6}$$

pour $z_1, z_2 \in \mathbb{C}$, où $\mathcal{N}$ est une constante de normalisation, $\mathcal{P}$ est le projecteur sur le secteur de l'espace de Hilbert qui satisfait la contrainte de blocage et $\sigma_-^i = |g_i\rangle\langle r_i|$ et $\sigma_+^i = |r_i\rangle\langle g_i|$. Pour des valeurs finies de z_1 et z_2, cet ansatz couvre une phase de RVB avec des excitations de spinon. Des descriptions similaires de réseaux tensoriels basés sur PEPS pour les états de l'atome de Rydberg ont également été suggérées dans d'autres travaux.

Avec l'intérêt croissant pour l'utilisation de l'ansatz PEPS pour étudier la dynamique de la trempe, il serait intéressant de poser certaines questions auxquelles l'ansatz PEPS peut répondre. Le système se thermalise-t-il et s'équilibre-t-il jusqu'à un certain état final ? Conserve-t-il l'information de l'état initial ? Le quench lève-t-il la dégénérescence locale ? Les symétries internes survivent-elles ? Afin de guider les stratégies expérimentales pour répondre à ces questions, il doit y avoir des prédictions théoriques pour ces questions. En outre, les résultats de ces expériences doivent être vérifiés avant de pouvoir être utilisés de manière fiable dans la pratique. Actuellement, des techniques numériques efficaces pour étudier la dynamique de la trempe existent dans des systèmes unidimensionnels sous la forme de tDMRG et MPS, mais le

[1] Phys. Rev. Lett.129 (2022), p. 090401.
[2] Science 374.6572 (2021), pp. 1242–1247.

calcul de la dynamique de non-équilibre qui suit un quench quantique est une tâche fastidieuse dans les systèmes de spins quantiques bidimensionnels. Jusqu'à présent, à l'exception de quelques modèles intégrables à quelques corps, aucune technique numérique fiable n'existe pour les systèmes bidimensionnels. Ainsi, le but de cette thèse est de construire des outils numériques pour simuler la dynamique de trempe d'un système fermé d'états purs à température zéro en utilisant le cadre des réseaux tensoriels. Ces outils seront ensuite utilisés pour étudier la dynamique de quench de l'état pur-RVB, qui est dit avoir des corrélations dimères-dimères critiques. Bien que l'accent soit mis sur la dynamique de l'état RVB sur le réseau carré, les outils présentés dans la thèse pourraient être généralisés à d'autres réseaux bidimensionnels.

B.2 Méthodes de réseau tenseur

Cette section résume les travaux des chapitres deux et trois.

Introduction

L'un des principaux obstacles à l'étude de la physique des systèmes quantiques à plusieurs corps à l'aide de méthodes numériques est la croissance exponentielle de l'espace de Hilbert du système avec le nombre de particules. Afin de contourner ce problème, il faut utiliser des techniques d'approximation pour rendre l'étude de ces systèmes quantiques à plusieurs corps réalisable. Bien que toute approximation nous empêche d'accéder à l'intégralité de l'espace de Hilbert possible, une bonne approximation couvre toujours la partie de l'espace de Hilbert qui est la plus pertinente pour un problème donné. Dans le cas des états fondamentaux des hamiltoniens avec ou sans espace en 1-D, la partie pertinente de l'espace de Hilbert est l'ensemble des états qui suivent la "loi de l'espace".

La fonction d'onde générale décrivant un système de N particules sur une chaîne est donnée par

$$|\psi\rangle = \sum_{i_1} \dots \sum_{i_N} C_{i_1 i_2 \dots i_N} |i_1 i_2 \dots . i_N\rangle .$$

Pour un ensemble donné de bases locales $|i_1\rangle |i_2\rangle \dots . |1_{N-1}\rangle |i_N\rangle$, toute l'information relative à la fonction d'onde est présente dans les coefficients de $C_{i_1 i_2 \dots i_N}$, ce qui devient extrêmement difficile à décrire numériquement car l'espace de Hilbert croît exponentiellement avec le nombre de particules. Une façon de gérer ce problème consiste à utiliser la décomposition de Schmidt pour réduire le coefficient massif en une simple contraction de tenseurs de rang 3.

Considérons une partition d'un système en deux sous-systèmes A et B dont les espaces de Hilbert sont de dimensions d_A et d_B. La décomposition de Schmidt de cette partition est donnée par,

$$|\psi_{AB}\rangle = \sum_i \lambda_i |\phi_i^A\rangle |\phi_i^B\rangle . \tag{B.7}$$

Cela équivaut à décomposer un tenseur $|\psi\rangle$ en 2 tenseurs composants à bases orthonormées, reliés par un indice auxiliaire i. La dimension de l'indice auxiliaire i

est le rang de Schmidt qui nous donne des informations concernant l'intrication entre les deux sous-systèmes A et B. Si les systèmes sont complètement indépendants avec une intrication nulle, la taille de l'indice auxiliaire serait de 1 et le système peut être réécrit comme un état produit. On peut également utiliser le tenseur des coefficients pour effectuer la même décomposition. En considérant le tenseur des coefficients comme un vecteur à n dimensions, nous pouvons le remodeler en une matrice de taille $(d_A \times d_B)$. En utilisant SVD, on peut effectuer une décomposition exacte ou approximative, en créant un nouvel indice D. Nous pouvons répéter ce processus de décomposition tensorielle pour obtenir un ensemble de tenseurs de rang 3 appelé l'état de produit matriciel (MPS).

$$C_{i_1 i_2 \ldots i_N} = \lambda_{12}\lambda_{23}\ldots\lambda_{(N-1)N} = \sum_{a_1 a_2 \ldots a_{N-1}} M^{i_1}_{a_1} M^{i_2}_{a_1 a_2} \ldots M^{i_{N-1}}_{a_{N-2} a_{N-1}} M^{i_N}_{a_{N-1}}$$

$$|\psi\rangle = \sum_{i_1 \ldots i_N} \sum_{a_1 a_2 \ldots a_{N-1}} M^{i_1}_{a_1} M^{i_2}_{a_1 a_2} \ldots M^{i_{N-1}}_{a_{N-2} a_{N-1}} M^{i_N}_{a_{N-1}} \tag{B.8}$$

Nous pouvons étendre le même argument aux opérateurs et obtenir une décomposition tensorielle appelée opérateur de produit de matrice (MPO). La notation diagrammatique de ce dernier est illustrée dans la figure B.5. Un MPS typique se compose de tenseurs de rang 3 avec un indice physique d et deux indices virtuels de dimension de liaison D. La taille de la liaison virtuelle D contrôle la précision de MPS et MPO. Pour une dimension D suffisamment grande, on peut couvrir une plus grande partie de l'espace de Hilbert et approximer une fonction d'onde donnée avec une meilleure précision. Si l'on devait construire une matrice de densité réduite à partir d'une MPS, la matrice résultante aurait toujours une forme de $(D \times D)$. Cela implique que l'entropie d'intrication, qui est maximale lorsque le spectre de la matrice de densité réduite est uniforme, a une limite supérieure $S \leq \ln(D)$. Ainsi, la quantité maximale d'entropie d'intrication est donnée par $\mathcal{S}_{max} = \ln(D)$. Puisque la longueur de frontière $|\partial A|$ d'un système 1D est une constante, les états de produit matriciel obéissent naturellement à la loi d'aire. De plus, les tenseurs de rang 3 peuvent être utilisés pour renforcer les symétries spatiales du tenseur. Afin de construire une chaîne de spin invariante par translation, on peut utiliser le même tenseur de rang 3 à chaque site. À partir de maintenant, sauf indication contraire, nous ne traiterons que des tenseurs invariants en translation.

États de paires intriquées projetées

Le concept de PEPS est une généralisation du MPS en deux dimensions. Un tenseur PEPS typique consiste en un indice physique de dimension d et un ensemble d'indices virtuels de dimension D comme le montre la figure B.6. Le nombre d'indices virtuels est idéalement pris égal au nombre de coordination z du treillis. Pour un réseau carré, nous utilisons un tenseur de rang 5 avec quatre indices virtuels et un indice physique. Diagrammatiquement, nous préférons utiliser une ligne courbe pour représenter l'indice physique et le distinguer des indices virtuels qui sont représentés par des lignes droites. On peut construire une fonction d'onde donnée à partir d'un tenseur PEPS en contractant les indices virtuels avec les indices virtuels des tenseurs PEPS voisins, comme le montre la figure B.6. Un réseau de tenseurs

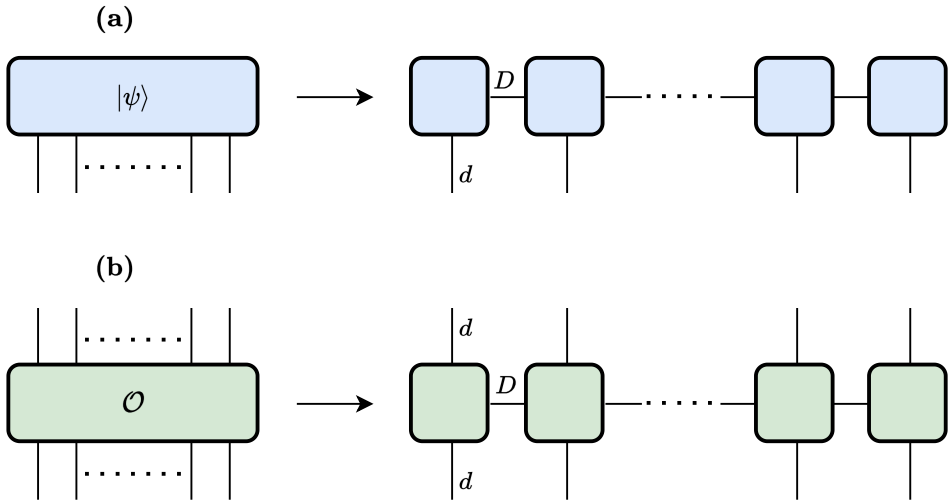

FIGURE B.5: (a) La décomposition tensorielle d'une fonction d'onde 1D. L'ensemble de la fonction d'onde invariante par translation peut être représenté par un ensemble de tenseurs de rang 3 et deux tenseurs limites de rang 2. La dimension des indices virtuels D fixe la limite de l'entanglement entropique que le MPS peut capturer. (b) La décomposition tensorielle d'un opérateur matrice-produit (MPO).

PEPS obéit par construction à la loi des aires. Pour toute aire donnée, le nombre d'indices virtuels ouverts qui coupent la frontière croît linéairement avec la longueur de la frontière, comme le montre la figure B.7-(c). Puisque chaque indice virtuel ouvert contient une intrication maximale de $\ln(D)$, l'intrication maximale entre une région compacte et le reste du réseau s'échelonne linéairement avec la longueur de la frontière. Naturellement, les symétries spatiales de la fonction d'onde se reflètent dans les symétries spatiales du tenseur PEPS. Pour que le système soit invariant en translation et en rotation, le tenseur PEPS doit être invariant sous l'action de la symétrie du groupe ponctuel C_{4v}. Les opérations de base du groupe de symétrie ponctuelle C_{4v} sont représentées schématiquement sur la figure B.7-(a). Dans la suite de la thèse, nous ne traiterons que des tenseurs SU(2) symétriques C_{4v} invariants par translation, sauf indication contraire.

La construction des PEPS symétriques SU(2) est similaire à la construction de l'état AKLT en 1D.

Mise à jour simple

Une fois que nous avons réduit l'opérateur d'évolution temporelle globale à un PEPO à site unique, nous pouvons l'appliquer à l'espace physique du tenseur pour le mettre à jour. Puisque chaque opérateur PEPO d'étape de Trotter augmente la dimension de liaison virtuelle par un facteur de d^2, on s'attend à ce que la dimension de liaison du tenseur croisse exponentiellement avec le nombre d'étapes de Trotter. Ainsi, un schéma d'approximation est nécessaire pour contrôler la dimension de liaison après chaque étape puisque $U(\tau) = \mathcal{G}_a\mathcal{G}_b\mathcal{G}_c\mathcal{G}_d$, chaque étape de la mise à jour peut être

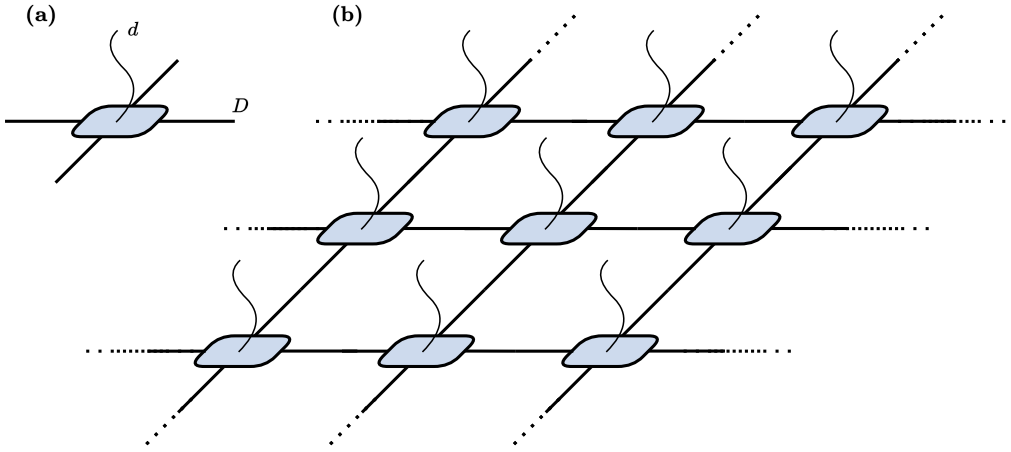

FIGURE B.6: (a) Un tenseur PEPS à réseau carré typique avec un indice physique représenté par une ligne courbe et quatre indices virtuels représentés par des lignes droites. (b) La contraction de plusieurs tenseurs PEPS pour donner une fonction d'onde. En utilisant des tenseurs identiques sur chaque site, nous pouvons incorporer la symétrie translationnelle dans la fonction d'onde.

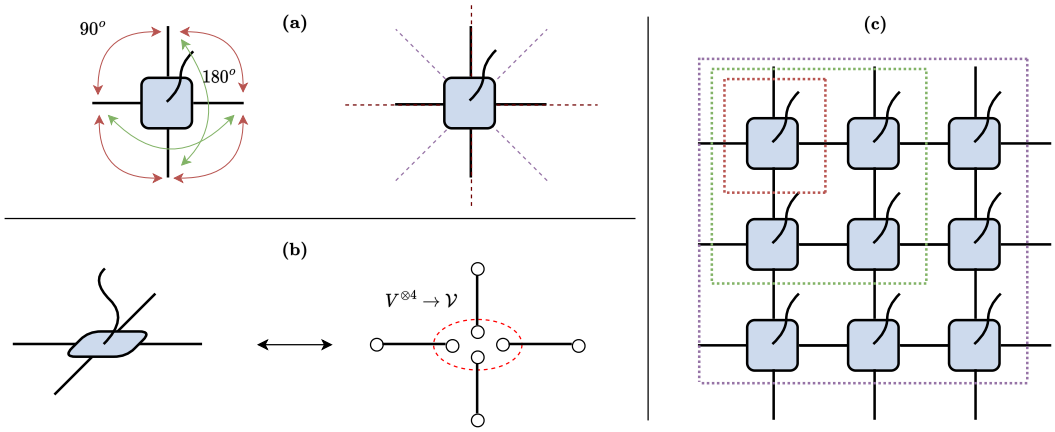

FIGURE B.7: Bases du tenseur PEPS sur un treillis carré (a) Opérations de symétrie du groupe de points C_{4v}. Un tenseur PEPS symétrique C_{4v} possède une symétrie de rotation de 90^o (indiquée en rouge) et une symétrie de rotation de 180^o (indiquée en vert) autour du centre du tenseur. Le tenseur a également une symétrie de réflexion autour de l'axe des X, de l'axe des Y et de deux axes XY qui font un angle de 45^o avec X et Y (indiqués en pointillés). (b) Tenseur PEPS sous forme de carte linéaire. (c) Loi d'aire d'un réseau de tenseurs PEPS. L'intrication maximale capturée par le réseau tensoriel est égale au nombre de liaisons virtuelles traversant la frontière multiplié par l'intrication maximale par liaison (donnée par $\ln(D)$). Le nombre de liaisons est proportionnel au périmètre de la frontière, donc la loi de l'aire est toujours satisfaite.

divisée en quatre sous-étapes où l'approximation est effectuée après l'application de la porte individuelle $\mathcal{G}_k$.

Un schéma d'approximation après application d'une porte $\mathcal{G}_k$ à une onde $|\psi\rangle$ est une procédure consistant à trouver une fonction d'onde $|\phi\rangle$ telle qu'elle minimise la distance $\||\phi\rangle - \mathcal{G}_k |\psi\rangle\|$. La différence entre les divers schémas d'approximation dépend de la manière dont la distance est calculée.

La plus simple de ces approximations est le schéma de mise à jour simple où la distance est minimisée à un niveau tensoriel local. Étant donné que la fonction d'onde est paramétrée par le tenseur PEPS local, la mise à jour simple réduit le problème de la mise à jour de la fonction d'onde à la mise à jour du tenseur PEPS local. Le schéma de mise à jour simple a été introduit pour la première fois par Jiang et a été largement utilisé depuis lors. À chaque étape de la mise à jour simple, nous appliquons la porte $\mathcal{G}_k$ qui agit sur deux sites, obtenons un tenseur à deux sites, puis tronquons la liaison élargie en utilisant la décomposition en valeurs singulières. Comme nous ne nous intéressons qu'aux réseaux tensoriels symétriques invariants par translation de C_{4v}, la SVD doit être symétrique. Avant de discuter des détails du schéma de mise à jour simple, nous allons d'abord discuter des détails de la forme symétrique de la décomposition en valeur singulière appelée décomposition d'Autonne-Takagi utilisée dans ce travail.

La décomposition d'Autonne-Takagi est une façon de factoriser une matrice symétrique en un produit de deux matrices qui sont transposées l'une de l'autre. Pour une matrice symétrique complexe A, elle est définie comme suit :

$$A = USU^T, \tag{B.9}$$

où S est une matrice diagonale contenant les valeurs singulières de la matrice A et U est un unitaire complexe.

Algorithme SU

Nous allons maintenant passer en revue l'algorithme SU pour un hamiltonien deux sites à plus proche voisin.

Pour le simple hamiltonien de Heisenberg antiferromagnétique à plus proche voisin, l'étape de Trotter est définie comme l'application des quatre portes telles. L'application du tenseur à deux sites donne un tenseur de rang 8 comme le montre la figure B.8-(c), qui peut être remodelé en une matrice de dimensions $dD^3 \times dD^3$. L'approximation à faible rang de la matrice de mise à jour simple résultante peut être trouvée en effectuant une décomposition en valeurs singulières. Afin de réduire le coût de calcul, nous pouvons séparer la liaison active à laquelle la porte $\mathcal{G}_k$ est appliquée, comme le montre la figure B.8. Ensuite, la matrice de mise à jour simple est réduite à une matrice de dimension $dD \times dD$. Si le tenseur initial à un site est C_{4v} symétrique et que la porte à deux sites $\mathcal{G}_k$ est symétrique, nous pouvons utiliser la décomposition d'Autonne-Takagi. La procédure est ensuite répétée sur les quatre liaisons pour terminer l'étape de mise à jour simple. Le schéma de mise à jour simple peut donc être résumé dans la figure B.8 et contient les étapes suivantes :

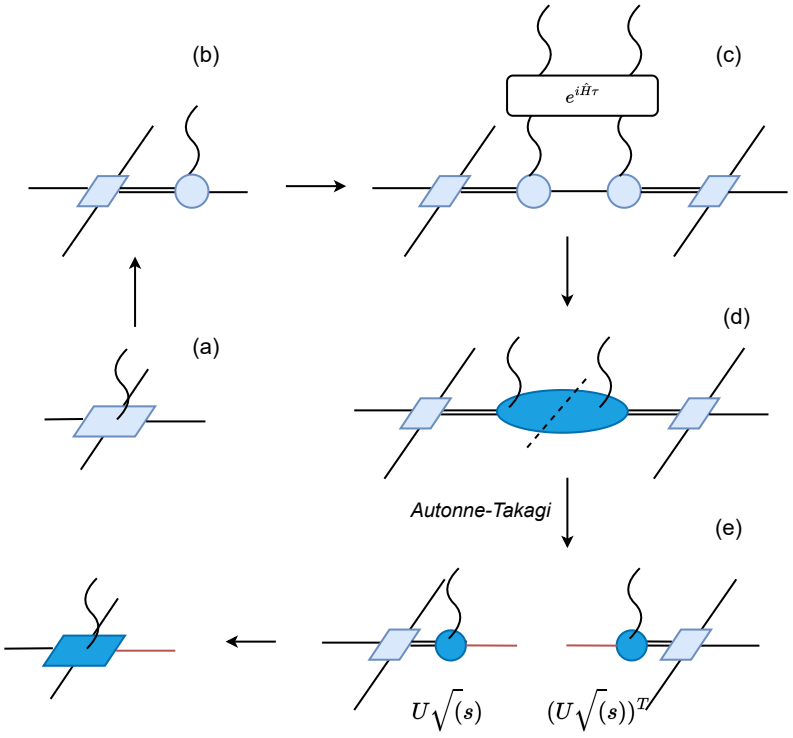

FIGURE B.8: L'idée de base d'une mise à jour simple. En appliquant la porte à deux sites, nous obtenons un tenseur agrandi qui peut être divisé en deux moitiés symétriques en utilisant la décomposition Autonne-Takagi. En pratique, nous séparerons la liaison et effectuerons le 'processus de fixation de la jauge'.

1. Les tenseurs d'un site et de son voisin sont d'abord divisés par décomposition en valeurs singulières (SVD) pour isoler la liaison active sur laquelle la porte symétrique complexe $\mathcal{G}_k$ est appliquée.

2. La matrice SU complexe symétrique à deux sites qui en résulte est factorisée à l'aide de la décomposition d'Autonne-Takagi. décomposition d'Autonne-Takagi. Les plus grandes valeurs singulières de D_{cut} sont conservées, et les autres sont éliminées pour réduire la dimension de la liaison.

3. Les composantes mises à jour sont utilisées pour construire le nouveau tenseur.

4. La procédure est répétée sur les liaisons restantes.

5. Une fois toutes les liaisons mises à jour, le tenseur est symétrisé et projeté dans le collecteur SU(2) pour obtenir les coefficients pertinents.

Afin de déterminer l'espace virtuel pertinent du tenseur résultant pour pouvoir choisir l'ensemble approprié de tenseurs dans lequel se projeter, nous pouvons simplement regarder les multiplicités des valeurs singulières obtenues à l'étape-2. La présence d'une particule de spin-s dans la liaison virtuelle donne lieu à un multiplet de dégénérescence $(2s+1)$. En tronquant la liaison, il faut veiller à ne pas couper les multiplicités, car cela entraînerait la rupture de la symétrie SU(2).

La dernière étape du schéma de mise à jour simple introduit une nouvelle série de défis. La décomposition d'Autonne-Takagi n'est pas unique, car il existe de multiples unitaires U qui donnent lieu à une SVD symétrique valide. En particulier, pour toute décomposition de matrice symétrique $A = MM^T$, on peut obtenir une matrice de jauge g qui est complexe-orthogonale de telle sorte que,

$$A = Mgg^T M^T = (Mg)(Mg)^T.$$

Comme cette matrice de jauge est arbitraire et ne peut pas être fixée, chaque étape de la procédure de mise à jour simple pourrait introduire une matrice de jauge différente sur différentes liaisons et entraîner un changement de base. Sans corriger cette liberté de jauge, nous ne pouvons pas symétriser le tenseur ou le projeter dans le sous-espace SU(2) pertinent. Par conséquent, nous effectuons une procédure de fixation de la jauge, expliquée en détail au chapitre 3.

Corner transfer matrix renormalization group (CTMRG)

Cet algorithme permet de contracter approximativement un réseau de tenseurs bi-couches dans la limite thermodynamique. Dans ce travail, nous présentons une extension symétrique complexe C_{4v} de la procédure CTMRG introduite par Orus et Vidal. L'idée de base consiste à classer l'espace réel en huit groupes. La contraction des tenseurs dans le groupe est représentée par quatre matrices de coin identiques et quatre tenseurs de bord identiques, comme indiqué sur la figure B.9. Afin de se contracter approximativement, nous représentons les tenseurs coin et arête par une dimension finie mais grande χ. L'algorithme peut alors être résumé dans les étapes suivantes.

1. **Initialiser C et T** : On obtient le coin initial en contractant deux jambes du tenseur bi-couche E De même, nous obtenons le coin initial en divisant l'une des jambes du tenseur bi-couche E en deux jambes de dimension D puis en les contractant.

2. **Enlarge C**: Nous absorbons un tenseur bi-couche à site unique dans le coin. Cela augmente la taille du coin de $\chi \times \chi$ à $(\chi D^2) \times (\chi D^2)$.

3. **Agrandir T** Nous absorbons un tenseur bi-couche dans le tenseur de bord. Cela augmente la taille de T de $\chi \times D^2 \times \chi$ à $(\chi D^2) \times D^2 \times (\chi D^2)$

4. **Obtenir les projecteurs**: un projecteur approprié P_i est une matrice qui tronque chaque liaison élargie de (χD^2) à χ.

5. **Renormaliser C et T** : Appliquer les projecteurs P_i sur C agrandi et T agrandi et les réduire au mieux à leur taille initiale. Par conséquent, le nouveau coin sera $P_1 C P_2^T$ et le nouveau bord sera $P_3 T P_4^T$ comme indiqué sur la figure 3.5.

6. **Convergence** les étapes (b) à (f) seront répétées jusqu'à ce que le critère de convergence soit satisfait.

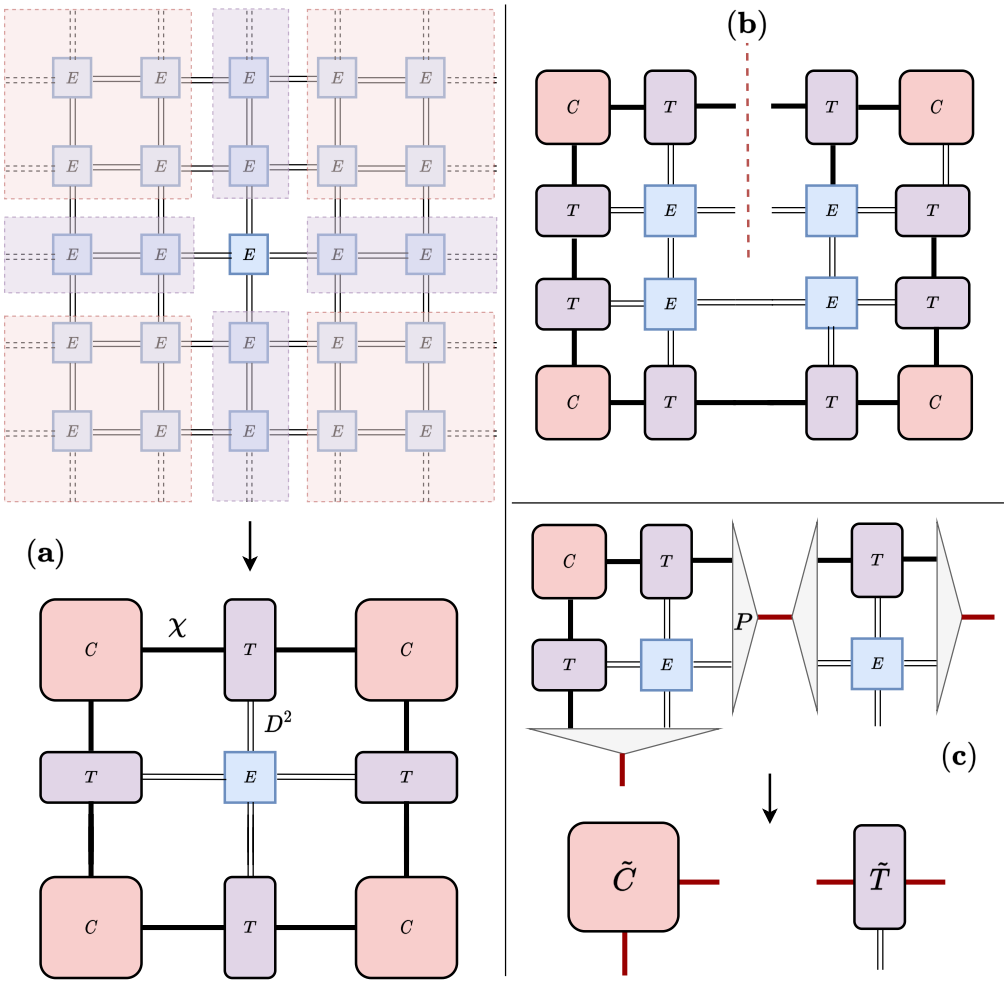

FIGURE B.9: (a) Dans le formalisme de matrice de transfert de coin, la contraction de la matrice de densité réduite de la fonction d'onde iPEPS est remplacée par quatre matrices de coin C de dimension $(\chi \times \chi)$ et quatre tenseurs d'arête T de dimensions $(D^2 \times \chi \times \chi)$. La symétrie C_{4v} et l'invariance translationnelle de la fonction d'onde se traduisent par toutes les matrices de coin identiques qui sont à symétrie complexe. De même, les tenseurs d'arête T sont identiques et ont une symétrie de réflexion autour de l'axe passant par la jambe de dimension D^2. (b) La matrice de densité réduite qui doit être approchée. (c) Étape de renormalisation qui réduit la dimension de liaison du coin de $(\chi D^2 \times \chi D^2)$ à $\chi \times \chi$ et le tenseur d'arête T de $(D^2 \times \chi D^2 \times \chi D^2)$ à $(D^2 \times \chi \times \chi)$.

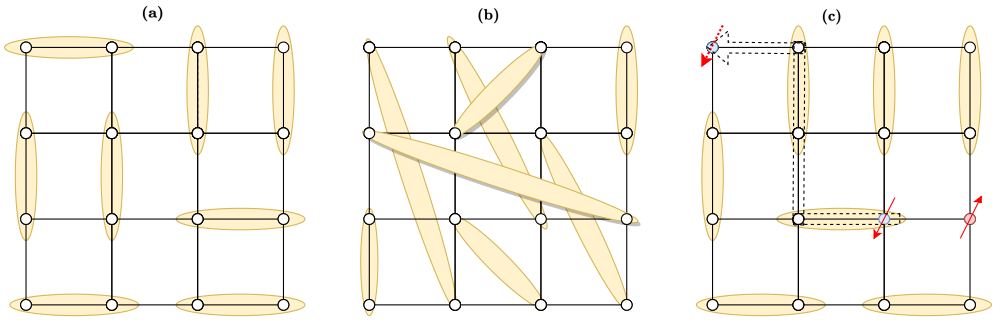

FIGURE B.10: (a) Un exemple de configuration de la liaison de valence du plus proche voisin. L'état NN-RVB est la superposition à poids égal de toutes ces configurations. (b) Un VBS avec des dimères à longue portée. (c) Excitation d'un spinon dans un état NN-RVB. La ligne pointillée correspond au chemin suivi par un spinon.

Le changement clé dans la version symétrique complexe de CTMRG est l'utilisation de la décomposition orthogonale pour obtenir les projecteurs. Si une matrice M est à symétrie complexe, alors elle peut être décomposée comme suit,

$$M = ODO^T \tag{B.10}$$

où O est une matrice orthogonale à entrées complexes (non hermitiennes) et D est une matrice diagonale dont les entrées sont les valeurs propres de la matrice M. Le projecteur est construit à partir des vecteurs propres orthogonaux correspondant aux plus grandes valeurs propres χ.

B.3 Evolution temporelle de l'état critique RVB

Nous étudions maintenant l'évolution temporelle de l'état RVB, qui est la superposition de poids égal de tous les états de liaison de valence voisins les plus proches possibles représentés sur la figure B.10-(a). Il a été démontré que cet état peut être représenté exactement par un tenseur PEPS avec une dimension de liaison D=3 et un espace virtuel $V = 0 \oplus \frac{1}{2}$. Les règles de fusion SU(2) limitent le nombre de tenseurs indépendants à seulement deux, T_1 et T_2, avec les numéros d'occupation $n_{\text{occ}} = \{3, 1\}$ et $n_{\text{occ}} = \{1, 3\}$ qui correspondent aux états avec des singulets voisins les plus proches et des singulets à longue portée comme indiqué dans figure B.10-(a)&(b). Pour construire n'importe quel PEPS symétrique SU(2) d'état RVB, nous utilisons simplement,

$$A_{RVB} = \lambda_1 T_1^{D=3} + \lambda_2 T_2^{D=3}. \tag{B.11}$$

Pour l'état NN-RVB, on met simplement $\lambda_2 = 0$.

PEPS

Avec le NN-RVB sur un réseau carré infini comme point de départ, nous supposons un quench Hamiltonien global à t=0, en activant le hamiltonien de Heisenberg antiferromagnétique du plus proche voisin (NN),

$$\mathcal{H}(t) = \begin{cases} 0, & \text{for } t \leq 0 \\ H = \sum_{\langle i,j \rangle} J\mathbf{S}_i \cdot \mathbf{S}_i, & \text{for } t > 0 \end{cases} \tag{B.12}$$

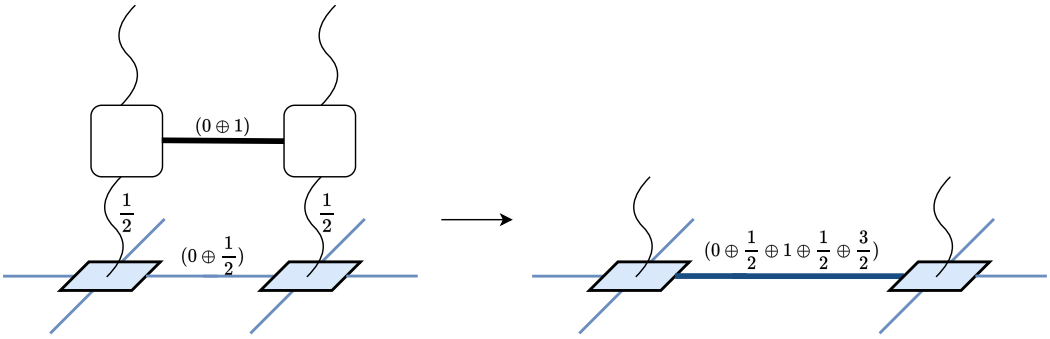

FIGURE B.11: L'espace virtuel résultant après l'application de la porte d'évolution temporelle. Le nouvel espace virtuel a une dimension $D = 12$ avec $\mathcal{V} = (0 \oplus \frac{1}{2} \oplus 1 \oplus \frac{1}{2} \oplus \frac{3}{2})$. À l'aide des poids respectifs des différents spins, nous décidons d'utiliser les tenseurs $D = 6$ avec $(\mathcal{V} = 0 \oplus \frac{1}{2} \oplus 1)$ pour capturer au mieux la dynamique de l'état NN-RVB.

Par commodité, nous mesurerons l'énergie en unités de J, c'est-à-dire $J = 1$. L'état initial et l'hamiltonien H sont tous deux invariants SU(2). Si nous devions construire un PEPO à partir du terme à deux sites, la liaison virtuelle contiendrait un $V = \frac{1}{2} \otimes \frac{1}{2} = 0 \oplus 1$. L'opérateur d'évolution temporelle peut être décomposé en une exponentielle de l'opérateur à deux sites, qui contiendra également le même espace virtuel. De plus, l'évolution temporelle étant une fonction algébrique de l'hamiltonien, la valeur attendue devrait rester constante. La valeur attendue de l'hamiltonien pour l'état initial NN-RVB pour $\chi = 180$ est ~ 0.59185.

Lorsque l'on applique l'opérateur d'évolution temporelle à l'état NN-RVB, la dimension de liaison résultante présente un espace virtuel de $V = (0 \oplus 1) \otimes (0 \oplus \frac{1}{2}) = (0 \oplus \frac{1}{2} \oplus 1\frac{1}{2} \oplus \frac{3}{2})$ comme le montre la figure B.11. Sur la base des poids des valeurs singulières des spins virtuels, nous concluons qu'un tenseur PEPS avec D=6 et $V = (0 \oplus \frac{1}{2} \oplus 1)$ est le choix optimal pour étudier la dynamique d'extinction de l'état NN-RVB.

Avec $V = (0 \oplus \frac{1}{2} \oplus 1)$, les nombres d'occupation possibles du spin virtuel-0, spin-$\frac{1}{2}$ et spin-1 à chaque site qui peut être projeté dans un espace physique de spin-$\frac{1}{2}$ sont $n_{\text{occ}} = \{1,3,0\}, \{3,1,0\}, \{0,3,1\}, \{2,1,1\}, \{0,1,3\}, \{1,1,2\}$. La base tensorielle symétrique du réseau C_{4v}/spin-SU(2) résultante $\{T_a\}$ contient un ensemble de 11 tenseurs orthogonaux à valeurs réelles. En les utilisant, on peut construire n'importe quel tenseur PEPS symétrique C_{4v}/spin-SU(2) à valeurs complexes par,

$$A(t) = \sum_{a=1}^{11} \mu_a(t)\, T_a, \tag{B.13}$$

où $\mu_a(t) \in \mathbb{C}$. Un aperçu des tenseurs de base pour D=3 et D=6 avec les symétries C_{4v} et C_s est donné par le tableau B.1

D	$\mathcal{V}$	C_s	C_s/U(1)	C_{4v}	C_{4v}/U(1)
3	$0 \oplus \frac{1}{2}$	7	4	2	1
6	$0 \oplus \frac{1}{2} \oplus 1$	41	30	11	8

TABLE B.1: Nombre de tenseurs locaux symétriques SU(2) de dimension de liaison $D = 3$ ou $D = 6$, espace virtuel $\mathcal{V}$, symétrie de groupe ponctuel C_s ou C_{4v}, et avec/sans symétrie de jauge U(1). Le nombre de tenseurs symétriques C_s donne le nombre de degrés de liberté disponibles à chaque sous-pas temporel. Nous constatons explicitement que les tenseurs symétriques non U(1) conservent un poids nul lors de l'évolution temporelle.

résultats de mise à jour simples

Tout d'abord, nous aimerions voir si l'espace virtuel $V = (0 \oplus \frac{1}{2} \oplus 1)$ capture l'état mieux que les autres. Comme l'intrication croît rapidement avec le temps, nous nous attendons à ce que les autres états virtuels deviennent plus significatifs. Sur la figure B.13, nous représentons les valeurs singulières λ_i obtenues par la décomposition d'Autonne-Takagi de la procédure de mise à jour simple et l'entropie d'intrication de liaison correspondante $S_{D=6} = -\sum_{i=1}^{6} \lambda_i \ln(\lambda_i)$. Cependant, nous observons également que les trois multiplets de D=6 restent bien au-dessus du reste du spectre.

Nous observons, sur la base des coefficients obtenus à partir du schéma SU, comme le montre la figure , que les coefficients correspondant au numéro d'occupation du spin virtuel-$\frac{1}{2}$ $n_{\frac{1}{2}} = 3$ reste toujours exactement nul fois. En conséquence, à partir de la cartographie de représentation de la hauteur, nous pouvons conclure que la phase de Coulomb U(1) loi de Gauss est maintenue tout au long de la simulation, et que l'état reste critique. Cela implique que le chevauchement de l'état évolué dans le temps avec les singulets à longue portée de la fonction d'onde est strictement nul à tout moment.

Echo de Loschmidt

Afin d'établir le temps maximum ci-dessus que notre procédure échoue, nous avons effectué le suivant la procédure de "renversement du temps" ; (i) l'évolution dans le temps est effectuée avec l'hamiltonien H et l'opérateur d'évolution temporelle e^{iHt} de $t = 0$ à $t = t_R$. (ii) alors, à $t = t_R$ le temps est "inversé", $t \to -t$, c'est-à-dire le temps l'évolution est effectuée avec l'opérateur d'évolution temporelle e^{iHt}. Dans le cas d'une évolution unitaire exacte, on devrait retrouver exactement état initial NN RVB au temps $t = 2t_R$, c'est-à-dire $|\langle \mathcal{A}(t = 2t_R)|\mathcal{A}(0)\rangle| \sim 1$. Ce chevauchement est appelé écho de Loschmidt. Le recouvrement en fonction de t est représenté sur la figure B.14-(a) et l'écho de Loschmidt est représenté sur la figure B.14-(b). Nous remarquons à partir du tracé de l'écho de Loschmidt que le temps maximum jusqu'auquel le SU est valide est, $t_{max} \sim 1$.

Energie

Comme expliqué précédemment, l'énergie des tenseurs SU est calculée à l'aide de l'algorithme iPEPS de l'algorithme de renormalisation de la matrice de transfert de coin (CTMRG) à symétrie complexe. En raison de la nature critique de la fonction d'onde, les valeurs d'énergie convergent très lentement. Plusieurs valeurs de χ sont donc considérées. La figure B.15 montre l'énergie par site en fonction du temps t pour des χ allant de D^2 à $3D^2$. Pour la plus petite valeur de $\chi = D^2$, on voit clairement un plateau au petit temps $t \sim 0.15$ et, ensuite, une déviation claire de l'énergie initiale $t = 0$. En augmentant χ, la déviation se produit encore plus rapidement. Remarquez l'échelle d'énergie utilisée dans la figure B.15, qui montre que l'écart d'énergie reste encore relativement faible jusqu'au temps intermédiaire, c'est-à-dire 0.6% à $t = 0.2$.

Résultats de la matrice de transfert

Pour étudier les propriétés critiques de l'état, nous utilisons le formalisme de la matrice de transfert. Dans ce cas, une matrice de transfert est construite à l'aide de deux tenseurs d'arête T et d'un tenseur élémentaire E comme indiqué sur la figure B.16-(a). A partir du spectre de cette matrice de transfert, représenté sur la figure, on peut calculer plusieurs longueurs de corrélation. Figure B.17 montre le spectre de la matrice de transfert aux temps t=0.15 et t=0.5. Le terme sous-leadique, les niveaux dégénérés correspondant au singlet et au doublet sont marqués. Comme prévu, le terme sous-leading présente un écart de vanisation. Dans la figure.B.18-(a), nous traçons les longueurs de corrélation des autres multiplets obtenus à partir du TM pour différents χ et à différents moments. Nous observons que la longueur de corrélation du singulet obtenue à partir du TM correspond bien à la longueur de corrélation calculée à partir des données de corrélation spin-spin.

La nature critique du PEPS massif se reflète également dans la nature critique du MPS limite avec une charge centrale $c = 1$. Nous confirmons cette caractéristique en calculant l'entropie de von Neumann S_{vN} et en l'ajustant au logarithme de la longueur de corrélation maximale $\ln(\xi_{max})$. La charge centrale peut être calculée à l'aide de la relation $S_{vN} \sim \frac{c}{6} \ln(\xi_{max})$. Sur la figure B.18-(b), nous montrons que l'ajustement pour $c \approx 1$ confirme la nature critique.

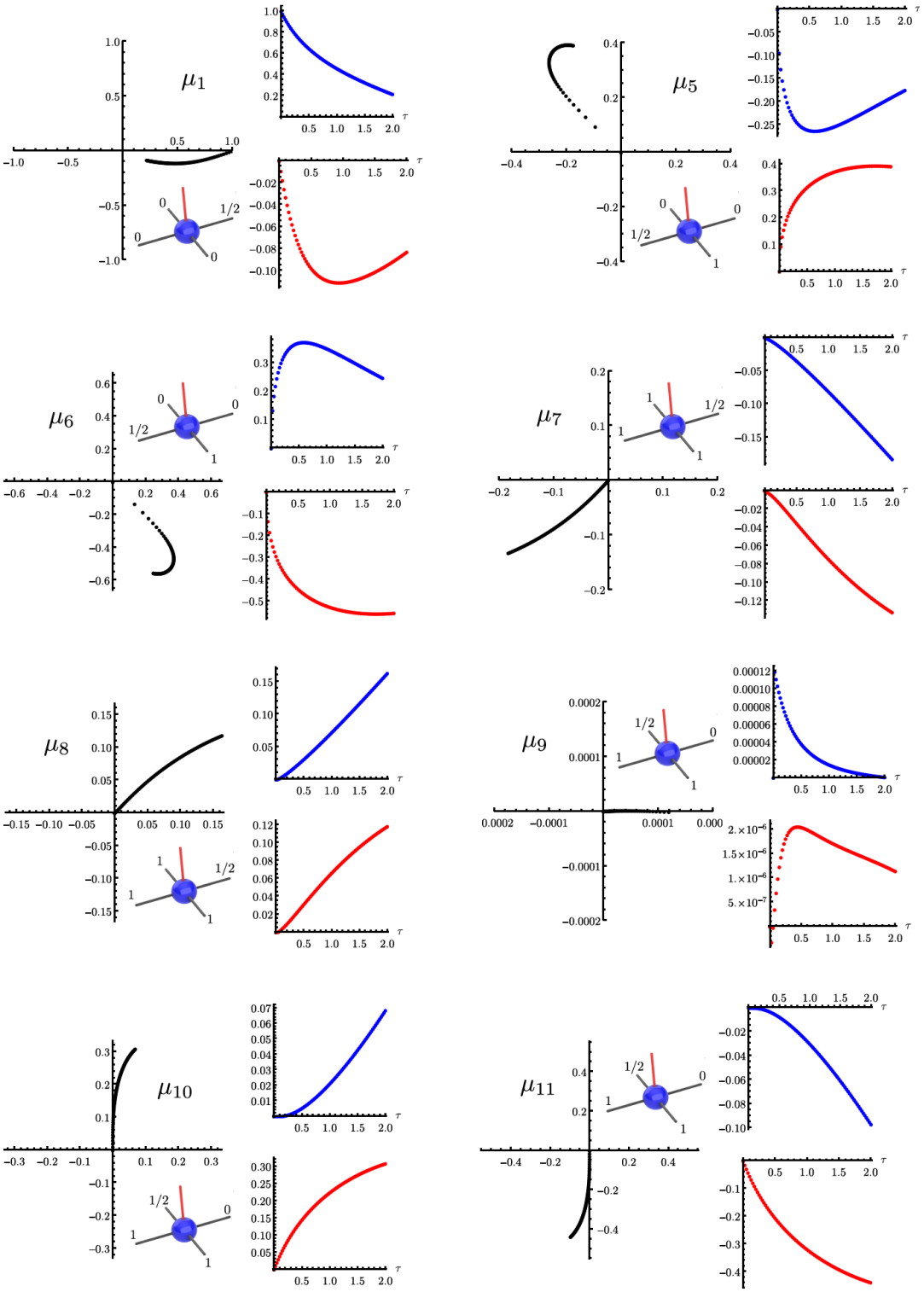

FIGURE B.12: Évolution temporelle des composantes complexes $\mathcal{A}(t)$ μ_i obtenues à partir du schéma de mise à jour simple avec $\tau = 0.025$ dans la plage temporelle $\in [0, 2]$. Dans chaque panneau, μ est affiché dans le plan complexe (points noirs) ainsi que sa partie réelle (sphères bleues) et sa partie imaginaire (sphères rouges). Les composantes μ_2, μ_3 et μ_4 étant identiquement nulles ne sont pas affichées.

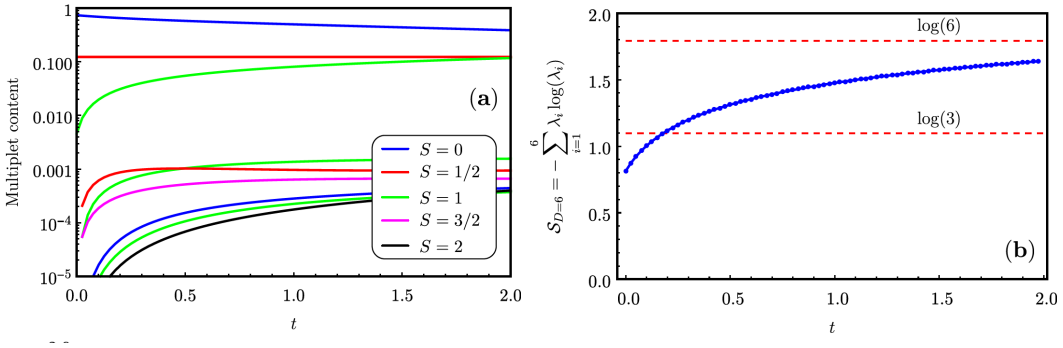

FIGURE B.13: (a) Valeurs singulières λ_i de la factorisation d'Autonne-Takagi de la matrice porte SU représentée dans la figure B.11. (b) Entropie d'intrication de la liaison obtenue à l'aide des valeurs singulières indiquées dans le sous-graphe (a) $S_{D=6} = -\sum_{i=1}^{6} \lambda_i \ln(\lambda_i)$.

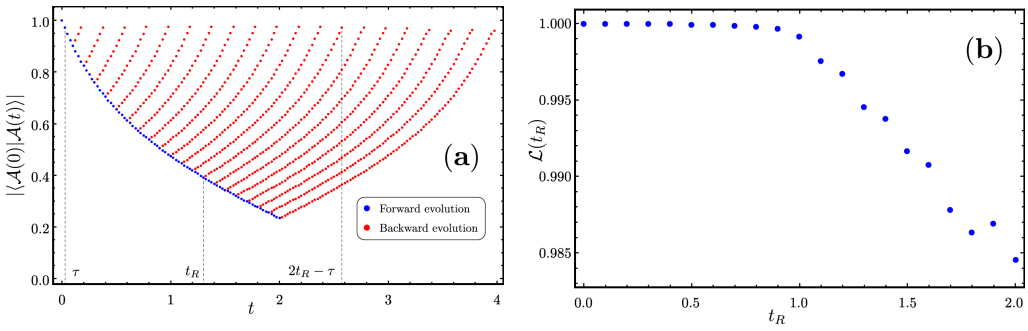

FIGURE B.14: (a) Chevauchement $|\langle \mathcal{A}(t)|\mathcal{A}(0)\rangle|$ du tenseur dépendant du temps avec le tenseur initial définissant l'état RVB NN ($\lambda_2 = 0$) en fonction du temps (points bleus). Les points rouges sont utilisés après le retournement temporel à $t = t_R$, en remontant dans le temps. (b) écho de Loschmidt $\mathcal{L}(t_R) = |\langle \mathcal{A}(t = 2t_R - \tau)|\mathcal{A}(\tau)\rangle|$ en fonction de t_R. Notez que, par commodité, $\mathcal{L}(t_R)$ n'est pas évalué entre les temps 0 et $2t_R$ mais entre les temps τ et $2t_R - \tau$ pour éviter un saut dimensionnel de $D = 3$ au temps 0 à $D = 6$ au temps $t > 0$. Dans (a) et (b), la méthode SU est utilisée avec $\tau = 0.025$.

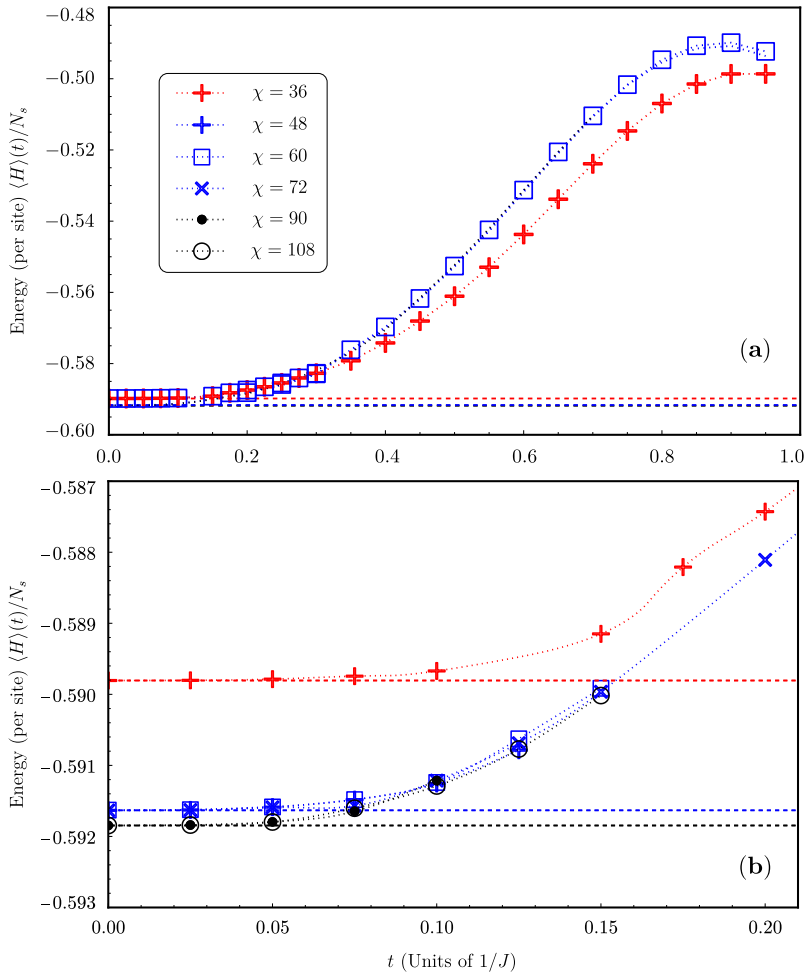

FIGURE B.15: L'énergie par site de la fonction d'onde obtenue à partir du résultat iPEPS en utilisant les tenseurs SU $D = 6$.

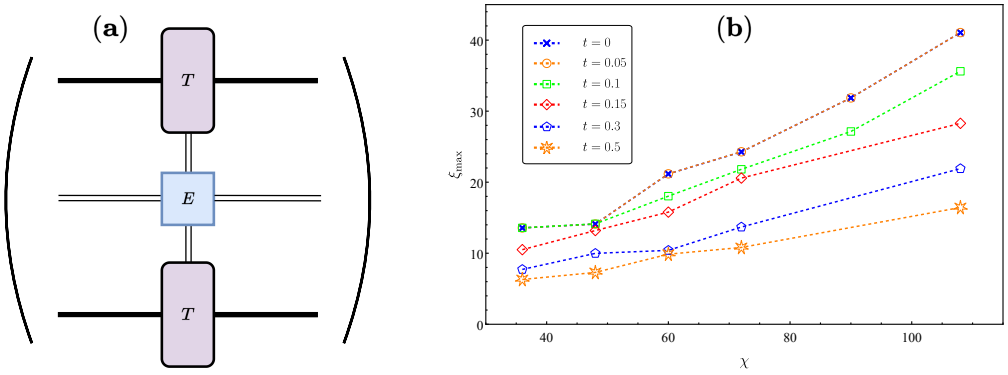

FIGURE B.16: (a) La matrice de transfert construite à l'aide du tenseur de bord T. (b) ξ_{max} obtenu à partir du logarithme du rapport entre les valeurs propres principales et secondaires $\frac{\lambda_2}{\lambda_1}$ de la matrice de transfert représentée.

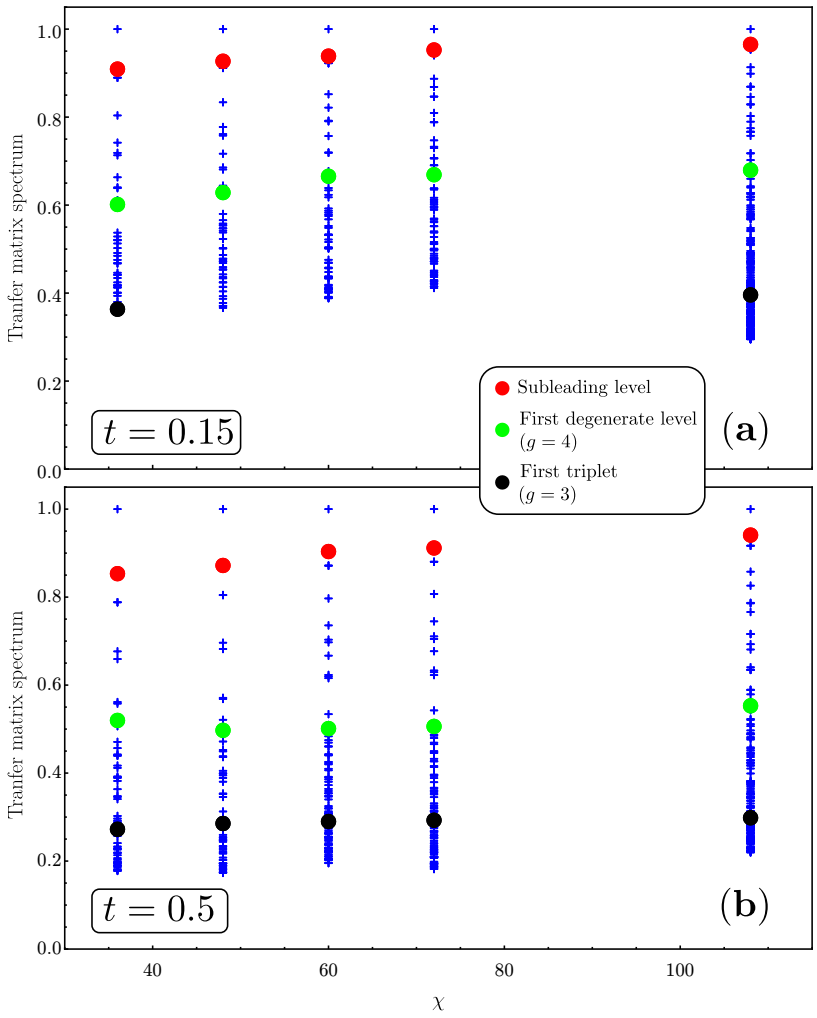

FIGURE B.17: Le spectre complet de la matrice de transfert représentée sur la figure B.16 à $t = 0.15$ et $t = 0.5$. Les points rouges marquent le terme sous-chef, les points verts marquent le premier multiplet (dégénérescence g=2), et le point noir représente le premier triplet. La distance décroissante entre le terme principal et le terme secondaire indique une longueur de corrélation divergente.

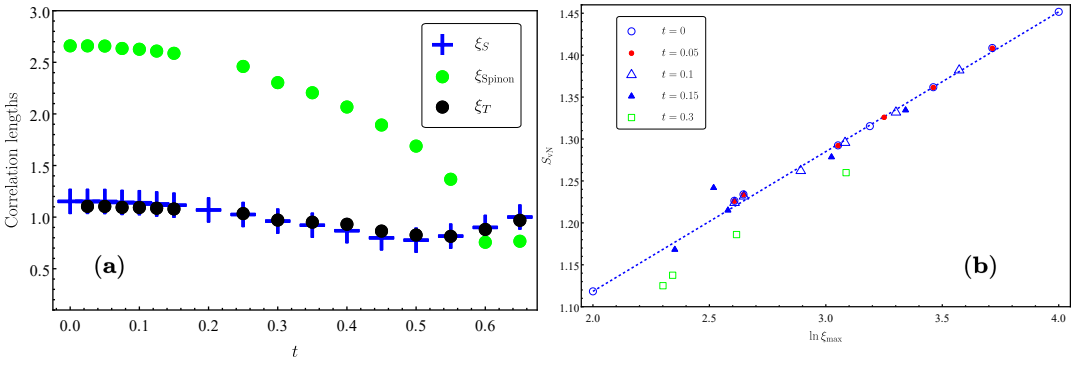

FIGURE B.18: (a) Longueurs de corrélation obtenues à partir du TM à partir de la décroissance exponentielle des multiplets comme observé dans B.17 ainsi que la longueur de corrélation spin-spin obtenue par un ajustement exponentiel des données de longueur de corrélation spin-spin. (b) Entropie d'intrication du MPS limite en fonction de $\ln(\xi_{max})$ pour différents temps t = 0, 0.05,0.1,0.15 et 0.3. La ligne en pointillés correspond à la pente= $\frac{1}{6}$, un comportement attendu pour $c = 1$.

Bibliography

[1] P. W. Anderson. “More Is Different”. In: *Science* 177.4047 (1972), pp. 393–396. DOI: 10.1126/science.177.4047.393. eprint: https://www.science.org/doi/pdf/10.1126/science.177.4047.393. URL: https://www.science.org/doi/abs/10.1126/science.177.4047.393.

[2] G. Semeghini et al. “Probing topological spin liquids on a programmable quantum simulator”. In: *Science* 374.6572 (2021), pp. 1242–1247. DOI: 10.1126/science.abi8794. eprint: https://www.science.org/doi/pdf/10.1126/science.abi8794. URL: https://www.science.org/doi/abs/10.1126/science.abi8794.

[3] Aditi Mitra. “Quantum Quench Dynamics”. In: *Annual Review of Condensed Matter Physics* 9.1 (2018), pp. 245–259. DOI: 10.1146/annurev-conmatphys-031016-025451. eprint: https://doi.org/10.1146/annurev-conmatphys-031016-025451. URL: https://doi.org/10.1146/annurev-conmatphys-031016-025451.

[4] a, familyi=c., given=Helena, giveni=H., „ et al. “Quench dynamics and relaxation of a spin coupled to interacting leads”. In: *Phys. Rev. B* 103 (12 2021), p. 125152. DOI: 10.1103/PhysRevB.103.125152. URL: https://link.aps.org/doi/10.1103/PhysRevB.103.125152.

[5] Masaya Kunimi et al. “Performance evaluation of the discrete truncated Wigner approximation for quench dynamics of quantum spin systems with long-range interactions”. In: *Phys. Rev. Res.* 3 (1 2021), p. 013060. DOI: 10.1103/PhysRevResearch.3.013060. URL: https://link.aps.org/doi/10.1103/PhysRevResearch.3.013060.

[6] Vincenzo Alba and Pasquale Calabrese. “Entanglement and thermodynamics after a quantum quench in integrable systems”. In: *Proceedings of the National Academy of Sciences* 114.30 (2017), pp. 7947–7951. DOI: 10.1073/pnas.1703516114. eprint: https://www.pnas.org/doi/pdf/10.1073/pnas.1703516114. URL: https://www.pnas.org/doi/abs/10.1073/pnas.1703516114.

[7] Stefanie Czischek, Martin Gärttner, and Thomas Gasenzer. “Quenches near Ising quantum criticality as a challenge for artificial neural networks”. In: *Phys. Rev. B* 98 (2 2018), p. 024311. DOI: 10.1103/PhysRevB.98.024311. URL: https://link.aps.org/doi/10.1103/PhysRevB.98.024311.

[8] N.W. Ashcroft and N.D. Mermin. *Solid State Physics*. Cengage Learning, 2011. ISBN: 9788131500521. URL: https://books.google.fr/books?id=x_s_YAAACAAJ.

[9] D. Bohm. "Note on a Theorem of Bloch Concerning Possible Causes of Superconductivity". In: *Phys. Rev.* 75 (3 1949), pp. 502–504. DOI: 10.1103/PhysRev.75.502. URL: https://link.aps.org/doi/10.1103/PhysRev.75.502.

[10] Gregory H. Wannier. "The Structure of Electronic Excitation Levels in Insulating Crystals". In: *Phys. Rev.* 52 (3 1937), pp. 191–197. DOI: 10.1103/PhysRev.52.191. URL: https://link.aps.org/doi/10.1103/PhysRev.52.191.

[11] "Electron correlations in narrow energy bands". In: *Proceedings of the Royal Society of London. Series A. Mathematical and Physical Sciences* 276.1365 (Nov. 1963), pp. 238–257. DOI: 10.1098/rspa.1963.0204. URL: https://doi.org/10.1098/rspa.1963.0204.

[12] R. B. Laughlin. "A Critique of Two Metals". In: *arXiv e-prints*, cond-mat/9709195 (Sept. 1997), cond–mat/9709195. arXiv: cond-mat/9709195 [cond-mat.supr-con].

[13] Charles L. Cleveland and Rodrigo Medina A. "Obtaining a Heisenberg Hamiltonian from the Hubbard model". In: *American Journal of Physics* 44.1 (Jan. 1976), pp. 44–46. DOI: 10.1119/1.10537. URL: https://doi.org/10.1119/1.10537.

[14] H. Bethe. "Zur Theorie der Metalle". In: *Zeitschrift für Physik* 71.3 (1931), pp. 205–226. ISSN: 0044-3328. DOI: 10.1007/BF01341708. URL: https://doi.org/10.1007/BF01341708.

[15] Ta-Pei Cheng and Ling-Fong Li. *Gauge theory of elementary particle physics*. en. Oxford science publications. London, England: Oxford University Press, 1984.

[16] Jin-Quan Chen. *Group Representation Theory for Physicists*. WORLD SCIENTIFIC, Mar. 1989. DOI: 10.1142/0262. URL: https://doi.org/10.1142/0262.

[17] Eugene D. Commins. "Electron Spin and Its History". In: *Annual Review of Nuclear and Particle Science* 62.1 (2012), pp. 133–157. DOI: 10.1146/annurev-nucl-102711-094908. eprint: https://doi.org/10.1146/annurev-nucl-102711-094908. URL: https://doi.org/10.1146/annurev-nucl-102711-094908.

[18] Lars Onsager. "Crystal Statistics. I. A Two-Dimensional Model with an Order-Disorder Transition". In: *Phys. Rev.* 65 (3-4 1944), pp. 117–149. DOI: 10.1103/PhysRev.65.117. URL: https://link.aps.org/doi/10.1103/PhysRev.65.117.

[19] N. D. Mermin and H. Wagner. "Absence of Ferromagnetism or Antiferromagnetism in One- or Two-Dimensional Isotropic Heisenberg Models". In: *Phys. Rev. Lett.* 17 (22 1966), pp. 1133–1136. DOI: 10.1103/PhysRevLett.17.1133. URL: https://link.aps.org/doi/10.1103/PhysRevLett.17.1133.

[20] Lucile Savary and Leon Balents. "Quantum spin liquids: a review". In: *Reports on Progress in Physics* 80.1 (2016), p. 016502. DOI: 10.1088/0034-4885/80/1/016502. URL: https://dx.doi.org/10.1088/0034-4885/80/1/016502.

[21] J Vannimenus and G Toulouse. "Theory of the frustration effect. II. Ising spins on a square lattice". In: *Journal of Physics C: Solid State Physics* 10.18 (1977), p. L537. DOI: 10.1088/0022-3719/10/18/008. URL: https://dx.doi.org/10.1088/0022-3719/10/18/008.

[22] P.W. Anderson. "Resonating valence bonds: A new kind of insulator?" In: *Materials Research Bulletin* 8.2 (1973), pp. 153–160. ISSN: 0025-5408. DOI: https://doi.org/10.1016/0025-5408(73)90167-0. URL: https://www.sciencedirect.com/science/article/pii/0025540873901670.

[23] David A. Huse and Veit Elser. "Simple Variational Wave Functions for Two-Dimensional Heisenberg Spin-½ Antiferromagnets". In: *Phys. Rev. Lett.* 60 (24 1988), pp. 2531–2534. DOI: 10.1103/PhysRevLett.60.2531. URL: https://link.aps.org/doi/10.1103/PhysRevLett.60.2531.

[24] Christian Balz et al. "Physical realization of a quantum spin liquid based on a complex frustration mechanism". In: *Nature Physics* 12.10 (2016), pp. 942–949. ISSN: 1745-2481. DOI: 10.1038/nphys3826. URL: https://doi.org/10.1038/nphys3826.

[25] Tian-Heng Han et al. "Fractionalized excitations in the spin-liquid state of a kagome-lattice antiferromagnet". In: *Nature* 492.7429 (2012), pp. 406–410. ISSN: 1476-4687. DOI: 10.1038/nature11659. URL: https://doi.org/10.1038/nature11659.

[26] Martin Klanjšek et al. "A high-temperature quantum spin liquid with polaron spins". In: *Nature Physics* 13.11 (2017), pp. 1130–1134. ISSN: 1745-2481. DOI: 10.1038/nphys4212. URL: https://doi.org/10.1038/nphys4212.

[27] Yoshihiko Okamoto, Hiroyuki Yoshida, and Zenji Hiroi. "Vesignieite BaCu3V2O8(OH)2 as a Candidate Spin-1/2 Kagome Antiferromagnet". In: *Journal of the Physical Society of Japan* 78.3 (2009), p. 033701. DOI: 10.1143/JPSJ.78.033701. eprint: https://doi.org/10.1143/JPSJ.78.033701. URL: https://doi.org/10.1143/JPSJ.78.033701.

[28] Daiki Watanabe et al. "Emergence of nontrivial magnetic excitations in a spin-liquid state of kagomé volborthite". In: *Proceedings of the National Academy of Sciences* 113.31 (2016), pp. 8653–8657. DOI: 10.1073/pnas.1524076113. eprint: https://www.pnas.org/doi/pdf/10.1073/pnas.1524076113. URL: https://www.pnas.org/doi/abs/10.1073/pnas.1524076113.

[29] Wen-Yuan Liu et al. "Gapless quantum spin liquid and global phase diagram of the spin-1/2 J1-J2 square antiferromagnetic Heisenberg model". In: *Science Bulletin* 67.10 (2022), pp. 1034–1041. ISSN: 2095-9273. DOI: https://doi.org/10.1016/j.scib.2022.03.010. URL: https://www.sciencedirect.com/science/article/pii/S2095927322001001.

[30] F.D.M. Haldane. "Continuum dynamics of the 1-D Heisenberg antiferromagnet: Identification with the O(3) nonlinear sigma model". In: *Physics Letters A* 93.9 (1983), pp. 464–468. ISSN: 0375-9601. DOI: https://doi.org/10.1016/0375-9601(83)90631-X. URL: https://www.sciencedirect.com/science/article/pii/037596018390631X.

[31] F. D. M. Haldane. "Nonlinear Field Theory of Large-Spin Heisenberg Antiferromagnets: Semiclassically Quantized Solitons of the One-Dimensional Easy-Axis Néel State". In: *Phys. Rev. Lett.* 50 (15 1983), pp. 1153–1156. DOI: 10.1103/PhysRevLett.50.1153. URL: https://link.aps.org/doi/10.1103/PhysRevLett.50.1153.

[32] Elliott Lieb, Theodore Schultz, and Daniel Mattis. "Two soluble models of an antiferromagnetic chain". In: *Annals of Physics* 16.3 (1961), pp. 407–466. ISSN: 0003-4916. DOI: https://doi.org/10.1016/0003-4916(61)90115-4. URL: https://www.sciencedirect.com/science/article/pii/0003491661901154.

[33] Masaki Oshikawa. "Commensurability, Excitation Gap, and Topology in Quantum Many-Particle Systems on a Periodic Lattice". In: *Phys. Rev. Lett.* 84 (7 2000), pp. 1535–1538. DOI: 10.1103/PhysRevLett.84.1535. URL: https://link.aps.org/doi/10.1103/PhysRevLett.84.1535.

[34] M. B. Hastings. "Lieb-Schultz-Mattis in higher dimensions". In: *Phys. Rev. B* 69 (10 2004), p. 104431. DOI: 10.1103/PhysRevB.69.104431. URL: https://link.aps.org/doi/10.1103/PhysRevB.69.104431.

[35] Ian Affleck et al. "Rigorous results on valence-bond ground states in antiferromagnets". In: *Phys. Rev. Lett.* 59 (7 1987), pp. 799–802. DOI: 10.1103/PhysRevLett.59.799. URL: https://link.aps.org/doi/10.1103/PhysRevLett.59.799.

[36] Zheng-Cheng Gu and Xiao-Gang Wen. "Tensor-entanglement-filtering renormalization approach and symmetry-protected topological order". In: *Phys. Rev. B* 80 (15 2009), p. 155131. DOI: 10.1103/PhysRevB.80.155131. URL: https://link.aps.org/doi/10.1103/PhysRevB.80.155131.

[37] Frank Pollmann et al. "Symmetry protection of topological phases in one-dimensional quantum spin systems". In: *Phys. Rev. B* 85 (7 2012), p. 075125. DOI: 10.1103/PhysRevB.85.075125. URL: https://link.aps.org/doi/10.1103/PhysRevB.85.075125.

[38] Hal Tasaki. "Topological Phase Transition and $\mathbb{Z}_2$ Index for $S = 1$ Quantum Spin Chains". In: *Phys. Rev. Lett.* 121 (14 2018), p. 140604. DOI: 10.1103/PhysRevLett.121.140604. URL: https://link.aps.org/doi/10.1103/PhysRevLett.121.140604.

[39] Tzu-Chieh Wei, Ian Affleck, and Robert Raussendorf. "Two-dimensional Affleck-Kennedy-Lieb-Tasaki state on the honeycomb lattice is a universal resource for quantum computation". In: *Phys. Rev. A* 86 (3 2012), p. 032328. DOI: 10.1103/PhysRevA.86.032328. URL: https://link.aps.org/doi/10.1103/PhysRevA.86.032328.

[40] Ian Affleck et al. "Valence bond ground states in isotropic quantum antiferromagnets". In: *Communications in Mathematical Physics* 115.3 (1988), pp. 477–528. ISSN: 1432-0916. DOI: 10.1007/BF01218021. URL: https://doi.org/10.1007/BF01218021.

[41] Xie Chen, Zheng-Xin Liu, and Xiao-Gang Wen. "Two-dimensional symmetry-protected topological orders and their protected gapless edge excitations". In: *Phys. Rev. B* 84 (23 2011), p. 235141. DOI: 10.1103/PhysRevB.84.235141. URL: https://link.aps.org/doi/10.1103/PhysRevB.84.235141.

[42] Samuel Gozel et al. "Novel families of SU(N) AKLT states with arbitrary self-conjugate edge states". In: *Nuclear Physics B* 945 (2019), p. 114663. ISSN: 0550-3213. DOI: https://doi.org/10.1016/j.nuclphysb.2019.114663. URL: https://www.sciencedirect.com/science/article/pii/S055032131930149X.

[43] Olivier Gauthé and Didier Poilblanc. "Entanglement properties of the two-dimensional SU(3) Affleck-Kennedy-Lieb-Tasaki state". In: *Phys. Rev. B* 96 (12 2017), p. 121115. DOI: 10.1103/PhysRevB.96.121115. URL: https://link.aps.org/doi/10.1103/PhysRevB.96.121115.

[44] X. G. Wen. "Mean-field theory of spin-liquid states with finite energy gap and topological orders". In: *Phys. Rev. B* 44 (6 1991), pp. 2664–2672. DOI: 10.1103/PhysRevB.44.2664. URL: https://link.aps.org/doi/10.1103/PhysRevB.44.2664.

[45] X. G. Wen. "Vacuum degeneracy of chiral spin states in compactified space". In: *Phys. Rev. B* 40 (10 1989), pp. 7387–7390. DOI: 10.1103/PhysRevB.40.7387. URL: https://link.aps.org/doi/10.1103/PhysRevB.40.7387.

[46] Claudine Lacroix, Frederic Mila, and Philippe Mendels, eds. *Introduction to frustrated magnetism*. Springer Series in Solid-State Sciences. Berlin, Germany: Springer, Jan. 2011.

[47] T. Senthil and Matthew P. A. Fisher. "Z_2 gauge theory of electron fractionalization in strongly correlated systems". In: *Phys. Rev. B* 62 (12 2000), pp. 7850–7881. DOI: 10.1103/PhysRevB.62.7850. URL: https://link.aps.org/doi/10.1103/PhysRevB.62.7850.

[48] Ji-Yao Chen and Didier Poilblanc. "Topological $\mathbb{Z}_2$ resonating-valence-bond spin liquid on the square lattice". In: *Phys. Rev. B* 97 (16 2018), p. 161107. DOI: 10.1103/PhysRevB.97.161107. URL: https://link.aps.org/doi/10.1103/PhysRevB.97.161107.

[49] Don N. Page. "Average entropy of a subsystem". In: *Phys. Rev. Lett.* 71 (9 1993), pp. 1291–1294. DOI: 10.1103/PhysRevLett.71.1291. URL: https://link.aps.org/doi/10.1103/PhysRevLett.71.1291.

[50] J. Eisert, M. Cramer, and M. B. Plenio. "Colloquium: Area laws for the entanglement entropy". In: *Rev. Mod. Phys.* 82 (1 2010), pp. 277–306. DOI: 10.1103/RevModPhys.82.277. URL: https://link.aps.org/doi/10.1103/RevModPhys.82.277.

[51] Mark Srednicki. "Entropy and area". In: *Phys. Rev. Lett.* 71 (5 1993), pp. 666–669. DOI: 10.1103/PhysRevLett.71.666. URL: https://link.aps.org/doi/10.1103/PhysRevLett.71.666.

[52] M B Hastings. "An area law for one-dimensional quantum systems". In: *Journal of Statistical Mechanics: Theory and Experiment* 2007.08 (Aug. 2007), P08024–P08024. DOI: 10.1088/1742-5468/2007/08/p08024. URL: https://doi.org/10.1088/1742-5468/2007/08/p08024.

[53] Tomotaka Kuwahara and Keiji Saito. "Area law of noncritical ground states in 1D long-range interacting systems". In: *Nature Communications* 11.1 (2020), p. 4478. ISSN: 2041-1723. DOI: 10.1038/s41467-020-18055-x. URL: https://doi.org/10.1038/s41467-020-18055-x.

[54] Ramis Movassagh and Peter W. Shor. "Supercritical entanglement in local systems: Counterexample to the area law for quantum matter". In: *Proceedings of the National Academy of Sciences* 113.47 (2016), pp. 13278–13282. DOI: 10.1073/pnas.1605716113. eprint: https://www.pnas.org/doi/pdf/10.1073/pnas.1605716113. URL: https://www.pnas.org/doi/abs/10.1073/pnas.1605716113.

[55] M. H. Anderson et al. "Observation of Bose-Einstein Condensation in a Dilute Atomic Vapor". In: *Science* 269.5221 (July 1995), pp. 198–201. DOI: 10.1126/science.269.5221.198. URL: https://doi.org/10.1126/science.269.5221.198.

[56] K. B. Davis et al. "Bose-Einstein Condensation in a Gas of Sodium Atoms". In: *Phys. Rev. Lett.* 75 (22 1995), pp. 3969–3973. DOI: 10.1103/PhysRevLett.75.3969. URL: https://link.aps.org/doi/10.1103/PhysRevLett.75.3969.

[57] Javier Argüello-Luengo et al. "Quantum simulation of two-dimensional quantum chemistry in optical lattices". In: *Phys. Rev. Res.* 2 (4 2020), p. 042013. DOI: 10.1103/PhysRevResearch.2.042013. URL: https://link.aps.org/doi/10.1103/PhysRevResearch.2.042013.

[58] Florian Schäfer et al. "Tools for quantum simulation with ultracold atoms in optical lattices". In: *Nature Reviews Physics* 2.8 (2020), pp. 411–425. ISSN: 2522-5820. DOI: 10.1038/s42254-020-0195-3. URL: https://doi.org/10.1038/s42254-020-0195-3.

[59] Christian Gross and Immanuel Bloch. "Quantum simulations with ultracold atoms in optical lattices". In: *Science* 357.6355 (Sept. 2017), pp. 995–1001. DOI: 10.1126/science.aal3837. URL: https://doi.org/10.1126/science.aal3837.

[60] Christie S. Chiu et al. "String patterns in the doped Hubbard model". In: *Science* 365.6450 (July 2019), pp. 251–256. DOI: 10.1126/science.aav3587. URL: https://doi.org/10.1126/science.aav3587.

[61] Xia-Ji Liu, Peter D. Drummond, and Hui Hu. "Signature of Mott-Insulator Transition with Ultracold Fermions in a One-Dimensional Optical Lattice". In: *Phys. Rev. Lett.* 94 (13 2005), p. 136406. DOI: 10.1103/PhysRevLett.94.136406. URL: https://link.aps.org/doi/10.1103/PhysRevLett.94.136406.

[62] Matthew A. Nichols et al. "Spin transport in a Mott insulator of ultracold fermions". In: *Science* 363.6425 (Jan. 2019), pp. 383–387. DOI: 10.1126/science.aat4387. URL: https://doi.org/10.1126/science.aat4387.

[63] Peter T. Brown et al. "Bad metallic transport in a cold atom Fermi-Hubbard system". In: *Science* 363.6425 (Jan. 2019), pp. 379–382. DOI: 10.1126/science.aat4134. URL: https://doi.org/10.1126/science.aat4134.

[64] Akiko Masaki and Hiroyuki Mori. "Mott Transition of Bose–Fermi Mixtures in Optical Lattices Induced by Attractive Interactions". In: *Journal of the Physical Society of Japan* 82.7 (2013), p. 074002. DOI: 10.7566/JPSJ.82.074002. eprint: https://doi.org/10.7566/JPSJ.82.074002. URL: https://doi.org/10.7566/JPSJ.82.074002.

[65] Scott Smale et al. "Observation of a transition between dynamical phases in a quantum degenerate Fermi gas". In: *Science Advances* 5.8 (Aug. 2019). DOI: 10.1126/sciadv.aax1568. URL: https://doi.org/10.1126/sciadv.aax1568.

[66] E. Urban et al. "Observation of Rydberg blockade between two atoms". In: *Nature Physics* 5.2 (2009), pp. 110–114. ISSN: 1745-2481. DOI: 10.1038/nphys1178. URL: https://doi.org/10.1038/nphys1178.

[67] M. Saffman, T. G. Walker, and K. Mølmer. "Quantum information with Rydberg atoms". In: *Rev. Mod. Phys.* 82 (3 2010), pp. 2313–2363. DOI: 10.1103/RevModPhys.82.2313. URL: https://link.aps.org/doi/10.1103/RevModPhys.82.2313.

[68] Hannes Bernien et al. "Probing many-body dynamics on a 51-atom quantum simulator". In: *Nature* 551.7682 (2017), 579—584. ISSN: 0028-0836. DOI: 10.1038/nature24622. URL: https://doi.org/10.1038/nature24622.

[69] A. Omran et al. "Generation and manipulation of Schrödinger cat states in Rydberg atom arrays". In: *Science* 365.6453 (2019), pp. 570–574. DOI: 10.1126/science.aax9743. eprint: https://www.science.org/doi/pdf/10.1126/science.aax9743. URL: https://www.science.org/doi/abs/10.1126/science.aax9743.

[70] W. E. Cooke et al. "Doubly Excited Autoionizing Rydberg States of Sr". In: *Phys. Rev. Lett.* 40 (3 1978), pp. 178–181. DOI: 10.1103/PhysRevLett.40.178. URL: https://link.aps.org/doi/10.1103/PhysRevLett.40.178.

[71] Robert Loew et al. "Apparatus for excitation and detection of Rydberg atoms in quantum gases". In: *arXiv: Quantum Physics* (2007).

[72] Wenhui Li, Paul J. Tanner, and T. F. Gallagher. "Dipole-Dipole Excitation and Ionization in an Ultracold Gas of Rydberg Atoms". In: *Phys. Rev. Lett.* 94 (17 2005), p. 173001. DOI: 10.1103/PhysRevLett.94.173001. URL: https://link.aps.org/doi/10.1103/PhysRevLett.94.173001.

[73] T. Pohl, E. Demler, and M. D. Lukin. "Dynamical Crystallization in the Dipole Blockade of Ultracold Atoms". In: *Phys. Rev. Lett.* 104 (4 2010), p. 043002. DOI: 10.1103/PhysRevLett.104.043002. URL: https://link.aps.org/doi/10.1103/PhysRevLett.104.043002.

[74] Ruben Verresen, Mikhail D. Lukin, and Ashvin Vishwanath. "Prediction of Toric Code Topological Order from Rydberg Blockade". In: *Phys. Rev. X* 11 (3 2021), p. 031005. DOI: 10.1103/PhysRevX.11.031005. URL: https://link.aps.org/doi/10.1103/PhysRevX.11.031005.

[75] Ruben Verresen and Ashvin Vishwanath. "Unifying Kitaev Magnets, Kagomé Dimer Models, and Ruby Rydberg Spin Liquids". In: *Phys. Rev. X* 12 (4 2022), p. 041029. DOI: 10.1103/PhysRevX.12.041029. URL: https://link.aps.org/doi/10.1103/PhysRevX.12.041029.

[76] S. K. Kanungo et al. "Realizing topological edge states with Rydberg-atom synthetic dimensions". In: *Nature Communications* 13.1 (2022), p. 972. ISSN: 2041-1723. DOI: 10.1038/s41467-022-28550-y. URL: https://doi.org/10.1038/s41467-022-28550-y.

[77] Sylvain de Léséleuc et al. "Observation of a symmetry-protected topological phase of interacting bosons with Rydberg atoms". In: *Science* 365.6455 (Aug. 2019), pp. 775–780. DOI: 10.1126/science.aav9105. URL: https://doi.org/10.1126/science.aav9105.

[78] Rhine Samajdar et al. *Emergent $\mathbb{Z}_2$ gauge theories and topological excitations in Rydberg atom arrays*. 2022. DOI: 10.48550/ARXIV.2204.00632. URL: https://arxiv.org/abs/2204.00632.

[79] Kevin Slagle et al. "Quantum spin liquids bootstrapped from Ising criticality in Rydberg arrays". In: *Phys. Rev. B* 106 (11 2022), p. 115122. DOI: 10.1103/PhysRevB.106.115122. URL: https://link.aps.org/doi/10.1103/PhysRevB.106.115122.

[80] Rhine Samajdar et al. "Quantum phases of Rydberg atoms on a kagome lattice". In: *Proceedings of the National Academy of Sciences* 118.4 (2021), e2015785118. DOI: 10.1073/pnas.2015785118. eprint: https://www.pnas.org/doi/pdf/10.1073/pnas.2015785118. URL: https://www.pnas.org/doi/abs/10.1073/pnas.2015785118.

[81] A D Bounds et al. "Coulomb anti-blockade in a Rydberg gas". In: *New Journal of Physics* 21.5 (2019), p. 053026. DOI: 10.1088/1367-2630/ab1c0e. URL: https://dx.doi.org/10.1088/1367-2630/ab1c0e.

[82] Chi Zhang et al. "Submicrosecond entangling gate between trapped ions via Rydberg interaction". In: *Nature* 580.7803 (2020), pp. 345–349. ISSN: 1476-4687. DOI: 10.1038/s41586-020-2152-9. URL: https://doi.org/10.1038/s41586-020-2152-9.

[83] Markus Greiner et al. "Quantum phase transition from a superfluid to a Mott insulator in a gas of ultracold atoms". In: *Nature* 415.6867 (2002), pp. 39–44. ISSN: 1476-4687. DOI: 10.1038/415039a. URL: https://doi.org/10.1038/415039a.

[84] D. Jaksch et al. "Cold Bosonic Atoms in Optical Lattices". In: *Phys. Rev. Lett.* 81 (15 1998), pp. 3108–3111. DOI: 10.1103/PhysRevLett.81.3108. URL: https://link.aps.org/doi/10.1103/PhysRevLett.81.3108.

[85] Belén Paredes and Immanuel Bloch. "Minimum instances of topological matter in an optical plaquette". In: *Phys. Rev. A* 77 (2 2008), p. 023603. DOI: 10.1103/PhysRevA.77.023603. URL: https://link.aps.org/doi/10.1103/PhysRevA.77.023603.

[86] S. Nascimbène et al. "Experimental Realization of Plaquette Resonating Valence-Bond States with Ultracold Atoms in Optical Superlattices". In: *Phys. Rev. Lett.* 108 (20 2012), p. 205301. DOI: 10.1103/PhysRevLett.108.205301. URL: https://link.aps.org/doi/10.1103/PhysRevLett.108.205301.

[87] Gregor Jotzu et al. "Experimental realization of the topological Haldane model with ultracold fermions". In: *Nature* 515.7526 (2014), pp. 237–240. ISSN: 1476-4687. DOI: 10.1038/nature13915. URL: https://doi.org/10.1038/nature13915.

[88] Pimonpan Sompet et al. "Realizing the symmetry-protected Haldane phase in Fermi–Hubbard ladders". In: *Nature* 606.7914 (2022), pp. 484–488. ISSN: 1476-4687. DOI: 10.1038/s41586-022-04688-z. URL: https://doi.org/10.1038/s41586-022-04688-z.

[89] Iñigo Arrazola et al. "Digital-Analog Quantum Simulation of Spin Models in Trapped Ions". In: *Scientific Reports* 6.1 (2016), p. 30534. ISSN: 2045-2322. DOI: 10.1038/srep30534. URL: https://doi.org/10.1038/srep30534.

[90] C. Monroe et al. "Programmable quantum simulations of spin systems with trapped ions". In: *Rev. Mod. Phys.* 93 (2 2021), p. 025001. DOI: 10.1103/RevModPhys.93.025001. URL: https://link.aps.org/doi/10.1103/RevModPhys.93.025001.

[91] G Wendin. "Quantum information processing with superconducting circuits: a review". In: *Reports on Progress in Physics* 80.10 (2017), p. 106001. DOI: 10.1088/1361-6633/aa7e1a. URL: https://dx.doi.org/10.1088/1361-6633/aa7e1a.

[92] Frank Arute et al. "Quantum supremacy using a programmable superconducting processor". In: *Nature* 574.7779 (2019), pp. 505–510. ISSN: 1476-4687. DOI: 10.1038/s41586-019-1666-5. URL: https://doi.org/10.1038/s41586-019-1666-5.

[93] Jay M. Gambetta, Jerry M. Chow, and Matthias Steffen. "Building logical qubits in a superconducting quantum computing system". In: *npj Quantum Information* 3.1 (2017), p. 2. ISSN: 2056-6387. DOI: 10.1038/s41534-016-0004-0. URL: https://doi.org/10.1038/s41534-016-0004-0.

[94] A. Duspayev et al. "Long-range Rydberg-atom–ion molecules of Rb and Cs". In: *Phys. Rev. Res.* 3 (2 2021), p. 023114. DOI: 10.1103/PhysRevResearch.3.023114. URL: https://link.aps.org/doi/10.1103/PhysRevResearch.3.023114.

[95] J. P. Shaffer, S. T. Rittenhouse, and H. R. Sadeghpour. "Ultracold Rydberg molecules". In: *Nature Communications* 9.1 (2018), p. 1965. ISSN: 2041-1723. DOI: 10.1038/s41467-018-04135-6. URL: https://doi.org/10.1038/s41467-018-04135-6.

[96] Simon Hollerith et al. "Quantum gas microscopy of Rydberg macrodimers". In: *Science* 364.6441 (2019), pp. 664–667. DOI: 10.1126/science.aaw4150. eprint: https://www.science.org/doi/pdf/10.1126/science.aaw4150. URL: https://www.science.org/doi/abs/10.1126/science.aaw4150.

[97] Sepehr Ebadi et al. "Quantum phases of matter on a 256-atom programmable quantum simulator". In: *Nature* 595.7866 (2021), pp. 227–232. ISSN: 1476-4687. DOI: 10.1038/s41586-021-03582-4. URL: https://doi.org/10.1038/s41586-021-03582-4.

[98] S. Ebadi et al. "Quantum optimization of maximum independent set using Rydberg atom arrays". In: *Science* 376.6598 (2022), pp. 1209–1215. DOI: 10.1126/science.abo6587. eprint: https://www.science.org/doi/pdf/10.1126/science.abo6587. URL: https://www.science.org/doi/abs/10.1126/science.abo6587.

[99] P. B. Wigley et al. "Fast machine-learning online optimization of ultra-cold-atom experiments". In: *Scientific Reports* 6.1 (2016), p. 25890. ISSN: 2045-2322. DOI: 10.1038/srep25890. URL: https://doi.org/10.1038/srep25890.

[100] A J Barker et al. "Applying machine learning optimization methods to the production of a quantum gas". In: *Machine Learning: Science and Technology* 1.1 (2020), p. 015007. DOI: 10.1088/2632-2153/ab6432. URL: https://dx.doi.org/10.1088/2632-2153/ab6432.

[101] Axel U. J. Lode et al. "Optimized observable readout from single-shot images of ultracold atoms via machine learning". In: *Phys. Rev. A* 104 (4 2021), p. L041301. DOI: 10.1103/PhysRevA.104.L041301. URL: https://link.aps.org/doi/10.1103/PhysRevA.104.L041301.

[102] Giuliano Giudici, Mikhail D. Lukin, and Hannes Pichler. "Dynamical Preparation of Quantum Spin Liquids in Rydberg Atom Arrays". In: *Phys. Rev. Lett.* 129 (9 2022), p. 090401. DOI: 10.1103/PhysRevLett.129.090401. URL: https://link.aps.org/doi/10.1103/PhysRevLett.129.090401.

[103] S. Ji, C. Ates, and I. Lesanovsky. "Two-dimensional Rydberg Gases and the Quantum Hard-Squares Model". In: *Phys. Rev. Lett.* 107 (6 2011), p. 060406. DOI: 10.1103/PhysRevLett.107.060406. URL: https://link.aps.org/doi/10.1103/PhysRevLett.107.060406.

[104] Valentin Crépel. "Dimer states of Rydberg atoms on the Kagome lattice as resources for universal measurement-based quantum computation". In: *AIP Advances* 12.11 (Nov. 2022), p. 115301. DOI: 10.1063/5.0111578. URL: https://doi.org/10.1063/5.0111578.

[105] Neil J. Robinson, Albertus J. J. M. de Klerk, and Jean-Sébastien Caux. "On computing non-equilibrium dynamics following a quench". In: *SciPost Phys.* 11 (2021), p. 104. DOI: 10.21468/SciPostPhys.11.6.104. URL: https://scipost.org/10.21468/SciPostPhys.11.6.104.

[106] A. Smith et al. "Absence of Ergodicity without Quenched Disorder: From Quantum Disentangled Liquids to Many-Body Localization". In: *Phys. Rev. Lett.* 119 (17 2017), p. 176601. DOI: 10.1103/PhysRevLett.119.176601. URL: https://link.aps.org/doi/10.1103/PhysRevLett.119.176601.

[107] Willian M. H. Natori and Johannes Knolle. "Dynamics of a Two-Dimensional Quantum Spin-Orbital Liquid: Spectroscopic Signatures of Fermionic Magnons". In: *Phys. Rev. Lett.* 125 (6 2020), p. 067201. DOI: 10.1103/PhysRevLett.125.067201. URL: https://link.aps.org/doi/10.1103/PhysRevLett.125.067201.

[108] Johannes Knolle, Subhro Bhattacharjee, and Roderich Moessner. "Dynamics of a quantum spin liquid beyond integrability: The Kitaev-Heisenberg-Γ model in an augmented parton mean-field theory". In: *Phys. Rev. B* 97 (13 2018), p. 134432. DOI: 10.1103/PhysRevB.97.134432. URL: https://link.aps.org/doi/10.1103/PhysRevB.97.134432.

[109] J. Knolle et al. "Dynamics of fractionalization in quantum spin liquids". In: *Phys. Rev. B* 92 (11 2015), p. 115127. DOI: 10.1103/PhysRevB.92.115127. URL: https://link.aps.org/doi/10.1103/PhysRevB.92.115127.

[110] R. Penrose. *The Road to Reality: A Complete Guide to the Laws of the Universe*. Knopf Doubleday Publishing Group, 2007. ISBN: 9780679776314. URL: https://books.google.fr/books?id=coahAAAACAAJ.

[111] Shi-Ju Ran et al. *Tensor Network Contractions*. Springer International Publishing, 2020. DOI: 10.1007/978-3-030-34489-4. URL: http://dx.doi.org/10.1007/978-3-030-34489-4.

[112] Román Orús. "A practical introduction to tensor networks: Matrix product states and projected entangled pair states". In: *Annals of Physics* 349 (2014), pp. 117–158. ISSN: 0003-4916. DOI: https://doi.org/10.1016/j.aop.2014.06.013. URL: https://www.sciencedirect.com/science/article/pii/S0003491614001596.

[113] Gemma De las Cuevas et al. "Irreducible forms of matrix product states: Theory and applications". en. In: *Journal of Mathematical Physics* 58.12 (2017), p. 121901. DOI: 10.1063/1.5000784. URL: http://dx.doi.org/10.1063/1.5000784.

[114] J. Ignacio Cirac et al. "Matrix product states and projected entangled pair states: Concepts, symmetries, theorems". In: *Rev. Mod. Phys.* 93 (4 2021), p. 045003. DOI: 10.1103/RevModPhys.93.045003. URL: https://link.aps.org/doi/10.1103/RevModPhys.93.045003.

[115] F. Verstraete et al. "Criticality, the Area Law, and the Computational Power of Projected Entangled Pair States". In: *Phys. Rev. Lett.* 96 (22 2006), p. 220601. DOI: 10.1103/PhysRevLett.96.220601. URL: https://link.aps.org/doi/10.1103/PhysRevLett.96.220601.

[116] Matthieu Mambrini, Román Orús, and Didier Poilblanc. "Systematic construction of spin liquids on the square lattice from tensor networks with SU(2) symmetry". In: *Phys. Rev. B* 94 (20 2016), p. 205124. DOI: 10.1103/PhysRevB.94.205124. URL: https://link.aps.org/doi/10.1103/PhysRevB.94.205124.

[117] Tomotoshi Nishino and Kouichi Okunishi. "Corner Transfer Matrix Renormalization Group Method". In: *Journal of the Physical Society of Japan* 65.4 (1996), pp. 891–894. DOI: 10.1143/JPSJ.65.891. eprint: https://doi.org/10.1143/JPSJ.65.891. URL: https://doi.org/10.1143/JPSJ.65.891.

[118] Román Orús and Guifré Vidal. "Simulation of two-dimensional quantum systems on an infinite lattice revisited: Corner transfer matrix for tensor contraction". In: *Phys. Rev. B* 80 (9 2009), p. 094403. DOI: 10.1103/PhysRevB.80.094403. URL: https://link.aps.org/doi/10.1103/PhysRevB.80.094403.

[119] Masuo Suzuki. "Fractal decomposition of exponential operators with applications to many-body theories and Monte Carlo simulations". In: *Physics Letters A* 146.6 (1990), pp. 319–323. ISSN: 0375-9601. DOI: https://doi.org/10.1016/0375-9601(90)90962-N. URL: https://www.sciencedirect.com/science/article/pii/037596019090962N.

[120] Naomichi Hatano and Masuo Suzuki. *Finding Exponential Product Formulas of Higher Orders*. Ed. by Arnab Das and Bikas K. Chakrabarti. Berlin, Heidelberg: Springer Berlin Heidelberg, 2005, pp. 37–68. ISBN: 978-3-540-31515-5. DOI: 10.1007/11526216_2. URL: https://doi.org/10.1007/11526216_2.

[121] Thomas Barthel and Yikang Zhang. "Optimized Lie–Trotter–Suzuki decompositions for two and three non-commuting terms". In: *Annals of Physics* 418 (2020), p. 168165. ISSN: 0003-4916. DOI: https://doi.org/10.1016/j.aop.2020.168165. URL: https://www.sciencedirect.com/science/article/pii/S0003491620300981.

[122] H. C. Jiang, Z. Y. Weng, and T. Xiang. "Accurate Determination of Tensor Network State of Quantum Lattice Models in Two Dimensions". In: *Phys. Rev. Lett.* 101 (9 2008), p. 090603. DOI: 10.1103/PhysRevLett.101.090603. URL: https://link.aps.org/doi/10.1103/PhysRevLett.101.090603.

[123] Philippe Corboz, Jacob Jordan, and Guifré Vidal. "Simulation of fermionic lattice models in two dimensions with projected entangled-pair states: Next-nearest neighbor Hamiltonians". In: *Phys. Rev. B* 82 (24 2010), p. 245119. DOI: 10.1103/PhysRevB.82.245119. URL: https://link.aps.org/doi/10.1103/PhysRevB.82.245119.

[124] Henning Kalis et al. "Fate of the cluster state on the square lattice in a magnetic field". In: *Phys. Rev. A* 86 (2 2012), p. 022317. DOI: 10.1103/PhysRevA.86.022317. URL: https://link.aps.org/doi/10.1103/PhysRevA.86.022317.

[125] Olivier Gauthé and Frédéric Mila. "Thermal Ising Transition in the Spin-1/2 J_1-J_2 Heisenberg Model". In: *Phys. Rev. Lett.* 128 (22 2022), p. 227202. DOI: 10.1103/PhysRevLett.128.227202. URL: https://link.aps.org/doi/10.1103/PhysRevLett.128.227202.

[126] Léon Autonne. "Sur les matrices hypohermitiennes et sur les matrices unitaires". In: *Ann. Univ. Lyon* 38 (1915), pp. 1–77. URL: https://www.biodiversitylibrary.org/item/192858#page/9/mode/1up.

[127] Alexander M. Chebotarev and Alexander E. Teretenkov. "Singular value decomposition for the Takagi factorization of symmetric matrices". In: *Applied Mathematics and Computation* 234 (2014), pp. 380–384. ISSN: 0096-3003. DOI: https://doi.org/10.1016/j.amc.2014.01.170. URL: https://www.sciencedirect.com/science/article/pii/S0096300314002239.

[128] J. Jordan et al. "Classical Simulation of Infinite-Size Quantum Lattice Systems in Two Spatial Dimensions". In: *Phys. Rev. Lett.* 101 (25 2008), p. 250602. DOI: 10.1103/PhysRevLett.101.250602. URL: https://link.aps.org/doi/10.1103/PhysRevLett.101.250602.

[129] Ho N. Phien et al. "Infinite projected entangled pair states algorithm improved: Fast full update and gauge fixing". In: *Phys. Rev. B* 92 (3 2015), p. 035142. DOI: 10.1103/PhysRevB.92.035142. URL: https://link.aps.org/doi/10.1103/PhysRevB.92.035142.

[130] Didier Poilblanc, Matthieu Mambrini, and Fabien Alet. "Finite-temperature symmetric tensor network for spin-1/2 Heisenberg antiferromagnets on the square lattice". In: *SciPost Phys.* 10 (2021), p. 019. DOI: 10.21468/SciPostPhys.10.1.019. URL: https://scipost.org/10.21468/SciPostPhys.10.1.019.

[131] Didier Poilblanc et al. "Resonating-valence-bond superconductors with fermionic projected entangled pair states". In: *Phys. Rev. B* 89 (24 2014), p. 241106. DOI: 10.1103/PhysRevB.89.241106. URL: https://link.aps.org/doi/10.1103/PhysRevB.89.241106.

[132] Jonathan R Shewchuk. *An Introduction to the Conjugate Gradient Method Without the Agonizing Pain*. Tech. rep. USA, 1994.

[133] Laurens Vanderstraeten et al. “Gradient methods for variational optimization of projected entangled-pair states”. In: *Phys. Rev. B* 94 (15 2016), p. 155123. DOI: 10.1103/PhysRevB.94.155123. URL: https://link.aps.org/doi/10.1103/PhysRevB.94.155123.

[134] Ravi Teja Ponnaganti, Matthieu Mambrini, and Didier Poilblanc. “Real-time dynamics of a critical resonating valence bond spin liquid”. In: *Phys. Rev. B* 106 (19 2022), p. 195132. DOI: 10.1103/PhysRevB.106.195132. URL: https://link.aps.org/doi/10.1103/PhysRevB.106.195132.

[135] G. Baskaran, Z. Zou, and P.W. Anderson. “The resonating valence bond state and high-Tc superconductivity — A mean field theory”. In: *Solid State Communications* 63.11 (1987), pp. 973–976. ISSN: 0038-1098. DOI: https://doi.org/10.1016/0038-1098(87)90642-9. URL: https://www.sciencedirect.com/science/article/pii/0038109887906429.

[136] Ying Tang, Anders W. Sandvik, and Christopher L. Henley. “Properties of resonating-valence-bond spin liquids and critical dimer models”. In: *Phys. Rev. B* 84 (17 2011), p. 174427. DOI: 10.1103/PhysRevB.84.174427. URL: https://link.aps.org/doi/10.1103/PhysRevB.84.174427.

[137] Jean-Marie Stéphan et al. “Entanglement in gapless resonating-valence-bond states”. In: *New Journal of Physics* 15.1 (2013), p. 015004. DOI: 10.1088/1367-2630/15/1/015004. URL: https://dx.doi.org/10.1088/1367-2630/15/1/015004.

[138] Takashi Koretsune and Masao Ogata. “Resonating-Valence-Bond States and Ferromagnetic Correlations in the Doped Triangular Mott Insulator”. In: *Phys. Rev. Lett.* 89 (11 2002), p. 116401. DOI: 10.1103/PhysRevLett.89.116401. URL: https://link.aps.org/doi/10.1103/PhysRevLett.89.116401.

[139] Norbert Schuch et al. “Resonating valence bond states in the PEPS formalism”. In: *Phys. Rev. B* 86 (11 2012), p. 115108. DOI: 10.1103/PhysRevB.86.115108. URL: https://link.aps.org/doi/10.1103/PhysRevB.86.115108.

[140] Henrik Dreyer et al. “Robustness of critical U(1) spin liquids and emergent symmetries in tensor networks”. In: (2020). DOI: 10.48550/ARXIV.2008.04833. URL: https://arxiv.org/abs/2008.04833.

[141] H W J Blote and H J Hilborst. “Roughening transitions and the zero-temperature triangular Ising antiferromagnet”. In: *Journal of Physics A: Mathematical and General* 15.11 (1982), p. L631. DOI: 10.1088/0305-4470/15/11/011. URL: https://dx.doi.org/10.1088/0305-4470/15/11/011.

[142] Fabien Alet et al. “Classical dimers with aligning interactions on the square lattice”. In: *Phys. Rev. E* 74 (4 2006), p. 041124. DOI: 10.1103/PhysRevE.74.041124. URL: https://link.aps.org/doi/10.1103/PhysRevE.74.041124.

[143] R. Moessner and S. L. Sondhi. "Ising and dimer models in two and three dimensions". In: *Phys. Rev. B* 68 (5 2003), p. 054405. DOI: 10.1103/PhysRevB.68.054405. URL: https://link.aps.org/doi/10.1103/PhysRevB.68.054405.

[144] Juraj Hasik and Federico Becca. "Optimization of infinite projected entangled pair states: The role of multiplets and their breaking". In: *Phys. Rev. B* 100 (5 2019), p. 054429. DOI: 10.1103/PhysRevB.100.054429. URL: https://link.aps.org/doi/10.1103/PhysRevB.100.054429.

[145] Carl Eckart and Gale Young. "The approximation of one matrix by another of lower rank". In: *Psychometrika* 1.3 (Sept. 1936), pp. 211–218. DOI: 10.1007/bf02288367. URL: https://doi.org/10.1007/bf02288367.